The Dissertation Committee for Gang Zhang Certifies that this is the approved version of the following dissertation:

Understanding Rainfall Variability over West Africa and Climate Sensitivity in the Tropics: Observational Analysis and Regional Climate Model Simulations

Committee:

Kerry H. Cook, Supervisor

Robert E. Dickinson

Rong Fu

Charles S. Jackson

Edward K. Vizy

Understanding Rainfall Variability over West Africa and Climate Sensitivity in the Tropics: Observational Analysis and Regional Climate Model Simulations

by

Gang Zhang, B.S.

Dissertation

Presented to the Faculty of the Graduate School of

The University of Texas at Austin

in Partial Fulfillment

of the Requirements

for the Degree of

Doctor of Philosophy

The University of Texas at Austin

December 2015

Dedication

Dedicated to my parents

Acknowledgements

I would like to give my sincere thanks to my Ph.D. supervisor, Professor Kerry H. Cook, for her persistent guidance and support without that it was impossible to complete this dissertation. During my time of working on this dissertation, Kerry has provided me a high standard of academic training and showed me a good example of conducting scientific research. Kerry is also a wonderful teacher, I learnt so much from her graduate level courses and the undergrad course I worked in as a Teaching Assistant with her. I would also like to thank Dr. Edward (Ned) K. Vizy for his suggestions in modeling and data analysis for my dissertation. I thank all the Cook-research-group members I worked with, including Dr. Julian Crétat, Dr. Naresh Neupane, and Ms. Caroline Binkley. Our weekly group meeting discussion is an effective way to obtain suggestions from Kerry, Ned and other group members. I also thank Professor Robert E. Dickinson, Professor Rong Fu, and Dr. Charles S. Jackson for serving my Ph.D. dissertation committee.

I also give my grateful thanks to Professor Zong-Liang Yang, who supervised me in the first two years of my graduate study at UT-Austin. Zong-Liang guided me how to do scientific research and how to be an excellent climate modeler. I also thank him for providing me many opportunities to work on different projects and connect with people for collaboration. I want to thank Dr. Hua Su, Dr. Xiaodan Guan, Dr. Mingjie Shi, and Dr. Zhong-Feng Xu for their countless helps and warm encouragement during the early stage of my Ph.D. My Ph.D. time would have been very difficult without their support.

I also give my thanks to Dr. Fei Chen and Dr. Michael Barlage at National Center for Atmospheric Research (NCAR) for supervising my visit in summer 2012. Fei is a

wonderful supervisor to work with. He is very nice and helpful, and really cares about his students' progress and future career development. Michael and I had great interactions on model developing activities. I also thank Mr. Mukul Tewari and Mr. Kevin Manning in our group at NCAR for their helps to my research. In addition, I also thank the other WRF team members in NCAR MMM division I often consulted with, including Dr. Wei Wang, Mr. Dave Gill, Mr. Michael Duda, Ms. Cindy Bruyere, and Dr. Bill Skamarock, etc., for their generous helps on improving my modeling skills and designing my simulations.

I thank all the editors and anonymous reviewers who processed my publications and eventually improved the quality of my dissertation. I also thank editors who invited me for peer reviewing, which was a great academic experience.

The numerical simulations in my dissertation are conducted on supercomputers at Texas Advanced Computing Center (TACC). I thank TACC consulting team for their efforts in helping my scientific computation on TACC supercomputers. I also thank Dr. Muhammad Shaikh in my department for technical helps on computation. I also thank Dr. Feng He at University of Wisconsin at Madison for providing his unprecedented 22,000-year transient CCSM simulation outputs to me for one of my project not included in this dissertation.

Thanks to National Science Foundation (NSF) for the funding during my dissertation. Thanks to all the instructors I took courses with at UT-Austin. Also, thanks to all the administrative staff in Jackson School of Geosciences, especially to our graduate coordinator Mr. Philip Guerrero who is always ready to help the students.

I would like to thank my friends I have not mentioned: Dr. Hongchun Jin, Yang Shi, Tong Ren, Ze Yang, Hao Ye, Shixuan Zhang, Quancheng Zhao, Lijing Zhao, Weiwei Tang, Xitian Cai, Lichun Wang, Wenting Fu, Qinjian Jin, Liyan Jia, Shengbo Wang, Yuyan Cui, Guo Zhang, Chen Zhang, and Margo Grace, for their encouragement and helps to me.

Finally, I would like to thank my parents for their understanding and firm support during my Ph.D. I dedicate this dissertation to them.

Finishing a Ph.D. degree is a unique experience in life. At the end, I use a famous poem in *Dream of the Red Chamber* as a summary of this dissertation and my Ph.D. journey:

"Pages full of silly litter,
Tears a handful sour and bitter;
All a fool the author hold,
But their zest who can unfold!"

Understanding Rainfall Variability over West Africa and Climate Sensitivity in the Tropics: Observational Analysis and Regional Climate Model Simulations

Gang Zhang, Ph.D.

The University of Texas at Austin, 2015

Supervisor: Kerry H. Cook

Abstract

West African rainfall plays an important role in tropical climate and hydrological cycle. This study aims to advance our understanding of the West African rainfall across different timescales, from the diurnal cycle to interannual variations. Then, the study is extended to understand the climate sensitivity in the tropics with an increase of greenhouse gases.

First, on a short timescale, the diurnal cycle of warm season rainfall over West Africa is investigated. In both the climatology and the 2006 case study, most of West Africa shows a single diurnal peak of rainfall in either the afternoon or at night. Afternoon rainfall peaks are associated with an unstable lower troposphere. Nocturnal rainfall peaks are associated with rainfall systems propagating westward. They occur most frequently about 3°-10° of longitude downstream of regions with afternoon rainfall peaks. Rainfall systems in the convection-permitting simulation show similar westward

propagation with afternoon peaks associated with elevated topography and nocturnal peaks downstream of the topographic afternoon rainfall regions. However, the model fails to reproduce the observed afternoon rainfall peaks in several regions far away from the downstream of elevated topography.

Second, on a longer timescale, the climatology and interannual variations of the West African monsoon demise are investigated using the Tropical Rainfall Measuring Mission and the Global Precipitation Climatology Project precipitation datasets along with the ERA-Interim reanalysis. During monsoon demise, the rainfall maximum progresses southward smoothly from the Sahel to the Gulf of Guinea. The climatological monsoon demise date is October 20th. The demise date varies between October 5th and 30th. An early (late) demise is associated with an anomalously strong (weak) North Atlantic subtropical high. The monsoon season total rainfall is found to be significantly correlated with the demise date.

Finally, idealized regional model simulations are used to understand the climate sensitivity over the broad tropical region. The model is configured with idealized continents and oceans. With a doubling of CO_2, the land and the ocean warm at different rates. The changes of the continental heat lows, subtropical highs and land-based rainfall in the tropics are explored and linked to the surface warming.

Table of Contents

List of Tables

List of Figures

Chapter 1: General Introduction

The essential research objective of this dissertation is to understand the rainfall variations and climate sensitivity in the tropical regions using observational data and the state-of-the-are climate model simulations. The dissertation is organized into five chapters. Chapter 1 provides a general introduction to the following chapters. Chapters 2, 3, 4, and 5 each describes a research subject within the scope of this dissertation, respectively. The diurnal cycle of rainfall over West Africa is investigated in Chapters 2 and 3, using observational datasets and high-resolution regional climate model simulation, respectively. Moreover, the West African monsoon demise is explored in Chapter 4. Material from this chapter is already published on the Journal of Geophysical Research-Atmospheres (Zhang and Cook 2014). Finally, an idealized simulation is presented in Chapter 5 to understand the climate sensitivity in the tropics given an increase of greenhouse gases. General conclusions are summarized in Chapter 6.

The West African monsoon plays an important role in the regional climate and water resources of the Sahel. The monsoon has a significant influence on agricultural management as it brings most of the rainfall to West Africa during the course of a year. For example, the growing season is largely determined by the timing the West African monsoon rainfall. Warm season rainfall over West Africa, and more broadly over all the tropics, varies greatly on wide-ranging timescales, and remains a challenging issue for weather and climate prediction. Therefore, an improved understanding of the physical processes that control the West African monsoon season is important because it will ultimately improve weather and climate forecasts for this region.

In Chapters 2 and 3, we focus on the diurnal cycle of West African rainfall. A physical understanding of how the diurnal cycle is controlled is crucial for simulating and predicting changes in both mean precipitation and extreme rainfall events. For example, to confidently project how rainfall will change in the future under global warming, climate models are expected to realistically capture the diurnal cycle of rainfall in the contemporary climate. However,

previous studies (Cook and Vizy 2006; Dai 2006; Xue et al. 2010) show that the diurnal cycle of tropical rainfall is poorly simulated by the current generation of general circulation models (GCMs). Even when models produce realistic average rainfall amounts on seasonal timescales, they fail to correctly simulate the diurnal cycle of rainfall (e.g., Dai 2006). This deficiency indicates that GCMs do not correctly represent all of the physical processes that control the diurnal cycle of tropical rainfall. The purpose of this chapter is to better understand the diurnal cycle of warm season rainfall over West Africa, including its underlying physical processes. Observed precipitation is used to characterize the diurnal cycle, and atmospheric reanalyses are used to explore the physical processes that control it. We also evaluate the ability of a regional, convection-permitting atmospheric model to reproduce the diurnal cycle of rainfall over West Africa and capture the underlying physical processes.

In Chapter 4, the demise phase in seasonal cycle of the West African monsoon is studied. Both the onset and the demise are important in determining the seasonal cycle of the West African monsoon. The onset of the Sahel monsoon season occurs typically in late June or early July with an abrupt shift of the rainfall maximum from the Guinean coast (~5°N) to the Sahel (~10°N); this is called the West African monsoon jump (Sultan and Janicot 2003; Hagos and Cook 2007). From late September to October, rainfall over the Sahel decreases gradually. Both the onset and demise dates are critical for agricultural planning. For example, a late onset may lead to late planting, and an early end of the rainy season might cause crop failure. While West African monsoon onset processes have been explored in several studies (Sultan and Janicot 2003; Ramel et al. 2006; Hagos and Cook 2007), less attention has been paid to the demise process. The purpose of this chapter is to better understand the basic dynamics of the West African monsoon demise, and its relationship to seasonal rainfall totals, from the perspectives of the climatology and interannual variations**.** The findings of this chapter improve our understanding of the physical processes associated with the West African monsoon demise, and serve as a basis for modeling investigations. In addition, the physical processes that regulate the

monsoon demise provide support for operational weather and climate forecasts of the monsoon demise.

In Chapter 5, a series of regional climate model simulations are conducted with idealized continents and oceans to advance the understanding of climate sensitivity in the tropics under the forcing of increasing greenhouse gases. Dynamics of the tropical climate is an essential component in global climate system and hydrological cycle. Under the global warming scenarios with increasing greenhouse gases, it is important to understand how the tropics responses to this forcing. Some of the tropical regions, e.g. the semi-arid West African Sahel region, are sensitive to climate changes. A better understanding of climate sensitivity in the tropics will help people in these regions prepare for mitigation and adaptation.

One important driver of the tropical climate sensitivity is the land-sea distribution. Land has a smaller heat capacity; therefore it always warms or cools faster than the oceans. This thermal contrast is an important driver of tropical climate sensitivity given the same greenhouse gases forcing. However, in the real world, the signal of the land-sea contrast is complicated due to the shape and location of the continents on the Earth. To better understand the climate sensitivity in the tropics related to the land-sea distribution, in this chapter we use a coupled regional climate with idealized continents and oceans. This idealized approach will reduce other factors involved in the tropical climate and highlight the role of land-sea distribution, which has been widely used in studying climate dynamics. The idealized model can be built up with more complexity until reached to the full complexity of an operational climate system model. This hierarchical structure in modeling the climate system has the advantage that any finding in the idealized models can be easily transferred and applied to understand the full-complexity model.

In Chapter 6, the general conclusions are stated and an outlook is provided for the future work of this dissertation.

Chapter 2: The Diurnal Cycle of Warm Season Rainfall over West Africa: Observations

ABSTRACT

This study provides an improved understanding of the diurnal cycle of warm season (June-September) rainfall over West Africa, including its underlying physical processes. Rainfall from the Tropical Rainfall Measuring Mission and atmospheric dynamics fields from reanalyses are used to evaluate the 1998-2013 climatology and a case study for 2006.

In both the climatology and the 2006 case study, most regions of West Africa are shown to have a single diurnal peak of rainfall in either the afternoon or at night. Averaging over West Africa produces a diurnal cycle with two peaks, but this type of diurnal cycle is quite atypical on smaller space scales. Rainfall systems are usually generated in the afternoon and propagate westward, lasting into the night. Afternoon rainfall peaks are associated with an unstable lower troposphere. They occur either over topography or in regions undisturbed by nocturnal systems, allowing locally-generated instability to dominate. Nocturnal rainfall peaks are associated with the westward propagation of rainfall systems, and not generally with local instability. Nocturnal rainfall peaks occur most frequently about 3°-10° of longitude downstream of regions with afternoon rainfall peaks. The diurnal cycle of rainfall is closely associated with the timing of extreme rainfall events.

2.1. INTRODUCTION

Warm season rainfall in the tropics varies greatly on wide-ranging timescales, and remains a challenging issue for weather and climate prediction. Here we focus on the diurnal cycle of West African rainfall. A physical understanding of how the diurnal cycle is controlled is

crucial for simulating and predicting changes in both mean precipitation and extreme rainfall events. For example, to confidently project how rainfall will change in the future under global warming, climate models are expected to realistically capture the diurnal cycle of rainfall in the contemporary climate. However, previous studies (e.g., Cook and Vizy 2006; Dai 2006; Xue et al. 2010) show that the diurnal cycle of tropical rainfall is poorly simulated by the current generation of general circulation models (GCMs). Even when models produce realistic average rainfall amounts on seasonal timescales, they fail to correctly simulate the diurnal cycle of rainfall(e.g., Dai 2006b). This deficiency indicates that GCMs do not correctly represent all of the physical processes that control the diurnal cycle of tropical rainfall.

The purpose of this study is to better understand the diurnal cycle of warm season rainfall over West Africa, including its underlying physical processes. We aim to provide a more general characterization of the diurnal cycle of rainfall at localized spatial scales and to better understand the geographical distribution of the diurnal cycle of rainfall over a broad West African domain. Observed precipitation is used to characterize the diurnal cycle, and atmospheric reanalyses are used to explore the physical processes that control it.

The current understanding of the diurnal cycle of rainfall over West Africa is reviewed in section 2. Observational and reanalysis data sets used in this study are described in section 3. Results are presented in section 4, and conclusions are summarized in section 5. To further advance our understanding of the diurnal cycle of rainfall, convection-permitting simulations over West Africa are analyzed in Part II (Zhang et al. 2015a).

2.2. BACKGROUND

The diurnal cycle of rainfall over West Africa is discussed in several studies that have a global perspective. Dai (2001) examines 3-hourly reports from weather stations around the globe to find that the Sahel region (defined as 10°W-20°E and 10-15°N) exhibits a nocturnal peak for non-drizzle rainfall, and both afternoon and nocturnal peaks for showery rainfall. Dai (2001) also

shows that the afternoon rainfall peak is related to local instability as indicated by the presence of large values of convective available potential energy (CAPE). Using satellite brightness temperature as a proxy for rainfall, Yang and Slingo (2001) show that afternoon and evening rainfall peaks are dominant over West Africa, and also explore connections with atmospheric instability and the life cycle of mesoscale convective systems (MCSs).

NASA Tropical Rainfall Measurement Mission (TRMM, Huffman et al. 2007) satellite observations have enabled a number of studies of the diurnal cycle over West Africa. Nesbitt and Zipser (2003) examine TRMM radar and microwave imager data for 1998-2001 and suggest that, over tropical land, rainfall associated with MCSs has a late evening peak while the intensity of MCSs is greatest in the late afternoon. The peak in non-MCS rainfall is in the afternoon.

In a detailed analysis of sub-Saharan African rainfall using the TRMM microwave imager data for 1998-2001, Mohr (2004) finds that the diurnal cycle of rainfall has a single late afternoon/evening peak south of 10^{o}N and two peaks – one in the evening and the other near midnight – north of 10^{o}N. This study also suggests that the frequency and life cycle of MCSs are important influences on the diurnal cycle. Another study using Niger station rainfall observations suggests that the peak hour of rainfall has regional variations. (Shinoda et al. 1999).

The diurnal cycle of rainfall over West African is known to be influenced by the life cycle of convective systems. West African warm season rainfall is linked with convective systems that range from localized, short-lived (1-3 hours) systems to long-lasting (6-24+ hours) MCSs (Laing and Fritsch 1993; Le Barbé and Lebel 1997; Hodges and Thorncroft 1997; Mohr 2004). Mathon et al. (2002) suggest that more than 90% of the warm season rainfall over the Sahel is contributed by organized convective systems (OCSs), which are a class of MCSs. Their analysis over Nigeria implies that the diurnal cycle of rainfall is associated with the propagation of OCSs that originate over upstream topography. By tracking the life cycle of West African MCSs in infrared satellite images, Mathon and Laurent (2001) show that, over the central Sahel, the frequency of summer MCSs peaks at 19:00 local solar time (LST). The MCSs are classified into a four-phase life cycle: initiation, splits, dissipations, and mergers. The frequency of

occurrence of MCSs in the initiation phase peaks at 16:00 LST, while other phases peak in the late afternoon or early evening. In an analysis of station rainfall data in a wet year and a dry year, Shinoda et al. (1999) conclude that the diurnal cycle of rainfall over Niger is related to the westward propagation of MCSs initiated around the Aïr mountains in the afternoon. Laing et al. (2008) also find that the diurnal cycle of West African rainfall is influenced by the zonal propagation of convective systems that are initiated over elevated terrain and propagate westward. Using the TRMM precipitation product, Janiga and Thorncroft (2014) conclude that Sahelian rainfall in the afternoon (early morning) is mainly generated by small (large) size convective systems.

In summary, previous studies have examined the diurnal cycle of rainfall over specific West African regions, or as an average over large portions of West Africa. The time periods analyzed have been limited to case studies of a single season or climatologies formed by averaging a relatively small number of years. In this paper we build on this previous work to further advance our understanding of how and why the diurnal cycle varies spatially across West Africa, examining the geographical distribution of the diurnal cycle of rainfall over a broad West African domain and then focusing on localized diurnal cycles to understand the observed distribution. In the associated Part II paper (Zhang et al. 2015a), we compare the observed geographical distribution of the diurnal cycle in simulations with a convection-permitting regional model to further advance our understanding of the physical processes that drive the diurnal cycle of precipitation over West Africa and our ability to capture these processes correctly in models.

2.3. METHODOLOGY

To examine the diurnal cycle of rainfall, we use the NASA 3-hourly Tropical Rainfall Measuring Mission precipitation 3B42V7 product (Huffman et al. 2007). TRMM coverage includes all longitudes from 50°S to 50°N with a spatial resolution of 0.25°. Compared with

previous generations of remote sensing products for rainfall, e.g., rainfall estimates based on brightness temperature, the TRMM rainfall product has a much finer spatial resolution with robust statistics, which allows advancements of the characterization of the diurnal cycle of rainfall to finer scales.

We analyze the diurnal climatology for June, July, August and September (JJAS) from 1998 through 2013. In addition, the warm season of 2006 is used as a case study since multi-year averaging can obscure the physics of synoptic-scale events. 2006 is selected for our case study because this year coincides with the African Monsoon Multidisciplinary Analysis (AMMA) special observing period (Lebel et al. 2010), with more extensive observations available.

The 3-hourly Modern-Era Retrospective Analysis for Research and Applications (MERRA, Rienecker et al. 2011) reanalysis is used for atmospheric dynamics fields. At the time of this study, MERRA was the only reanalysis product that supplied atmospheric dynamics fields on 3-hourly intervals over West Africa. To reduce the uncertainty of using reanalysis data, other global reanalyses are also compared with MERRA, including the National Centers for Environmental Prediction (NCEP) Climate Forecast System Reanalysis (CFSR, Saha et al. 2010), the ECMWF ERA-Interim reanalysis (Dee et al. 2011), and the ECMWF reanalysis from their operational forecasts for the AMMA observational campaign with AMMA radiosonde data assimilated (ECMWF-OPERA, Agustí-Panareda et al. 2010). Note that CFSR, ERA-Interim, and ECMWF-OPERA are available at 6-hourly intervals for 00 UTC, 06 UTC, 12 UTC and 18 UTC.

The mean diurnal cycle of rainfall rate, $\overline{R}$, is defined as the mean rainfall rate at each 3-hourly interval:

$$\overline{R}(h) = \frac{\sum_{d=1}^{N} P(d,h)}{N} \qquad (2.1)$$

where d and h are indices indicating the day and the 3-hourly interval, respectively. $P(d,h)$ is the precipitation rate at (d, h). N is the number of days in the sample.

The analyses region is 7°W-21°E and 7°N-17°N (Figure 1), which is the same as the model domain for the convection-permitting simulations in Part II (Zhang et al. 2015a). This is a large area, covering 3.38×10^6 km^2, or nearly half the surface area of the contiguous United States. The Bodélé Depression (centered around 18°E, 17°N) is included in this domain. This region is one of the largest sources of aerosol dust on the planet (Washington et al. 2009), but nearly all of the emissions occur during the winter months while the analysis here is confined to the warm season.

2.4. RESULTS

2.4.1 Geographical distribution of the diurnal cycle of rainfall over West Africa

Figures 1a-h show the percentage of total daily rainfall delivered during each 3-hourly interval in the TRMM climatology (1998-2013). Note that the TRMM rainfall product is at 3-hourly intervals. Since the zonal range of our analysis region is 7°W-21°E, which is within the 3-hour time zone centered on Greenwich meridian, UTC is used as the local time of the analysis region. The highest percentages, 25% to 50%, generally occur in the late afternoon (i.e., 18 UTC) or at night (i.e., 21 UTC, 00 UTC, and 03 UTC). Rainfall percentages are minimal from 09 UTC until noon (12 UTC), with values below 15% in most locations. Both maxima and minima exhibit pronounced spatial variations.

Figure 2 displays the distribution of the peak hour of rainfall in the climatological diurnal cycle. Major features include late afternoon peaks over southwestern Mali, Burkina Faso, Ghana, Togo and Benin; nocturnal peaks (00 UTC and 03 UTC) around the political boundaries between Burkina Faso, Niger, Benin, and Nigeria; late evening (21 UTC) peaks in western Niger, and afternoon (15 UTC and 18 UTC) peaks in the vicinity of Lake Chad. The spatial differences of rainfall peak hour are consistent with Shinoda et al. (1999). These spatial variations in the timing of the rainfall peak suggest that dominant physical process likely vary regionally.

This regionalization is apparent in Figure 3, which shows the climatological diurnal cycle of rainfall area-averaged over 1°×1° grid boxes from 7°W to 21°E and 5°N to 15°N. 98% of the grid boxes analyzed contain a single diurnal peak. The single peak is either in the afternoon or night. The remaining 2% of the boxes exhibit double peaks, one in the afternoon and another at night.

This result indicates that, climatologically speaking, most of West Africa exhibits a single diurnal peak of rainfall. This is different from some previous studies. For example, Mohr (2004) concludes that the rainfall north of 10°N over the Sahel has two diurnal peaks, based on a large-scale area average (10-15°N, 18°W-32°E). As shown in Figure 2, the rainfall in this region has a single diurnal peak but with substantially spatial variations of the peak time; two peaks in the climatological diurnal cycle only occur in the large-scale area average.

Different features in the geographical distribution of the diurnal cycle of rainfall can also arise due to time averaging. For this reason, a case study of the 2006 warm season is analyzed. This case study also allows us to more directly relate synoptic events to the diurnal cycle. Figure 4 shows peak hours of the diurnal cycle of rainfall for JJAS of 2006. A similar geographical distribution of the peak hours is found in the 3-hourly PERSIANN rainfall data (Sorooshian et al. 2000, results not shown). The large-scale features are similar to the climatology in Figure 2, which suggests that the warm season (JJAS) in 2006 is reasonably representative of the climatology. The greater spatial variability is expected due to the shorter averaging period.

Figure 5 shows the JJAS 2006 mean diurnal cycle of rainfall in each 1°×1° grid box within the region from 7°W to 21°E and 5°N to 15°N. Distinct from the climatology, 72% of the small regions show a single peak, while 26% exhibit double peaks. This indicates that the very high percentage (98%) of single peaks seen in the climatology is, in part, a vestige of the multi-year time averaging. However, it is still the case that most regions experience a single diurnal rainfall maximum.

Three regions, indicated in Figure 4, are defined for more in-depth analysis of the diurnal cycle. These regions cover areas with fairly uniform diurnal cycles of rainfall that are similar in

the climatology (Figs. 2 and 3) and in 2006 (Fig. 4). One region has a late afternoon peak at 18 UTC and is denoted AF (3°W-0°W, 9°N-11.5°N). Two domains have nocturnal rainfall peaks. The southern region with a nocturnal peak at 00 UTC is referred to as SN (2°E-5°E, 9°N-11.5°N), and the northern region with a nocturnal peak at 03 UTC is named NN (2°E-5°E, 13.5°N-16.5°N).

Figure 6 shows a Hovmöller diagram of the TRMM 3-hourly rainfall for JJAS 2006 averaged between 9°N-11.5°N, which includes the AF and SN domains. Generally, rainfall systems form in the afternoon and propagate westward during the late afternoon and night. This westward propagation includes heavy rainfall episodes, e.g., the one starting on the afternoon of July 27, 2006, at 9°E; another begins in the afternoon of September 1, 2006, at 25°E and propagates to the west over the next several days. Many of these rainfall events are associated with MCSs, and this westward propagation agrees with the studies of life cycle of MCSs (e.g., Mathon and Laurent 2001; Mathon et al. 2002).

Rainfall systems that propagate into the SN domain (2°E -5°E) to create the nocturnal maximum are primarily the result of afternoon rainfall immediately to the east (about 5°E - 15°E). A few long-lasting rainfall episodes can be tracked back to about 20°E. One event begins in the afternoon of July 20, 2006, at 25°E and lasts until the early morning of July 22, 2006, at 2°E. Another event forms in the afternoon of September 1, 2006, at 27°E and remains strong through September 5, 2006, as it propagates westward across West Africa. Note that, although there is regular initiation of afternoon rainfall in the vicinity of the Ethiopian Highlands (40°E), most of these rainfall systems do not remain intact past 10°E. A Hovmöller diagram averaged between 13.5°N-16.5°N (the latitudes of the NN domain, not shown) displays similar westward propagating features, but with less frequent events and lower rainfall rates compared with Figure 6 because the overall rainfall is less intense at this latitude range.

2.4.2 Afternoon rainfall: The role of local instability

The relationship of local atmospheric instability to the afternoon rainfall peaks is explored by examining the vertical profile of the moist static energy (MSE). MSE is the sum of the sensible, latent, and geopotential heat contents of a parcel:

$$MSE = c_p T + Lq + gz \qquad (2.2)$$

where c_p is the specific heat of air at constant pressure, T is the air temperature, L is the latent heat of water vaporization, q is the specific humidity, g is the gravity acceleration, and z is the geopotential height. MSE increasing with altitude indicates a stable atmosphere. Analysis of the MSE allows one to distinguish between the roles of temperature and moisture variations in changing atmospheric stability properties.

Figure 7a displays profiles of MSE anomalies (solid lines) for 00 UTC (green), 03 UTC (blue), and 18 UTC (red) averaged over the AF domain. The anomaly is defined as the difference between the averaged MSE profiles at every 00 UTC, 03 UTC, 18 UTC, respectively, and the mean of JJAS 2006. The moisture (Lq) and temperature ($c_p T$) components of the MSE anomalies (see Eq. 5) are indicated by the dot-dashed and dashed lines, respectively.

The diurnal cycle of the MSE anomaly in the AF region is confined below 850 hPa. The afternoon rainfall peak is associated with an anomalous MSE profile (red solid line) that is unstable below 850 hPa and neutral above that level; it is near neutral at 00 UTC and stable at 03 UTC from the surface to 700 hPa. The MSE anomalies are primarily associated with changes in both Lq and $c_p T$, as the contribution by gz is negligible in the lower troposphere (not shown). The contribution from $c_p T$ reflects daytime warming of the land surface. Despite these diurnal variations of surface temperature, diurnal variations in Lq are small at the lowest level (975 hPa) and greatest between 900 hPa and 925 hPa, with positive anomalies at 18 UTC and negative anomalies at 00 UTC and 03 UTC.

The MSE anomaly profiles for the SN (Fig. 7b) and NN (Fig. 7c) regions have similar diurnal variations to the AF region but, in the NN region (Fig. 7c), the Lq anomaly is negative near the surface at 18 UTC. However, the total MSE profile remains unstable due to the sensible

heating term. Although rainfall in these regions peaks at night, the MSE anomaly profiles are not favorable for the initiation of nocturnal convection. Note that the SN and NN domains still have afternoon rainfall, though not as peaks.

Figures 8a-c display the AF domain's MSE anomaly profiles using CFSR, ERA-Interim and ECMWF-OPERA reanalyses. Only 18 UTC and 00 UTC are shown because 03 UTC is not available in these 6-hourly data sets. The vertical distribution of the 18 UTC profiles of the MSE, temperature and moisture terms are similar to those in Figure 7a, although the magnitudes vary. This suggests that the physical processes evaluated here are not sensitive to the choice of reanalysis.

Over the AF region the difference in the sensible heating term between day and night can be explained by the fact that land surface heats (cools) the low-level atmosphere in the afternoon (nighttime). To understand the diurnal cycle of the latent heating term, Figure 9a displays the diurnal cycle of low-level specific humidity averaged over the AF domain. The afternoon peaks of moisture at 900 hPa and 925 hPa are associated with smaller vertical gradients, suggesting strong vertical mixing.

Figure 9b shows the diurnal cycle of the planetary boundary layer (PBL) height over AF. The nocturnal PBL is below 975 hPa, while the afternoon PBL is well-developed up to 900 hPa. Therefore, the nocturnal atmospheric moisture from 975 hPa to 875 hPa is more stratified while, in the afternoon, the atmospheric moisture at 900 hPa and 925 hPa is well mixed (Figure 9a).

In general, the afternoon rainfall peaks over West Africa are associated with unstable atmospheric profiles in the lower troposphere. Based on Figures 2 and 4 we conclude that the afternoon rainfall peaks are dominant over topographical features and in several regions far removed from elevated topography where local instability dominates.

2.4.3 Nocturnal rainfall: The role of propagating convective systems

Nocturnal rainfall over the broader West African region is associated with westward propagating MCSs as indicated by the Hovmöller diagrams in Figure 6 and previous studies (e.g., Shinoda et al. 1999; Laing et al. 2008). In this subsection, we examine preferred regions for the initiation of these propagating systems and their pathways across West Africa.

If the nocturnal rainfall in a given region is supported by propagation from a preferred location upstream, then rainfall in that region at the peak hour will be positively correlated with the rainfall in the upstream location with some time lag. Figure 10a shows the correlation coefficient map between the JJAS 2006 time series of 03 UTC rainfall averaged over the NN region and the time series of 15 UTC rainfall at each grid point. The nocturnal rainfall peaks are related to previous afternoon rainfall in the relative depression between the Aïr Mountains of Niger and the Jos Plateau of Nigeria. The windward slopes of these topographical features favor the initiation of afternoon convection. This region has an afternoon rainfall peak as indicated in Figures 2 and 5. This correlation is a necessary but not sufficient condition for tracking the movements of rainfall events. An examination of the time series is also conducted to confirm the propagation track. Visual inspection of 3-hourly TRMM rainfall snapshots (not shown) indicates that the region with high correlation centered near 7°E and 8°N in Figure 10b is not directly related to the propagation of rainfall into the NN region.

Figures 10b - d display similar correlation maps relating nocturnal rainfall in the NN region with rainfall in other regions at 18 UTC and 21 UTC on the previous day, and on the same day at 00 UTC. Taken together, Figures 10a - d reveal a typical pathway that propagating systems follow to produce the 03 UTC NN rainfall peak. These rainfall systems generally form near 10°E and move westward along the boundary between Niger and Nigeria.

Figures 10e - g show correlation coefficient maps that relate the 00 UTC rainfall time series averaged over SN with each grid point at the previous 15 UTC, 18 UTC, and 21 UTC times, respectively. The nocturnal peak over SN is associated with rainfall that is initiated near the Jos Plateau (centered at 8°E and 9°N) on the previous afternoon at 15 UTC. Similar to the

NN region, a westward propagating pathway occurs. Additionally, for the SN and NN regions, the midnight/early-morning rainfall shows no significant correlation with the rainfall on the following afternoon.

To summarize, nocturnal rainfall over the NN and SN regions is both found to be associated with the development of afternoon convection approximately 500 km upstream (i.e., to the east). The average propagating speed of the rainfall systems is 15 m s^{-1}, which is close to the estimation in Shinoda et al. (1999).

Next we examine the low-level flow related to this propagation. Figure 11 shows the wind from 950 hPa to 600 hPa in JJAS 2006. Below 850 hPa, the southwesterly monsoon flow dominates, while above 850 hPa the wind is mainly easterly, which is favorable for the westward propagation of MCSs. The seasonally-averaged zonal wind speed does not exhibit a diurnal cycle, and the 650 hPa zonal wind speed averaged between 15 UTC and 03 UTC on the next day is 9.5 m s^{-1}. Our analysis suggests that in order to produce a nocturnal rainfall peak there needs to be large-scale mid-tropospheric easterly flow and an afternoon rainfall system that is generated at the appropriate distance upstream. This applies to the NN and SN regions as well as other regions with nocturnal rainfall peaks (Figures 2 and 4). For example, the nocturnal peaks in the southeastern part of the domain (7°E-20°E and 8°N-9°N) are associated with afternoon rainfall initiated over the Darfur Mountains of Sudan about 650 km to the east (not shown on this map). The nocturnal peaks at 7°W-4°W and 7°N-10°N are associated with afternoon rainfall peaks over the AF region.

Generally, nocturnal rainfall peaks over West Africa are associated with rainfall systems propagating westward into a neutrally stable environment. Regions with strong nocturnal rainfall are located 3°-10° of longitude downstream (i.e., to the west) of regions with afternoon rainfall peaks. In contrast, regions with afternoon rainfall peaks are either co-located with topographical features, or they are located far from topography allowing locally-generated atmospheric instability to dominate the diurnal cycle.

As discussed in Section 4.1, the diurnal cycle of rainfall is closely associated with the timing of extreme rainfall events. Applying a 50 mm day^{-1} threshold to the rainfall at 03 UTC averaged over the NN domain and at 00 UTC over the SN domain, 12 extreme events (see Table 1) from the summer of 2006 are selected. Four of the 12 events are associated with African easterly waves (AEWs) as indicated by 700 hPa wind and relative vorticity fields (not shown).

Figures 12a - l show the propagation of rainfall from 15 UTC to 03 UTC on the following day for each extreme event. Each of these events shows propagating features that relate nocturnal rainfall to rainfall generated on the previous afternoon to the east. Within the NN region, 4 events in 2006 (Figures 12a, d, e, and f) are associated with systems that formed on the windward slope that lies along the boundary between Niger and Nigeria, and one event (on August 06) originated over the Aïr Mountains of Niger. The August 11 event is a large-scale squall line that formed near 12 UTC on the previous day. It is associated with nocturnal peaks over both the NN and SN regions. In the SN region, all 7 events (Figures 12c, g - l) derive from rainfall events that were initiated over the Jos Plateau and propagated westward. The overlapping of the 00 UTC and 03 UTC rainfall distributions suggests that the system became stationary near midnight.

2.5. CONCLUSIONS

We investigate the geographical distribution of the diurnal cycle of West African warm season (JJAS) rainfall and explore its underlying physical processes using the satellite-derived TRMM precipitation and atmospheric dynamics fields from the MERRA reanalysis.

The diurnal cycle of rainfall is analyzed in the TRMM climatology for 1998-2013. We also evaluate the 2006 warm season (JJAS) as a case study to facilitate a more detailed investigation on synoptic timescales. The high-resolution TRMM rainfall product improves the understanding of the diurnal cycle of rainfall at finer spatial scales.

The conclusions from this observational analysis are summarized as follows:

- Most regions of West Africa (98% in the climatology and 78% in 2006) have a single diurnal peak of rainfall in either the afternoon (i.e., 15 and 18 UTC) or at night (i.e., 21, 00, and 03 UTC). This finding is in contrast to several previous studies (see section 2.) that suggest that the diurnal cycle of rainfall over West Africa is characterized by two peaks. This is a vestige of averaging over a large area, and the result does not apply locally or regionally.
- Two types of regions experience afternoon rainfall peaks. One is regions with topographic features, and the other is regions far removed from upstream topography, i.e., not within the range that is directly influenced by westward propagating rainfall systems originated over the mountains. In these regions, local instability processes dominate. A moist static energy analysis is used to show that the afternoon rainfall peaks are associated with unstable atmospheric profiles dominated by diurnal temperature variations in the lower troposphere; boundary layer moisture variations play a minor role.
- Coherent regions with nocturnal rainfall peaks are located 3°-10° of longitude downstream (i.e., to the west) of regions with afternoon rainfall maxima. These rainfall peaks are associated with the westward propagation of rainfall systems, but not with local instability.
- The diurnal cycle of rainfall is closely associated with the timing of extreme rainfall events. Applying a 50 mm day-1 threshold, 12 extreme events that occurred at night during the summer of 2006 are examined, and each is found to be associated with an MCS that originated on the previous afternoon to the east and propagated to the west.

An improved understanding of the diurnal cycle of rainfall is important for advancing weather and climate prediction over West Africa. To capture the diurnal cycle of rainfall correctly, climate models need to have an accurate representation of the determining physical processes. In Part II (Zhang et al. 2015a), the diurnal cycle of rainfall produced by convection-

permitting simulations is analyzed to evaluate the extent to which the model correctly represents the important physical processes controlling the diurnal cycle of rainfall over West Africa.

Table 2.1. Extreme rainfall events (using 50 mm day^{-1} threshold) at nocturnal peak time for the NN and SN domains during JJAS 2006. The label is the same as listed in Figure 11.

Label	Time	Domain	Rainfall Rate (mm day^{-1})	Associated with AEWs?
(a)	03 UTC July 26, 2006	NN	57.72	Yes
(b)	03 UTC August 06, 2006	NN	72.53	No
(c)	03 UTC August 11, 2006	NN	162.63	Yes
(c)	00 UTC August 11, 2006	SN	59.98	Yes (the same one as in NN)
(d)	03 UTC August 22, 2006	NN	101.20	No
(e)	03 UTC August 28, 2006	NN	58.82	No
(f)	03 UTC September 24, 2006	NN	75.79	No
(g)	00 UTC June 14, 2006	SN	62.81	No
(h)	00 UTC July 15, 2006	SN	113.94	No
(i)	00 UTC July 28, 2006	SN	53.94	Yes
(j)	00 UTC September 08, 2006	SN	108.16	Yes
(k)	00 UTC September 12, 2006	SN	83.62	No
(l)	00 UTC September 27, 2006	SN	96.19	No

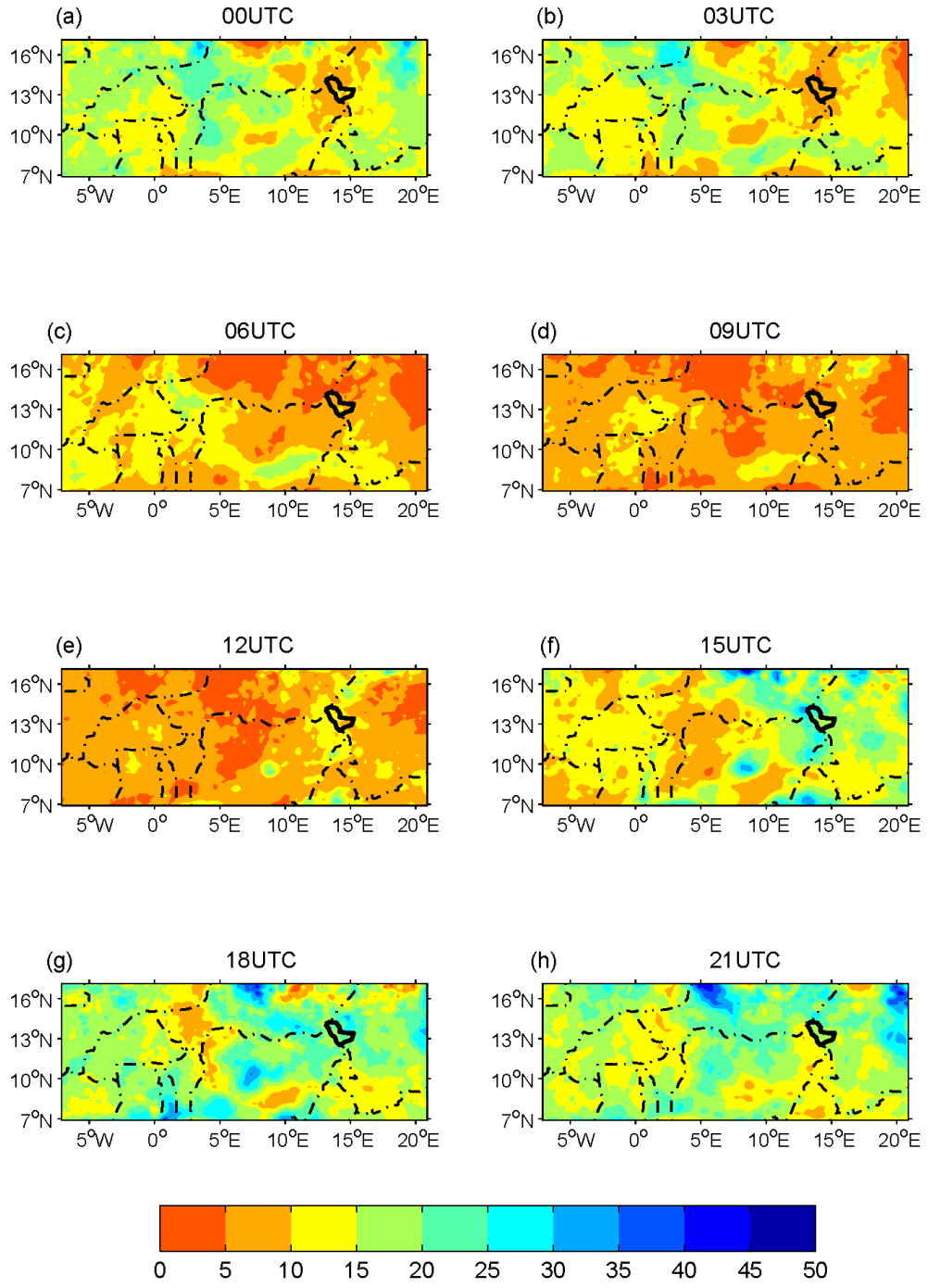

Figure 2.1. Diurnal distribution of rainfall percentage at 3-hourly intervals from June-September (JJAS) climatology (1998-2013). Dash-dot lines indicate the political boundaries.

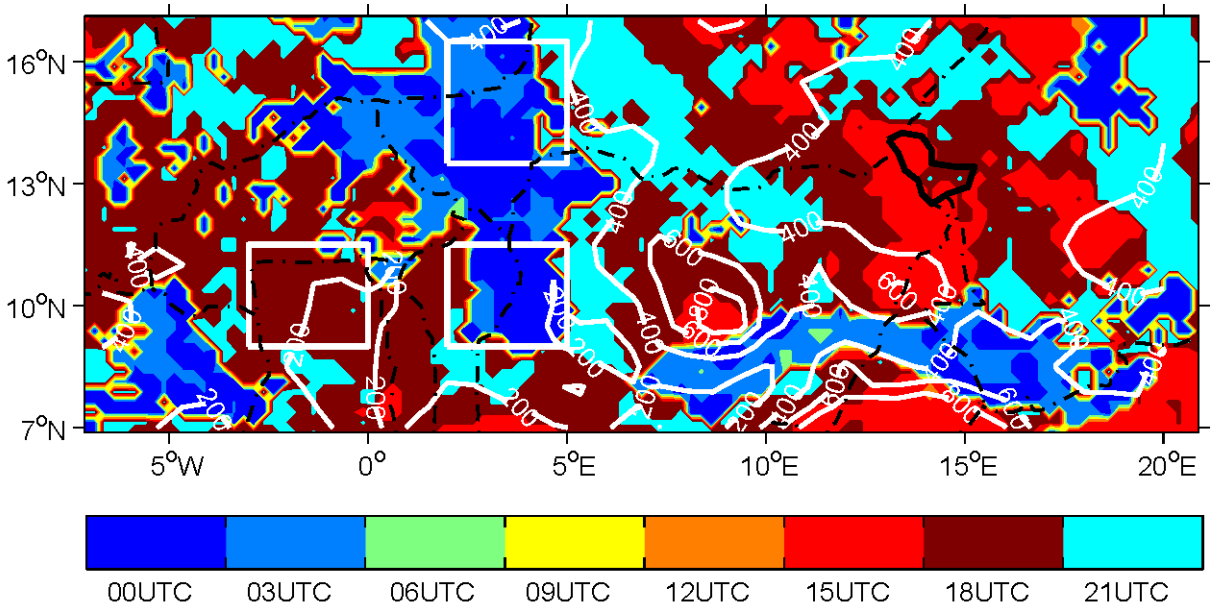

Figure 2.2. Hour of maximum rainfall from the TRMM JJAS climatology (1998-2013). White contours show elevation (m). Boxes denote the three averaging domains defined for further analysis: AF (short for "afternoon", 3°W-0°W, 9°N-11.5°N) with late afternoon rainfall peaks; SN (short for "southern nocturnal", 2°E-5°E, 9°N-11.5°N); and NN (short for "northern nocturnal", 2°E-5°E, 13.5°N-16.5°N) with nocturnal rainfall peaks .

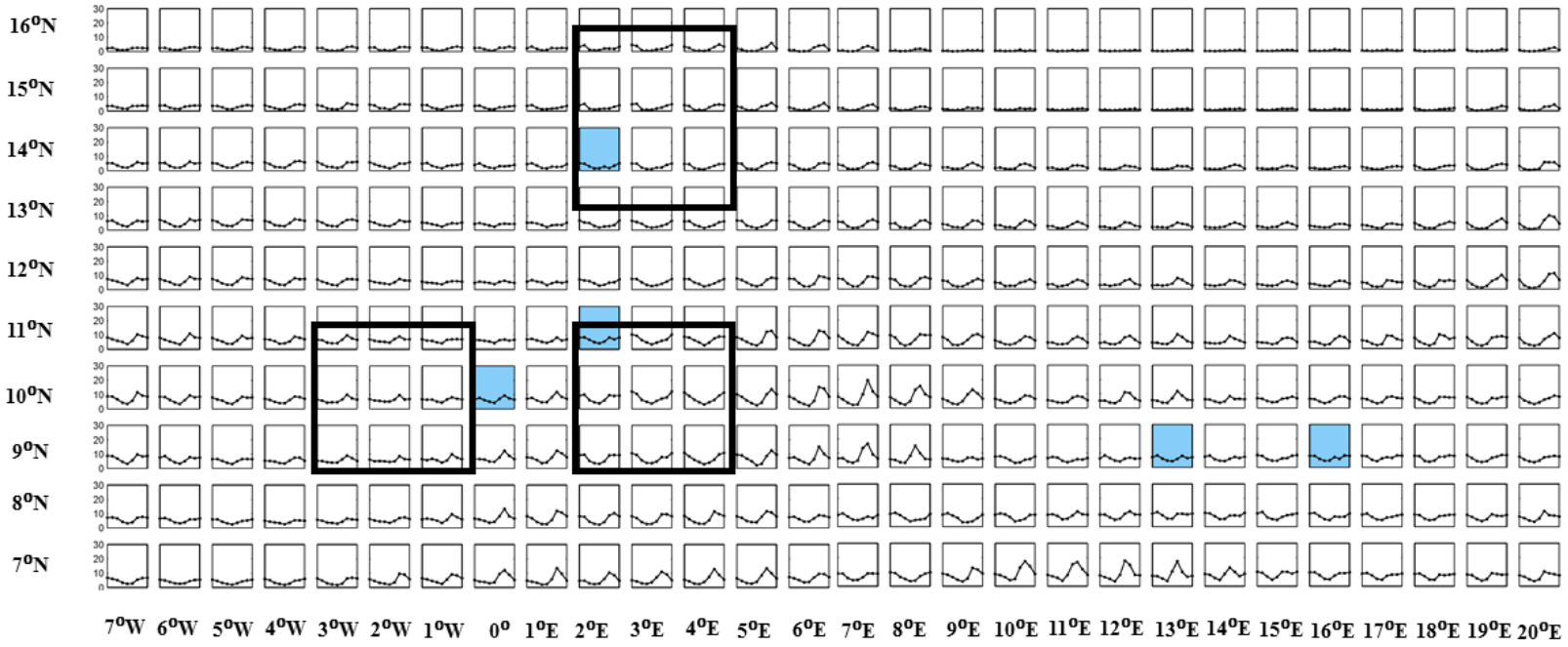

Figure 2.3. Diurnal cycle of climatological JJAS rainfall (mm day^{-1}) area-averaged for 1°×1° grid boxes within the region of 7°W-21°E, 7°N-17°N. Grid boxes with multiple diurnal peaks of rainfall are shaded in blue. Boxes denote the three domains defined in Figure 2. The x-axis of each panel ranges from 00 UTC to 24 UTC at 3 hour intervals. A peak is defined as at least 1 mm day^{-1} higher than its neighbor times.

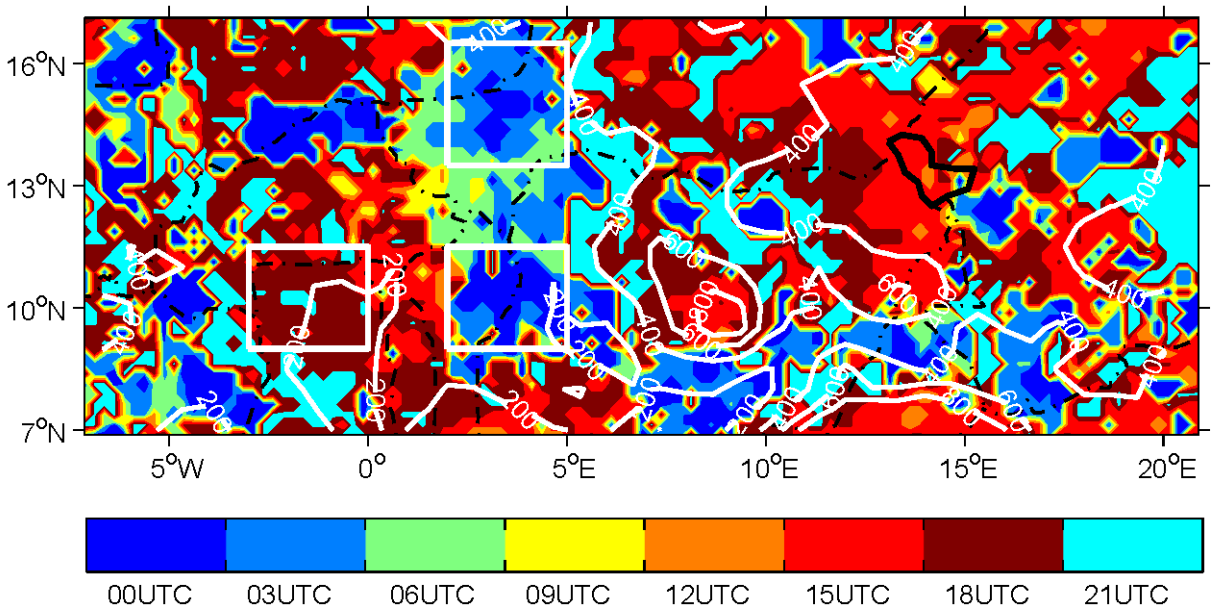

Figure 2.4. Peak hour of rainfall from the JJAS 2006 mean. White contours show elevation (m). Boxes denote the three domains defined in the text.

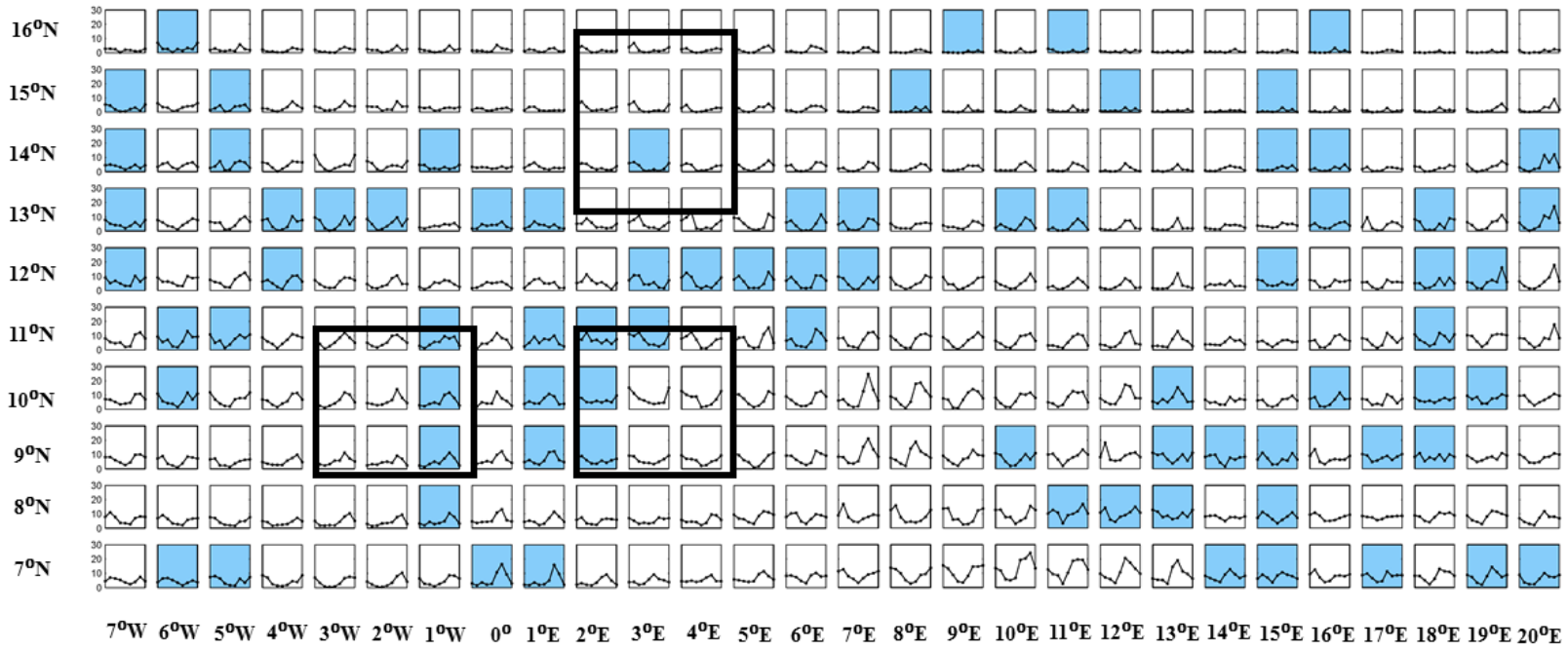

Figure 2.5. Same as Figure 2.3, but for JJAS of 2006 in TRMM. Bold boxes denote the three domains defined in the text. The x-axis of each panel ranges from 00 UTC to 24 UTC at 3 hour intervals.

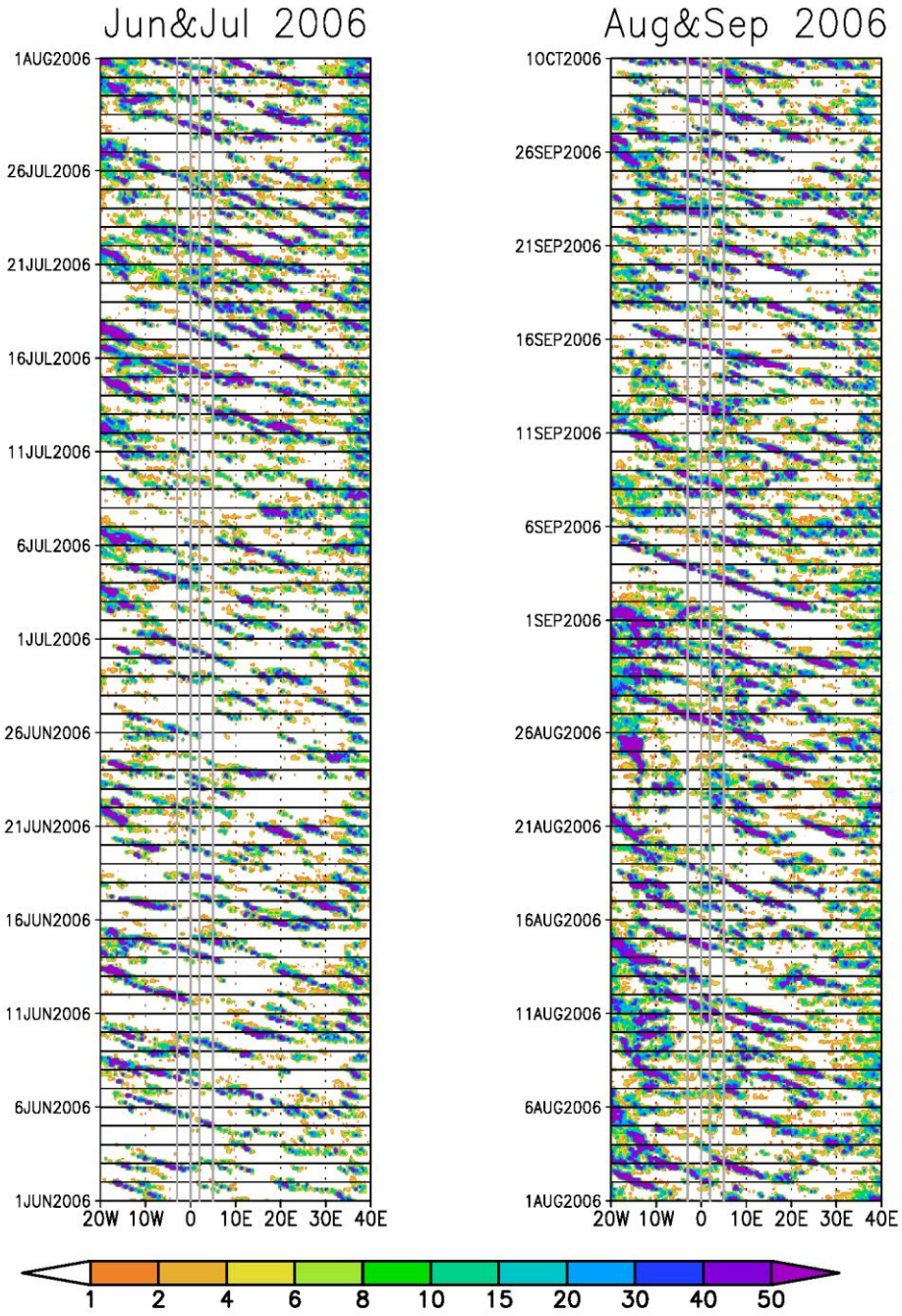

Figure 2.6. Hovmöller diagram of TRMM 3-hourly rainfall (mm day^{-1}) averaged between 9°N-11.5°N for (a) June and July and (b) August and September of 2006. Grey lines denote the boundaries of the AF (3°W and 0°W) and SN (2°E and 5°E) domains.

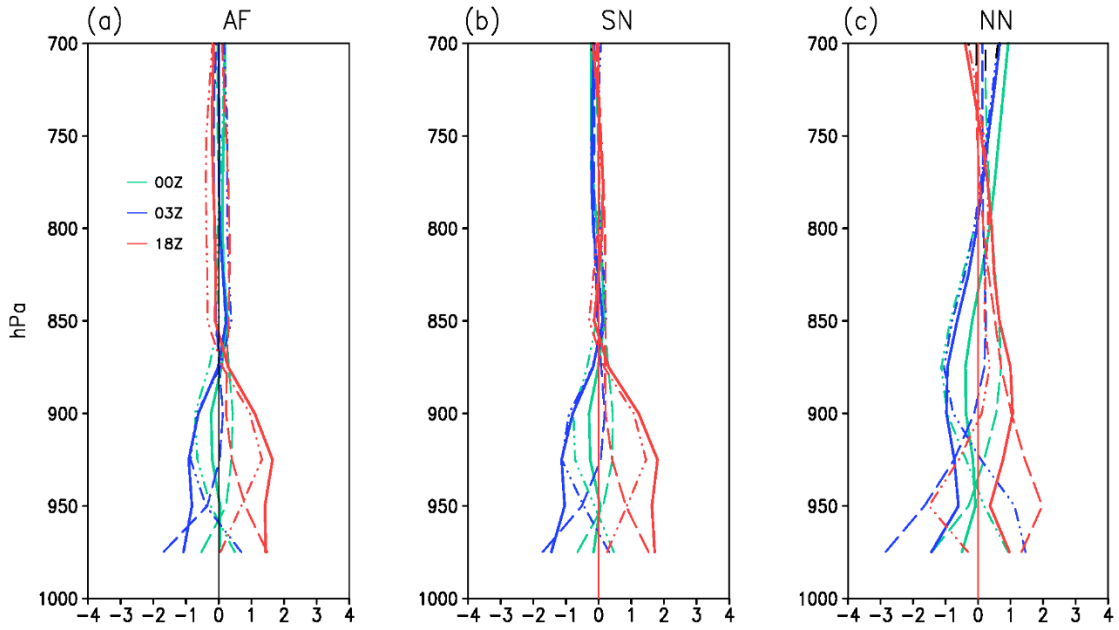

Figure 2.7. (a) Profiles of total MSE (solid lines; units: 10^3 m^2 s^{-2}), c_pT (dashed lines), and Lq (dot-dashed lines) anomalies averaged over the AF domain at 00 UTC (green), 03 UTC (blue), and 18 UTC (red). (b) and (c) are the same as (a) but for the SN and NN domains, respectively. Units are 10^3 m^2 s^{-2}.

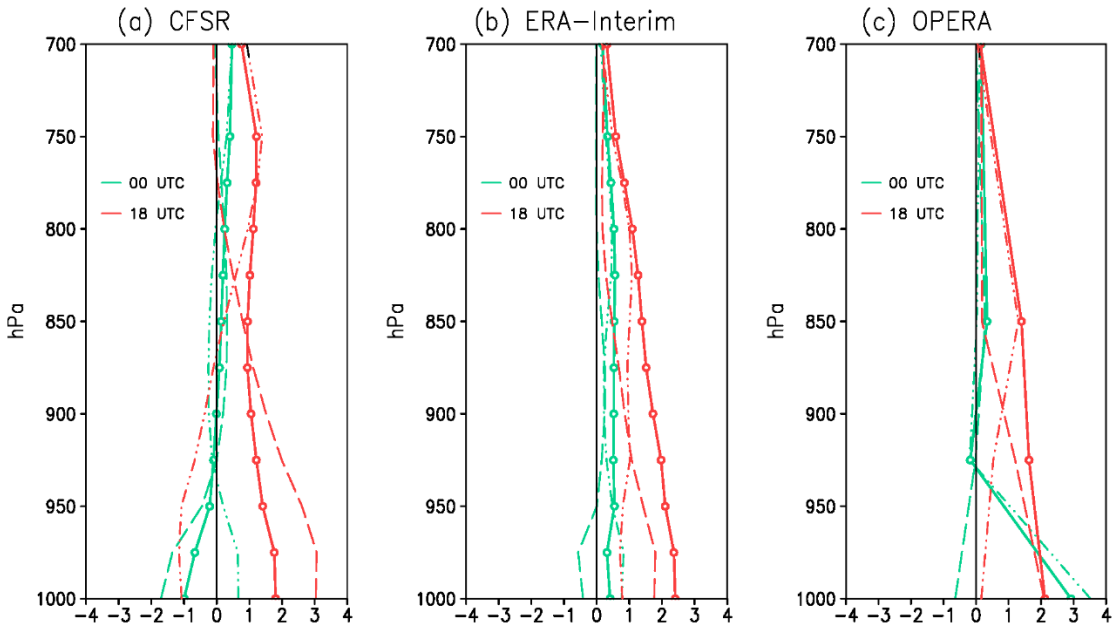

Figure 2.8. Same as Figure 2.7a, but for (a) CFSR, (b) ERA-Interim, and (c) ECMWF-OPERA at 00 UTC and 18 UTC.

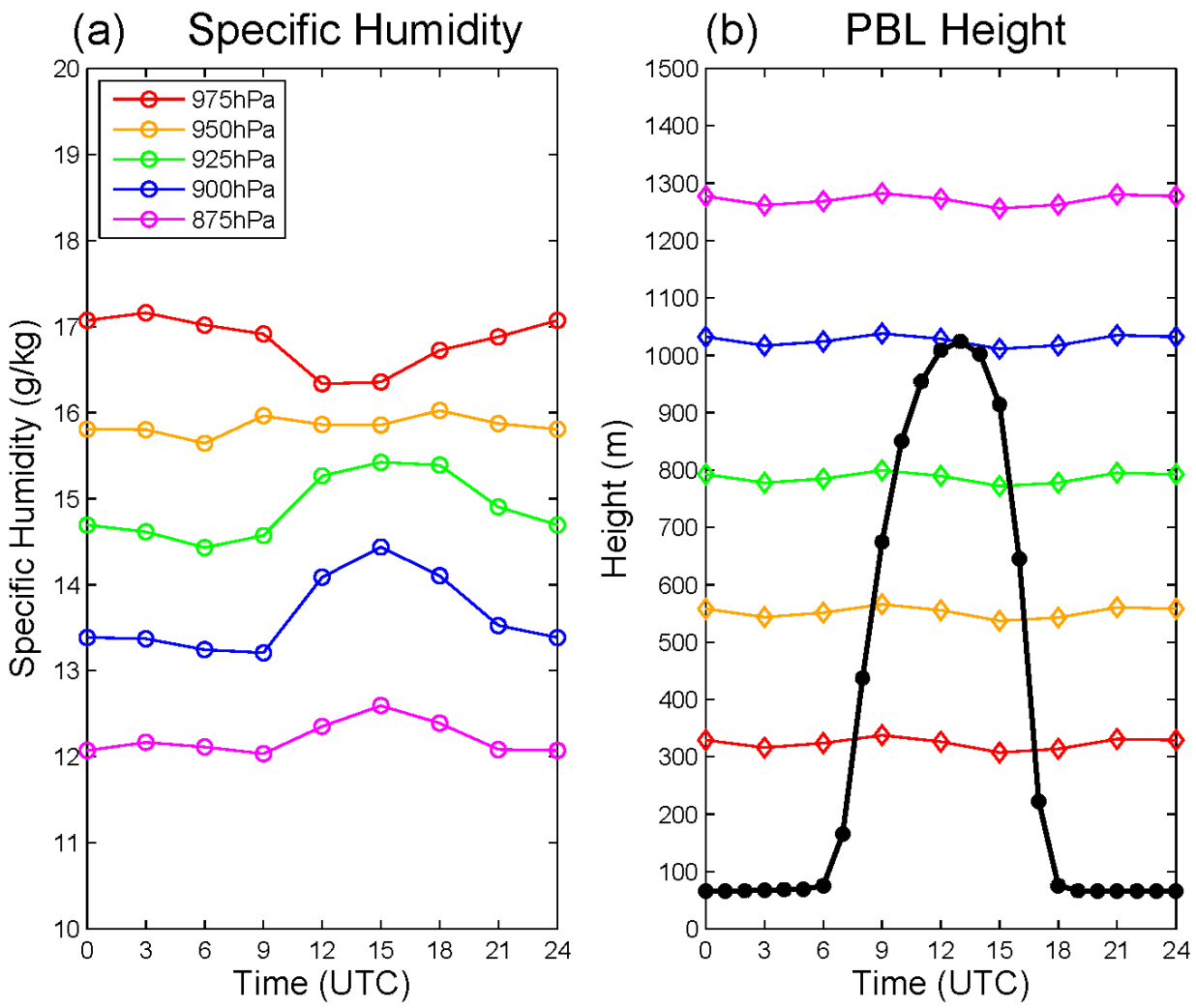

Figure 2.9. JJAS 2006 AF domain mean diurnal cycle of (a) low-level specific humidity (g kg^{-1}) and (b) geopotential height (color lines, units: m) and planetary boundary layer (PBL) height (bold line, units: m) in MERRA reanalysis.

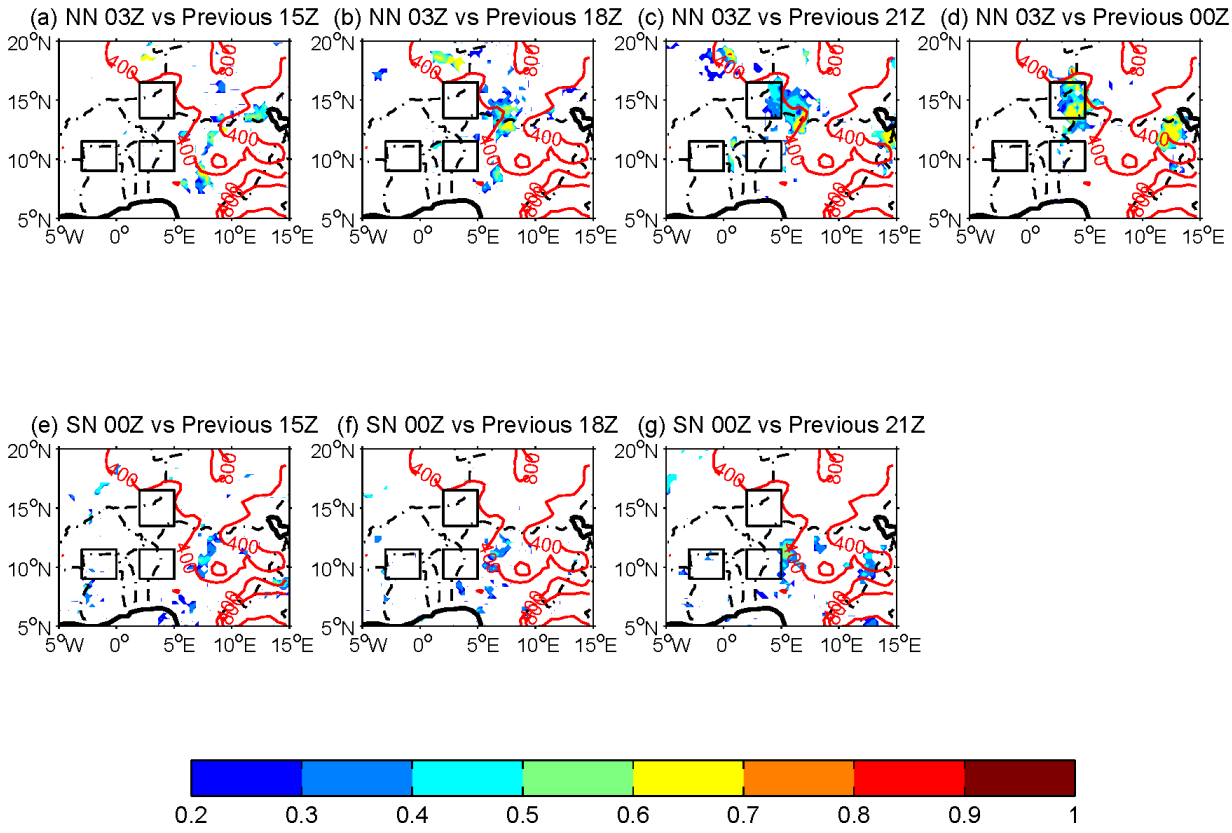

Figure 2.10. Correlation maps relating the JJAS 2006 time series of 03 UTC rainfall averaged over the NN domain and the rainfall time series of each grid point at previous (a) 15 UTC, (b) 18 UTC, (c) 21 UTC, and (d) 00 UTC. (e)-(g) same as (a)-(d) but for the SN domain time series of 00UTC rainfall correlated with the rainfall time series of each grid point at previous 15 UTC, 18 UTC, and 21 UTC, respectively. Only positive correlation coefficients statistically significant at the 99% confidence level are shown. Elevation is shown as red contours for 400 m and 800 m.

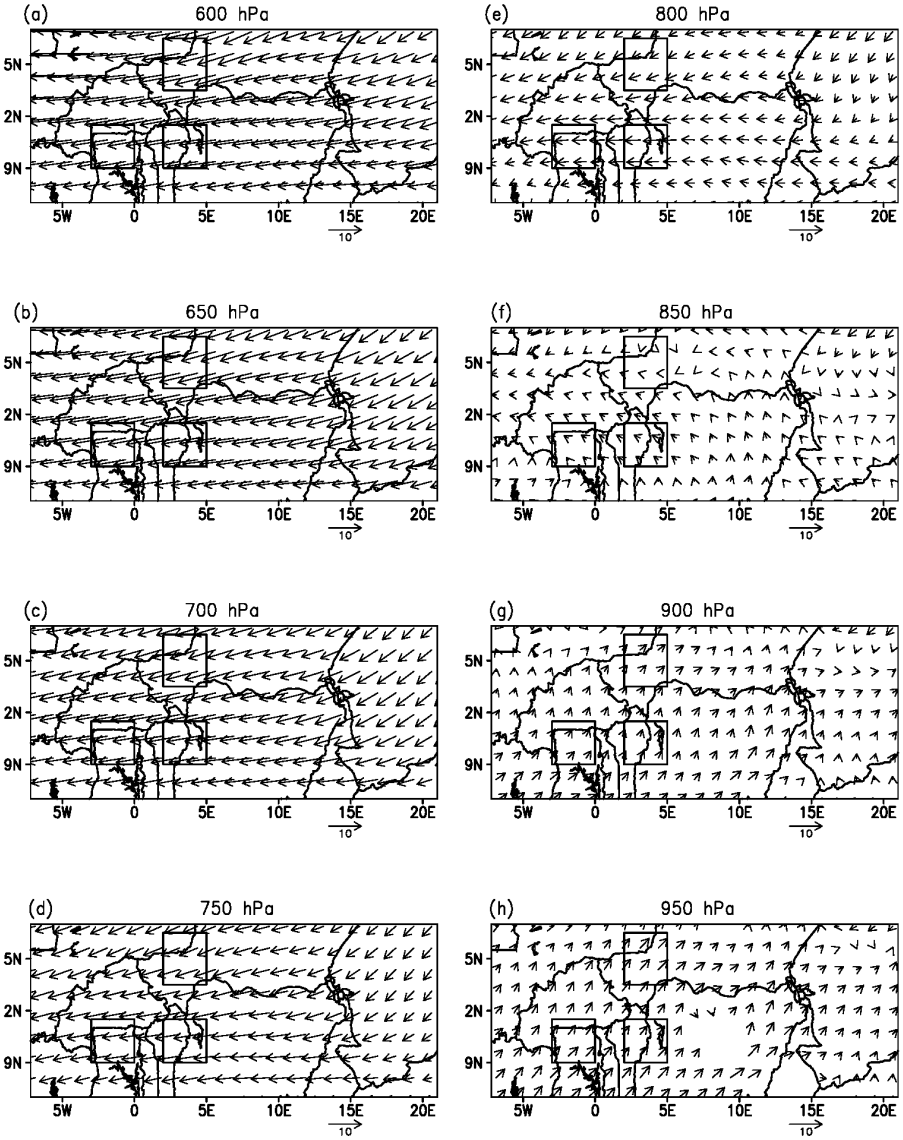

Figure 2.11. JJAS 2006 seasonal mean wind (m s^{-1}) in the MERRA reanalysis in the lower troposphere from 600 hPa to 950 hPa at 50 hPa intervals, from (a) to (h).

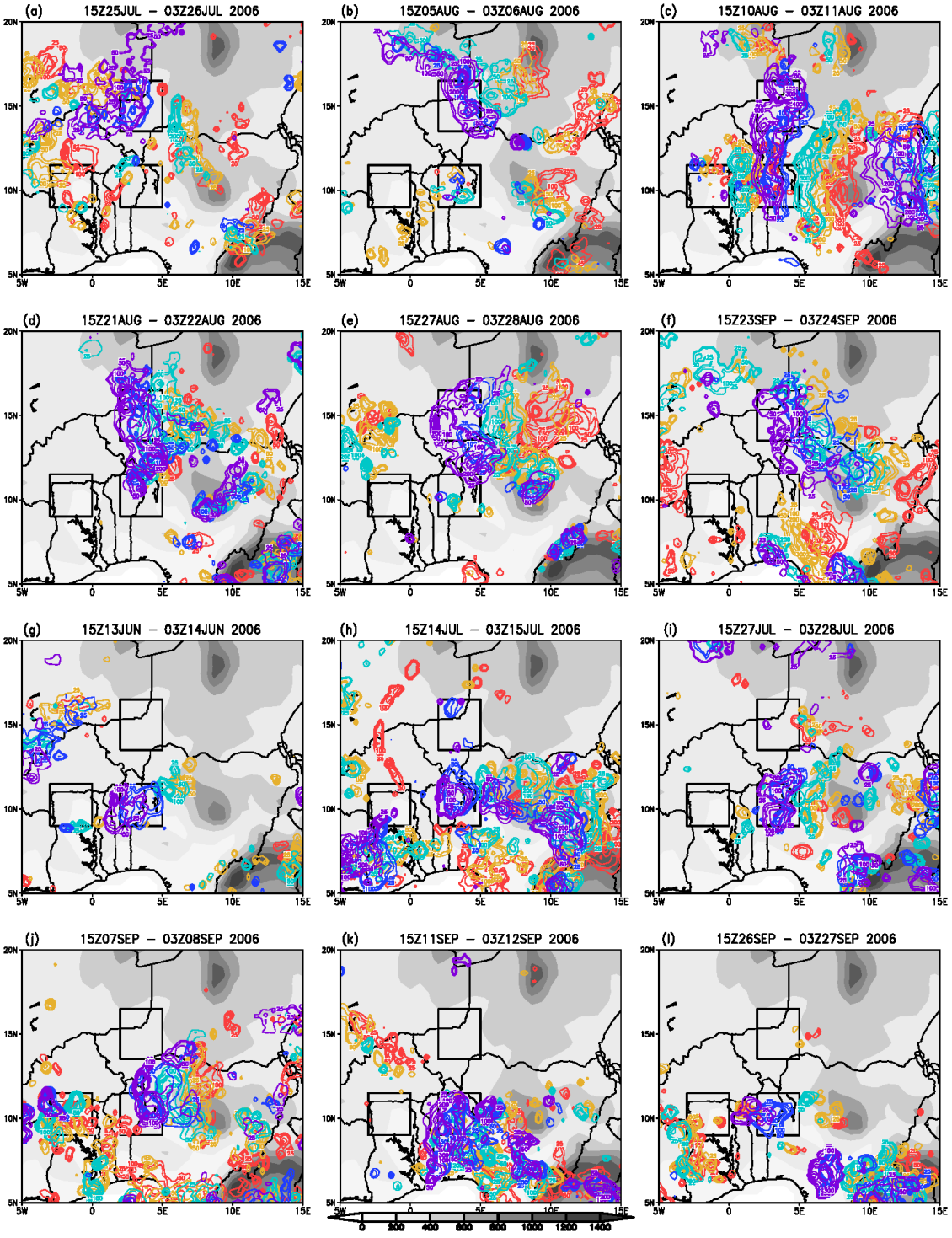
(a) 15Z25JUL – 03Z26JUL 2006
(b) 15Z05AUG – 03Z06AUG 2006
(c) 15Z10AUG – 03Z11AUG 2006
(d) 15Z21AUG – 03Z22AUG 2006
(e) 15Z27AUG – 03Z28AUG 2006
(f) 15Z23SEP – 03Z24SEP 2006
(g) 15Z13JUN – 03Z14JUN 2006
(h) 15Z14JUL – 03Z15JUL 2006
(i) 15Z27JUL – 03Z28JUL 2006
(j) 15Z07SEP – 03Z08SEP 2006
(k) 15Z11SEP – 03Z12SEP 2006
(l) 15Z26SEP – 03Z27SEP 2006
20N
15N
10N
5N
5W
0
5E
10E
15E
0 200 400 600 800 1000 1200 1400

Figure 2.12.

Figure 2.12. Propagation of rainfall during 12 extreme events during JJAS 2006 (see Table 1 for details) over the NN and SN domains. Rainfall contours at the same time are plotted in the same color using intervals of 50, 100, and 200 mm day^{-1}. Color legend is: red for 15 UTC, yellow for 18 UTC, cyan for 21 UTC, deep blue for the following 00 UTC, and purple for the following 03 UTC. Elevation (m) is shaded as background.

Chapter 3: The Diurnal Cycle of Warm Season Rainfall over West Africa: Convection-permitting Simulations

ABSTRACT

Convection-permitting simulations using a regional climate model are analyzed to improve the understanding of the diurnal cycle of rainfall over West Africa and its underlying physical processes. The warm season of 2006 is used for the model simulations. The model has a good performance of seasonal mean rainfall and lower-troposphere circulation and captures the observed westward propagation of rainfall systems. The majority of the West Africa shows a single diurnal peak of rainfall in these simulations in agreement with the observation. However, the number of rainfall systems is more than twice of the observations, which is related to an overestimation of the initiation of afternoon rainfall over elevated topography. The simulations also produce shorter lived rainfall systems and their propagation speed is slightly faster than the observation.

The model captures the afternoon rainfall peaks associated with elevated topography, e.g., the Jos Plateau. Nocturnal rainfall peaks downstream of the topographic afternoon rainfall are also well-simulated. However, the model generates too widespread nocturnal rainfall peaks and fails to reproduce the observed afternoon rainfall peaks over regions not associated with topography. This deficiency is related to a higher planetary boundary layer (PBL) than the observation which elevates the unstable profile to a higher level and inhibit the development of afternoon convections for the regions far away from topography. This study highlights that increasing the model resolution to convection-permitting scale improves the diurnal cycle of rainfall compared with the models with parameterized convection, but is not sufficient to fully resolve the issue.

3.1. INTRODUCTION

This paper is the second part of a study that aims to improve our understanding of the diurnal cycle of warm season rainfall over West Africa. Here we follow an observational study (Zhang et al. 2015b) with an analysis of high-resolution simulations.

Atmospheric models, including both general circulation models (GCMs) and regional climate models (RCMs), are primary tools for predicting rainfall from sub-synoptic to multi-decadal time scales. The diurnal cycle of precipitation is a critical aspect of the regional climatology, and influences rainfall distributions on all time scales. In Part I (Zhang et al. 2015b) we provide an observational analysis of the diurnal cycle of rainfall over West Africa. We conclude that, despite previous studies indicating that there are two diurnal peaks in rainfall over West Africa, almost all regions have a single diurnal peak, either in the afternoon or at night, and two peaks only occur as a result of area averaging.

The purpose of this paper is to examine the ability of a regional, convection-permitting atmospheric model to reproduce the diurnal cycle of rainfall over West Africa and capture the underlying physical processes. The performance issues of the current generation of GCMs and RCMs in simulating the diurnal cycle of rainfall over West Africa are reviewed in section 2. Section 3 documents the regional climate model used in this study, including the configuration of the convection-permitting simulation. Observational and reanalysis data sets used to evaluate the model are also described in section 3. Results are presented in section 4, and conclusions are summarized in section 5.

3.2. BACKGROUND

Representing the diurnal cycle of rainfall over West Africa remains a challenging issue for the current generation of GCMs and RCMs. GCMs can often produce realistic simulations of the mean precipitation on monthly to annual timescales, but they fail to capture the diurnal cycle

of rainfall over West Africa (Cook and Vizy 2006; Dai 2006; Xue et al. 2010). For example, Dai (2006) compares the rainfall simulated by 18 different GCMs to TRMM observations and shows that over West Africa all the models initiate convective rainfall too early in the day (i.e., around local noon compared to late afternoon). In addition, the observed nocturnal rainfall peaks diagnosed in Zhang et al. (2015) are not captured by the GCMs. Recent efforts to improve convective parameterization in GCMs provide a better representation of the timing of convection (e.g., Rio et al. 2009, 2013; Bechtold et al. 2014), but the nocturnal rainfall peaks are still not represented well. Such misrepresentations undermine our confidence in the models' ability to properly represent the physical processes of precipitation, including those associated with high-impact extreme events.

Simply increasing a GCM's resolution is not sufficient for correcting inaccuracies in the simulation of the diurnal cycle of rainfall if the resolution is not fine enough to explicitly allow convective rainfall without the use of cumulus parameterization (Lee et al. 2007; Ploshay and Lau 2010; Dirmeyer et al. 2012). This inability suggests that the errors are at least partially associated with the parameterized physical processes that control rainfall production in the models.

One approach to avoiding the use of cumulus parameterization in models is to conduct convection-permitting simulations using spatial resolutions on the order of 4 km or finer. Sato et al. (2009) examine the dependence of the diurnal cycle of rainfall on spatial resolution in simulations with a global, convection-permitting model with 14-km, 7-km, and 3.5-km grid spacing. Over the tropical continents, the 3.5-km run produces realistic diurnal rainfall peaks in the afternoon and night, in both timing and magnitude, when compared with the TRMM observations. The 7-km and 14-km simulations produce 1.5 and 4.5 hour delays in the afternoon peak, respectively. Noda et al. (2012) suggest that these delays are associated with inaccuracies in the model's simulation of organized convective systems with radii less than 100 km. Dirmeyer et al. (2012) also show that a global convection-permitting model produces a more realistic

diurnal cycle of rainfall than global models with parameterized convection or an embedded two-dimensional convection-permitting model.

Convection-permitting simulations with GCMs are computationally expensive, especially for simulating seasonal or longer timescales. Regional climate modeling provides an efficient alternative. RCMs use the same set of governing equations as GCMs, but the use of a limited domain makes high resolution simulation practical and the constraint of requiring hydrostatic balance used in GCMs can be relaxed. In addition, the focus on a particular region can produce more accurate simulations when surface features such as topography are more accurately represented, and physical parameterizations (e.g., radiation calculations and land surface models) that are more suitable for the analysis region are selected (e.g., Cook and Vizy 2012; Vizy et al. 2013).

Pearson et al. (2013) and (Birch et al. 2014) examine the diurnal cycle of rainfall in regional model simulations with 4-km and 1.5-km resolution and explicit convection. These high-resolution simulations reproduce the dual peaks of precipitation observed over many regions of West Africa, including afternoon convection and nocturnal propagating features. A version of the same model with 12-km resolution and parameterized convection fails to produce nighttime peaks. The difference in the accuracy of the diurnal cycle of rainfall between the higher- and lower-resolution simulations is attributed to the treatment of convection (explicit vs. parameterized) and not directly to the resolution differences.

With preliminary testing to select physical parameterizations that work well in the region, the Weather Research and Forecasting (WRF) regional climate model (Skamarock et al. 2008) accurately reproduces West African rainfall on seasonal to interannual (e.g., Hagos and Cook 2007; Cook and Vizy 2012; Vizy et al. 2013; Crétat et al. 2014). Working on the synoptic time scale, Laing et al. (2012) conduct 4-km resolution WRF convection-permitting simulations over tropical northern Africa for 12.5 days during the summer of 2006. The model captures the diurnal cycle and other statistical properties of precipitation systems in the lee of the Ethiopian Highlands.

In Part I (Zhang et al. 2015b), an observational analysis shows that most regions of West Africa (98% in the climatology and 78% in a case study for 2006) have a single diurnal peak of rainfall in either the afternoon (i.e., 15 and 18 UTC) or at night (i.e., 21, 00, and 03 UTC). Two types of regions experience afternoon rainfall peaks. One is regions with topographic features, and the other is regions far removed from upstream topography. Coherent regions with nocturnal rainfall peaks are located 3°-10° of longitude downstream (i.e., to the west) of regions with afternoon rainfall maxima. These nocturnal rainfall maxima are associated with the westward propagation of rainfall systems, and not with local convective instability.

This paper builds on the observational analysis to further advance our understanding of the diurnal cycle of rainfall by examining convection-permitting simulations over West Africa. These simulations provide the opportunity to compare the model-simulated diurnal cycle of rainfall with observations to understand the extent to which the critical physical processes that control the diurnal cycle are represented accurately in the model.

3.3. METHODOLOGY

3.3.1 Description of the regional climate model simulations

The Advanced Research WRF (ARW) version 3.4.1 (Skamarock et al. 2008) model is used to conduct convection-permitting simulations over West Africa. We use 3-km horizontal resolution to explicitly resolve moist convection without the use of cumulus parameterization. A model domain encompassing the region bounded by 7°W-21°E and 7°N-17°N (985 longitude × 371 latitude gridpoints) is used. This domain covers the study region used in the observational analysis of Part I. Such a large domain is useful for reducing the impacts of the lateral boundary conditions on the model solution in the domain interior.

Due to the high computational demands of running a 3-km resolution simulation over a domain with 365,435 gridpoints, one summer, 2006, is selected for a case study. The simulation is initialized at 00 UTC on 1 March 2006 and run through 30 September 2006 and the warm

season (June to September) is analyzed. The summer of 2006 is chosen because it is representative of a typical summer season over West Africa, and it has been extensively studied as part of the African Monsoon Multidisciplinary Analysis (AMMA) special observing period (Lebel et al. 2010). This year is also used in the observational analysis conducted in Part I. The model integration time step is 15 seconds, and hourly model output is archived for analysis.

Initial and boundary conditions are taken from the 6-hourly National Centers for Environmental Prediction (NCEP) Climate Forecast System Reanalysis (CFSR, Saha et al. 2010), which has a horizontal resolution of 0.5° for atmospheric fields and 0.31° for surface fields. CFSR is chosen because of its high spatial resolution.

Physical parameterizations selected for use in the simulation include the Lin et al. microphysics scheme (Chen and Sun 2002), the RRTM longwave radiation scheme (Mlawer et al. 1997), the Dudhia shortwave radiation scheme (Dudhia 1989), the Yonsei University boundary layer scheme (Hong et al. 2006), the MM5 Monin-Obukhov surface layer scheme (Skamarock et al. 2008), and the Noah land surface model (Chen and Dudhia 2001). This combination of parameterizations has been shown to reproduce the West African climate realistically at various spatial resolutions greater than 10-km (Cook and Vizy 2012; Vizy et al. 2013). The cumulus convection parameterization is disabled.

The above simulation is the default simulation used in this study, and its results are presented in next section. To verify that the diurnal cycle of rainfall produced in the default simulation is due to the internal model physics rather than being injected into the model domain by the lateral boundary conditions, an additional simulation was run with the diurnal cycle filtered out of the lateral boundary conditions. The diurnal cycle of rainfall throughout the model domain is insensitive to this filtering.

Analysis of the output from the default simulation raised concern about a dependence on the atmospheric boundary layer and cloud microphysics parameterizations. Therefore, two additional 3-km resolution simulations are conducted. The first sensitivity simulation is run in the same manner as the default except the Mellor–Yamada–Janjić (MYJ, Janjić 1994)

atmospheric boundary layer scheme is used instead of the Yonsei University boundary layer scheme. The second sensitivity simulation uses the Thompson microphysics scheme (Thompson et al. 2004) instead of the Lin et al. microphysics scheme. The results of these sensitivity simulations are discussed in the results section.

3.3.2 Description of the observational/reanalysis data sets

Several observational/reanalysis data sets are used to evaluate the modeled diurnal cycle of rainfall and various atmospheric fields. For rainfall, we use the 3-hourly Tropical Rainfall Measuring Mission (TRMM) precipitation 3B42V7 product (Huffman et al. 2007) and the 3-hourly Precipitation Estimation from Remote Sensing Information using Artificial Neural Network (PERSIANN) rainfall data (Sorooshian et al. 2000). Both have a spatial resolution of 0.25°.

The 3-hourly Modern-Era Retrospective Analysis for Research and Applications (MERRA, Rienecker et al. 2011) reanalysis is used for evaluating the atmospheric fields on diurnal time scales. At the time of this study, MERRA is the only reanalysis product that supplies atmospheric fields on 3-hourly intervals over West Africa. Other reanalyses are also used for model evaluation on longer time scales, including the National Centers for Environmental Prediction (NCEP) Climate Forecast System Reanalysis (CFSR) and the ECMWF ERA-Interim reanalysis (Dee et al. 2011). These products are available at 6-hourly intervals for 00 UTC, 06 UTC, 12 UTC and 18 UTC.

3.4. RESULTS

3.4.1 Evaluation of seasonal mean climate

The model's ability to simulate the seasonal mean low-level circulation and rainfall fields is first examined. Figure 1 compares the model simulated 925 hPa wind and specific humidity with reanalyses. The full domain of the simulation (7°W-20°E and 7°N-17°N) is shown. The

southwesterly monsoon flow is well-captured in the WRF model. The model also captures the spatial distribution of specific humidity at 925 hPa. The model simulated specific humidity agrees well with CFSR, which is the source of boundary conditions for the WRF convection-permitting simulation, and these two are dryer than MERRA and ERA-Interim over the southern part of the domain. Figure 2 examines the 650 hPa wind and specific humidity. The prevailing easterly flow is simulated by the WRF model. The zonal structure of the specific humidity in the model is also close to the reanalyses, especially CFSR as expected. Other levels in the lower troposphere are also examined (not shown) to conclude that the WRF convection-permitting simulation reasonably captures the seasonal mean dynamics fields of the lower troposphere.

Figure 3a-c display the JJAS 2006 mean rainfall rate from TRMM, PERSIANN and the WRF convection-permitting simulation, respectively. TRMM and PERSIAAN show similar seasonal mean rainfall. The model captures the meridional gradient of the seasonal rainfall reasonably well. South of 13°N, the model also captures the observed zonal structure, with drier conditions west of the Greenwich meridian and wetter conditions to the east. The rainfall maxima located near the Jos Plateau is also shown in the convection-permitting simulation. However, the model produces stronger rainfall than is observed over most of the southern part of the domain (2°W-19°E, 7°N-12°N) and weaker rainfall in the north (15°N-17°N).

3.4.2 Diurnal cycle of rainfall in the simulation

Figure 4 displays the percentage of daily rainfall distributed into each 3-hourly intervals in JJAS 2006. Similar to the observational analysis in Part I (Zhang et al. 2015b), UTC is used as the local time of this domain. The anomalously high percentage of afternoon rainfall along the boundaries are neglected because it is a common problem related to the forcing of lateral boundary conditions in the RCMs. For the West African region (west of 10°E), the afternoon rainfall starts around the Jos Plateau (7°E-10°E, 9°N-11.5°N) at 16-19 UTC and other regions at 19-22 UTC. The percentage of rainfall then decreases at 22-01 UTC and 01-04 UTC, then there

is few rainfall during the early morning and noon/early afternoon time. The afternoon maxima in the TRMM observations (Figure 1 in Part I) are delayed to the evening in the model. The nocturnal rainfall after midnight is weaker in the model than the observation.

Figure 5 shows the observed and model simulated peak hour of rainfall in the mean diurnal cycle of JJAS 2006. To compare with TRMM (Figure 5a), the model simulated hour of maximum rainfall is first evaluated in the 1-hourly output, and then rounded to the closest 3-hourly interval at the TRMM reporting times (Figure 5b). In contrast to TRMM, the model produces nocturnal peaks that dominate across West Africa except in some isolated areas, e.g., the Jos Plateau. We continue using the regions defined in Part I (Zhang et al. 2015b) for case studies and then generalize the findings: the AF domain (3°W-0°W, 9°N-11.5°N), the SN domain (2°E-5°E, 9°N-11.5°N), and the NN domain (2°E-5°E, 13.5°N-16.5°N). To explore the role of the Jos Plateau in shaping the diurnal cycle of rainfall, here we add another domain for the Jos Plateau (7°E-10°E, 9°N-11.5°N). The simulated rainfall peaks are mainly nocturnal in the AF region, which has afternoon peaks in the TRMM observations. The SN domain has realistically-simulated nocturnal rainfall peaks. The transition of rainfall peak hours from 18 UTC over the Jos Plateau to 03 UTC over the SN domain indicates a westward propagation of rainfall systems. This westward propagation agrees with the conclusions identified in the observational analysis. The NN domain contains nocturnal peaks in the southern half and afternoon peaks in the northern half where the model has a dry bias with rainfall rates below 1 mm/day (Figure 3). The two sensitivity simulations using different PBL and microphysics parameterizations show similar results (not shown) to the default simulation, indicating that alternating these parameterizations is not sufficient to improve the model simulation of the diurnal cycle of rainfall.

In general, the convection-permitting simulation captures the afternoon rainfall peaks associated with elevated topography, e.g., around the Jos Plateau. The nocturnal rainfall peaks in the downstream of the topographic afternoon rainfall is also well-simulated. Nevertheless, the regional model generates nocturnal rainfall peaks that are too widespread over the domain, and

fails to reproduce the observed afternoon rainfall peaks over regions that are more than a few hundred kilometers downstream of elevated topography.

To further explore the spatial variations of the diurnal cycle of rainfall, Figure 6 displays the model simulated diurnal cycle of rainfall which is area-averaged over 1°×1° grid boxes from 7°W to 21°E and 7°N to 17°N. 59% of the small regions show a single peak, while 29% exhibit double peaks. This agrees with the observations (Figure 5 in Part I) that the majority of these small regions experience a single diurnal peak of rainfall. Also note that the model has a dry bias to the north of 14°N; therefore the multiple peaks close to the northern boundary are related to the relatively small magnitude.

Figure 7 show the JJAS 2006 mean diurnal cycle of rainfall area-averaged for Joes Plateau, SN, and AF domains from TRMM observation and the convection-permitting simulation. Note that the TRMM data has 3-hourly intervals while the model output are archived at 1-hourly intervals. Therefore, if the difference of peak hour between observation and model simulation is less than 3 hours, the model has a good performance. For the Jos Plateau, the observed rainfall peak (at 18 UTC) is well-captured by the model (at 17 UTC). The magnitude of the diurnal cycle is much larger in the model and the rainfall maximum is twice in the model as in the observation.

Over the SN domain, similar to the observation, the model shows a nocturnal rainfall peak around midnight (at 02 UTC) which is close to the 00 UTC peak in the observation and also the magnitude of the peak in the model is doubled compared with the observation. However, for the AF domain, the observed afternoon rainfall peak (at 18 UTC) is not reproduced by the model. The model simulates a delayed peak at 23 UTC, but the magnitude of the peak is comparable to the observation.

3.4.3 Physical processes

Figure 8 and 9 display Hovmöller diagrams of the JJAS 2006 rainfall averaged 9°N-11.5°N from TRMM and the WRF convection-permitting simulation. One prominent feature is that the westward-propagating nature of rainfall systems is captured in the simulation. As discussed in section 2, GCMs and coarser-resolution RCMs with parameterized convection tend to simulate static afternoon rainfall without westward propagation, which results in missing the nocturnal rainfall peaks. Here, the well-simulated westward propagation of rainfall is a promising improvement toward advancing the representation the diurnal cycle of rainfall in climate models.

Afternoon rainfall systems are frequently initiated near 9°E, indicating that the model realistically simulates the afternoon rainfall related to the topography of the Jos Plateau. These systems propagate westward into the SN region, similar to the findings in TRMM, resulting in the realistic timing of rainfall peaks in the SN domain (Figure 5). However, the model produces too frequent initiation of afternoon rainfall around the Jos Plateau. The total number of propagating rainfall events in the model is more than twice in the observation (Table 1).

In the AF domain, the model simulates intense propagating rainfall systems passing through it during evening and night, and this causes the misrepresentation of the diurnal cycle of rainfall in that region. There is no secondary afternoon peak in the AF domain that is comparable to the observations. A similar Hovmöller diagram for simulated rainfall at the NN domain latitudes (13.5°N-16.5°N, not shown) exhibits few events and a low rainfall rate, failing to reproduce the diurnal cycle of rainfall over the northern part of the domain.

The statistics of the propagating rainfall systems are summarized in Table 1. Generally, the number of rainfall systems generated in the model is more than twice of that in the observations, which is caused by an overestimation of the initiation of afternoon rainfall around the Jos Plateau. In addition to the doubled frequency of rainfall events, The WRF model produces shorter lived rainfall systems and their propagation speed is slightly faster than that observed in TRMM.

Figure 10 shows the large-scale low-level circulation for the Jos Plateau region between model simulation and reanalyses. The model simulated low-level flow matches well with reanalyses, indicating that the overestimation of afternoon rainfall initiation is not caused by a bias in the low-level circulation. Next in Figure 11, we examine the instability of the lower troposphere suggested by afternoon MSE profiles averaged over the region (8.3°E-8.8°E, 9.5°N-10°N) to the downstream (i.e., west) of the top of Jos Plateau. The MERRA reanalysis shows unstable MSE profile from 850 hPa above and the MSE profile gradually becomes neutral. The model simulated MSE anomaly profile is neutral from surface to 850 hPa and then becomes unstable above 850 hPa. Especially, the simulated MSE anomaly profile is more unstable than the reanalysis from 800 hPa above. Note that this region is to the downstream (i.e., west) of the top of Jos Plateau, the disturbances generated on the top of Jos Plateau are elevated at levels above 850 hPa and then propagated into this region. Therefore, these topographical disturbances enter at levels with favorably unstable profile for the development of deep convections. The more unstable MSE anomaly profile in the model helps to explain the more frequent initiation of afternoon convections over this region than observation.

For the AF domain, as suggested in section 2, the observed afternoon peak of rainfall is not captured by the WRF convection-permitting simulation. Instead, the model produces a nocturnal rainfall peak. Generally, this delay of the afternoon peaks is a common problem across the model domain for regions not affected by topographic rainfall. Figure 12 display the MSE anomaly profiles for the AF domain in MERRA and the WRF model simulation. In the low levels from surface to 850 hPa, the model produced MSE anomaly profile is close to natural while MERRA shows an unstable profile. Although the model shows similar unstable profile from 850 hPa to 750 hPa, it is difficult for the afternoon convections to break the neutral layers in below to form deep convections. In general, the afternoon rainfall peaks in the model is not well-captured because the model produce less favorable instability profile for the generation of afternoon convections.

By separating the contribution of temperature and moisture terms to the total MSE (dashed and dot-dashed lines in Figure 12), it is obvious that the MSE anomaly profile is stabilized by a maximum of atmospheric moisture at 850 hPa. Figure 13a shows the diurnal cycle of low-level specific humidity for the AF domain. The increase of moisture in the afternoon at 850 hPa and 800 hPa is similar to the MERRA reanalysis (Figure 9a in Part I). Figure 13b displays the diurnal cycle of PBL height simulated by the WRF model. Compared with MERRA (Figure 9b in Part I), the model produces a much higher PBL top up to 1500 m. Therefore, the vertical mixing is stronger around the levels of the model simulated PBL, e.g., 900 hPa and 850 hPa. This enhanced vertical mixing is associated with the moistening of these levels as shown in the MSE profiles.

In general, the WRF convection-permitting simulations produce a deeper PBL and more moisture than the observation in the low levels below 850 hPa, which stabilize the MSE profiles at these levels and elevate the unstable MSE profile at higher levels compared with observation. This vertical instability setting is unfavorable for the development of afternoon rainfall, except over the mountain regions where the disturbances originated from the top of mountain are propagated into the unstable levels that are favorable for convections.

3.5. CONCLUSIONS

Based on the physical understanding of the diurnal cycle of rainfall over West Africa in the observational analysis of Part I (Zhang et al. 2015b), in this paper we evaluate convection-permitting regional model simulations for the warm season of 2006 to further understand the physical processes that control the diurnal cycle of rainfall over West Africa.

We summarize the results from the convection-permitting regional model simulations as follows:

- The model realistically simulates seasonal mean rainfall and lower-troposphere circulation fields. Moreover, the westward propagating nature of rainfall is well-captured

in the convection-permitting simulations, which is a distinct advantage compared to the rainfall simulated in GCMs or RCMs at coarser resolutions with convective parameterization activated.

- The model produces a single diurnal peak of rainfall over the majority of West Africa, which agrees with the observation. The number of simulated rainfall systems is more than twice of the observations, which is caused by an overestimation of the initiation of afternoon rainfall around the Jos Plateau. The model also produces shorter lived rainfall systems and their propagation speed is slightly faster than that observed in TRMM.
- The model captures the afternoon rainfall peaks associated with elevated topography, e.g., around the Jos Plateau. Nocturnal rainfall peaks downstream of the topographic afternoon rainfall are also well-simulated.
- The model fails to reproduce the observed afternoon rainfall peaks over regions not with topography. Nocturnal rainfall is too widespread. The reason is that the model has a deeper PBL than the observation. Model simulated unstable afternoon MSE anomaly is located at a higher altitude than the observation, and underneath MSE anomaly is nearly neutral. This MSE profile inhibits the development of afternoon convection over most of regions with no topographic features. To the opposite, in the downstream (i.e., west) of the top of Jos Plateau, this MSE profile is favorable for initiation of afternoon convections, because the disturbances propagated from the top of plateau are elevated above the neutral levels and located at the unstable levels.

An improved understanding of the diurnal cycle of rainfall is important for advancing weather and climate prediction over West Africa. This study demonstrates that atmospheric models running at convection-permitting resolutions improves the representation of the diurnal cycle of rainfall, compared with GCMs and coarser resolution RCMs with parameterized convection. However, increasing the model resolution to a convection-permitting resolution (e.g., 3 km) still cannot fully solve the problem. The diurnal cycle of rainfall simulated by the

model always depends on the parameterization of various physical processes, e.g., the cloud microphysics, PBL, etc. The representation of these physical processes is critical in determining the timing of convections and therefore diurnal cycle of rainfall.

Table 3.1. Statistics of the propagating rainfall systems in TRMM and the WRF convection-permitting simulation.

	TRMM	WRF simulation
Total Number of propagating systems	163	337
Mean duration of propagation (hour)	24.3	17.1
Mean propagation speed (m/s)	12.4	14.7

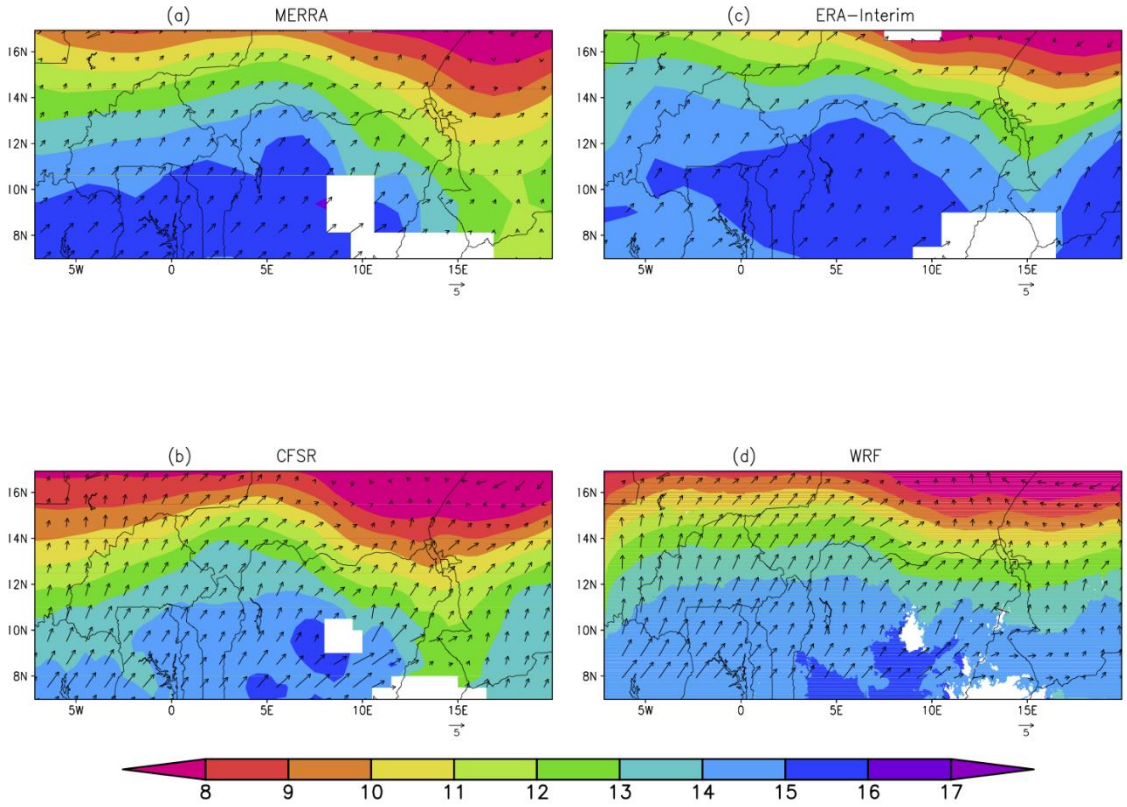

Figure 3.1. JJSA 2006 mean 925 hPa specific humidity (shaded, units g kg^{-1}) and wind (vectors, units m s^{-1}) in (a) MERRA, (b) CFSR, (c) ERA-Interim, and (d) the WRF convection-permitting simulation.

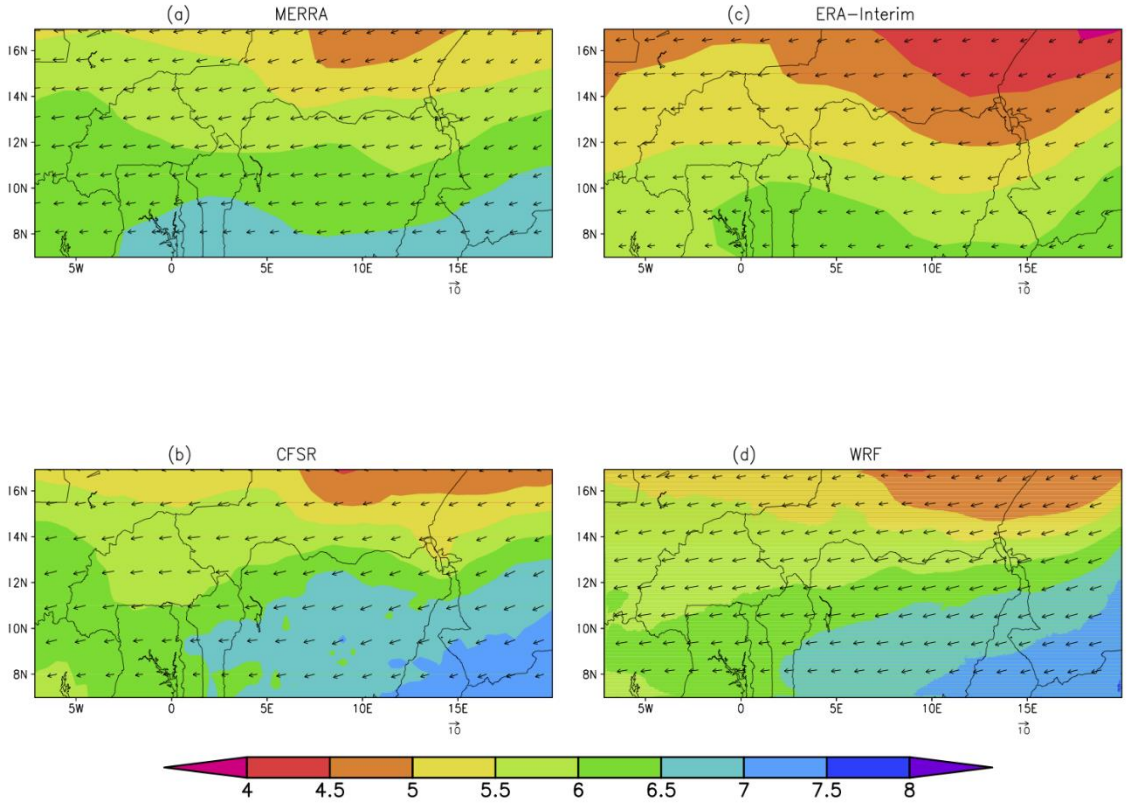

Figure 3.2. Same as Figure 3.1, but for 650 hPa.

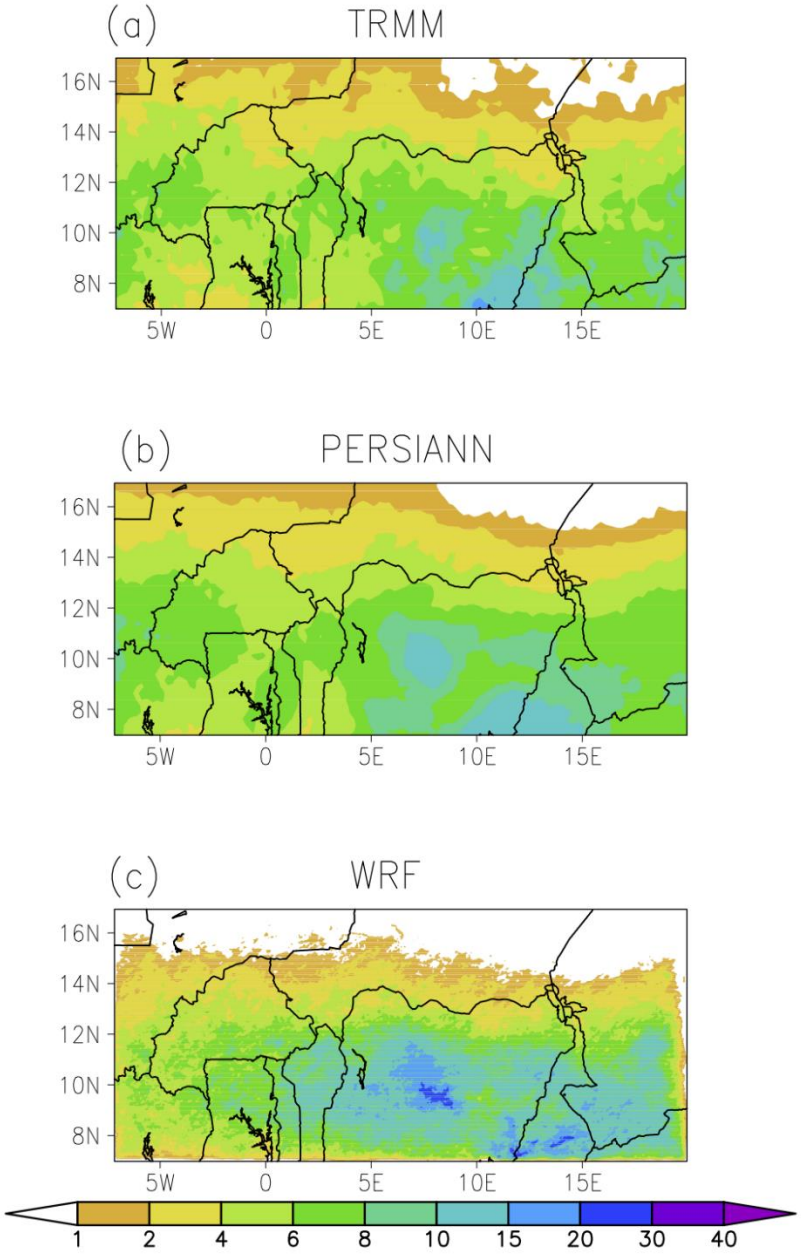

Figure 3.3. JJAS 2006 mean rainfall rate (mm day^{-1}) in (a) TRMM, (b) PERSIANN, and (c) the WRF convection-permitting simulation.

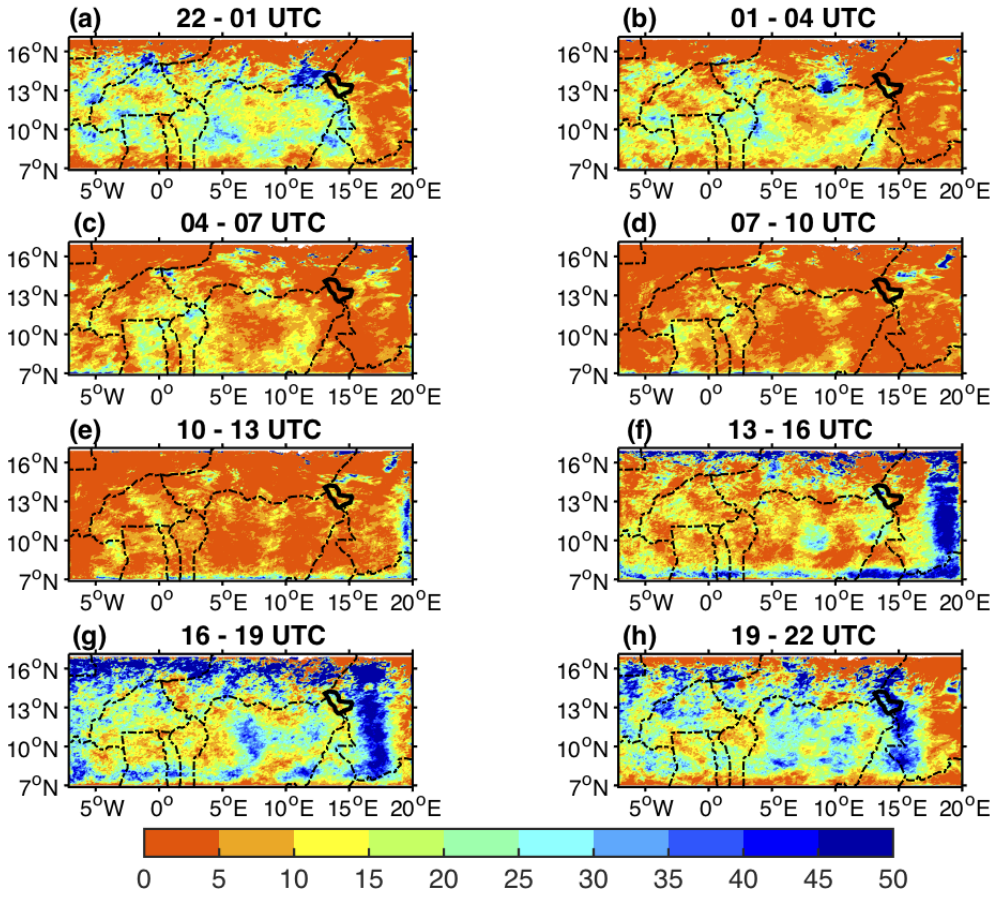

Figure 3.4. Diurnal distribution of rainfall percentage at 3-hourly intervals from JJAS 2006 of the WRF convection-permitting simulation. Dash-dot lines indicate the political boundaries.

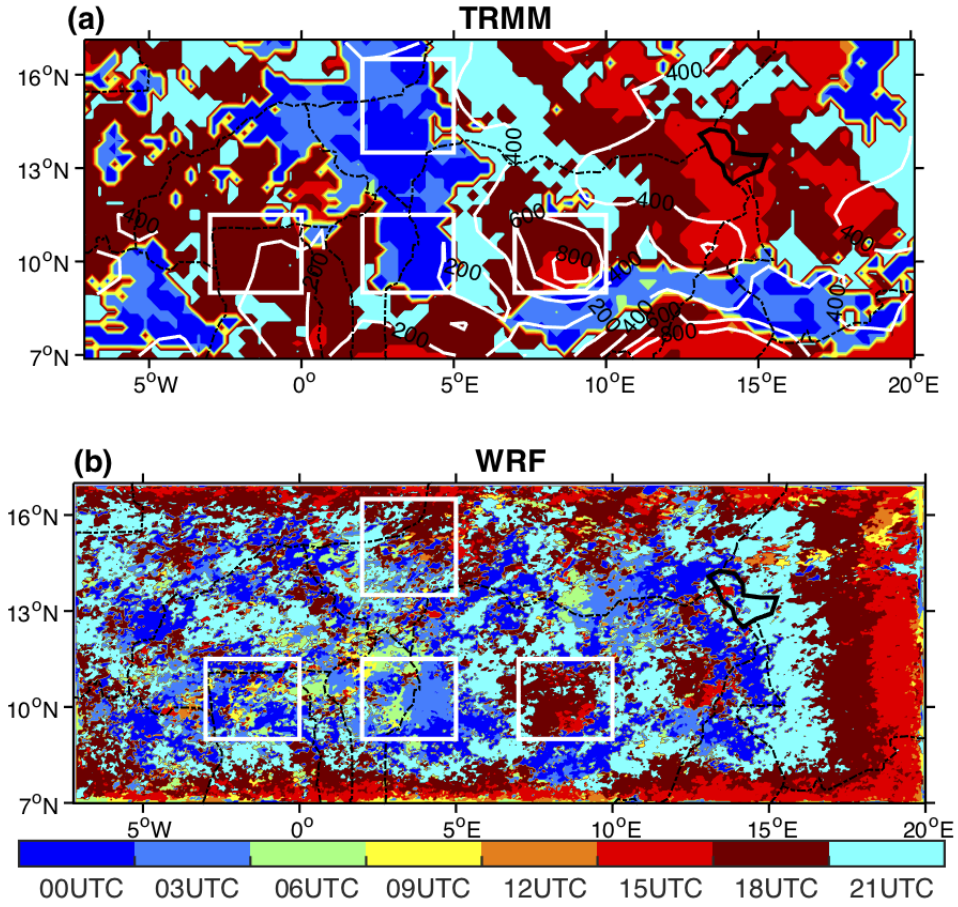

Figure 3.5. Hour of maximum rainfall from JJAS 2006 in (a) TRMM and (b) the WRF convection-permitting simulation. Boxes denote the averaging domains: JP (short for "Jos Plateau", 7°E-10°E, 9°N-11.5°N), AF (short for "afternoon", 3°W-0°W, 9°N-11.5°N) with late afternoon rainfall peaks,; SN (short for "southern nocturnal", 2°E-5°E, 9°N-11.5°N) and NN (short for "northern nocturnal", 2°E-5°E, 13.5°N-16.5°N) with nocturnal rainfall peaks .

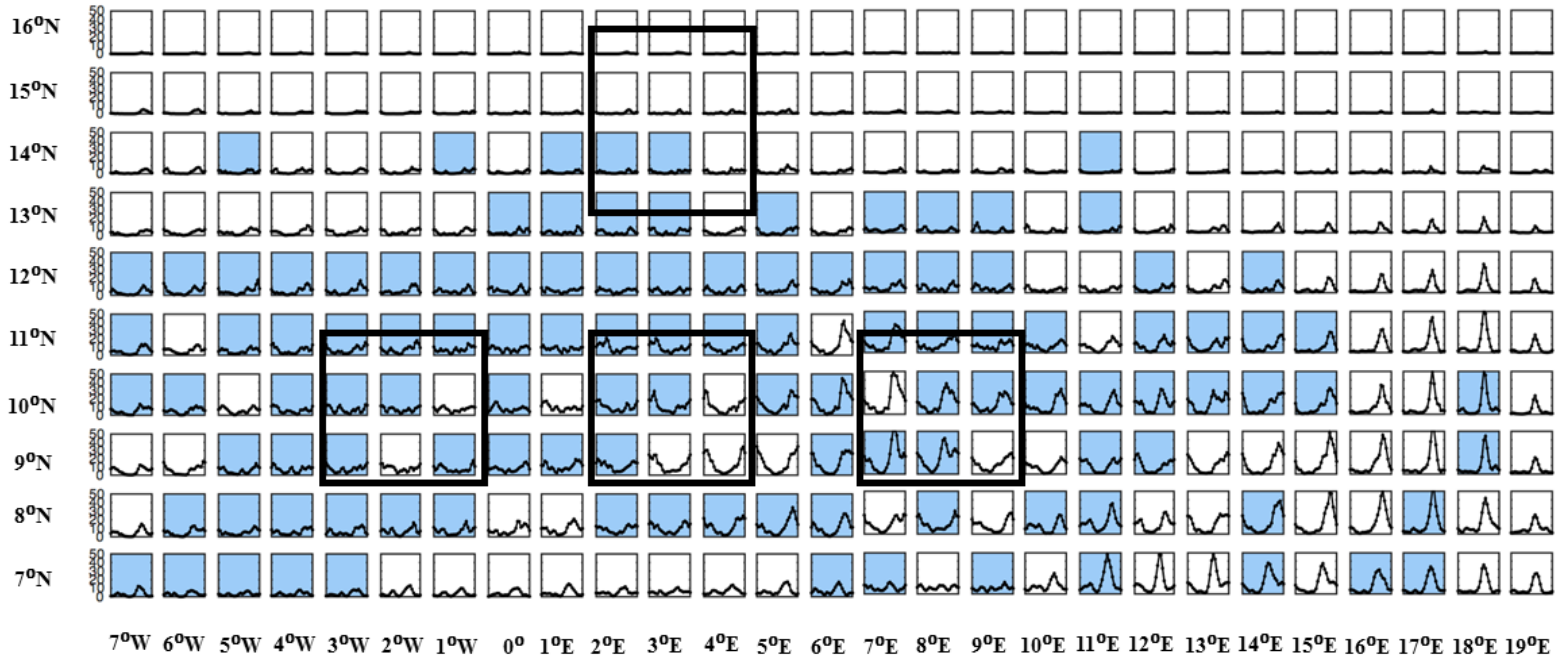

Figure 3.6. Diurnal cycle of WRF simulated JJAS 2006 rainfall (mm day^{-1}) area-averaged for 1°×1° grid boxes within the region of 7°W-21°E, 7°N-17°N. Grid boxes with multiple diurnal peaks of rainfall are shaded in blue. Boxes denote the three domains defined in Figure 5. The x-axis of each panel ranges from 00 UTC to 24 UTC at 1 hour intervals. A peak is defined as at least 1 mm day^{-1} higher than its neighbor times.

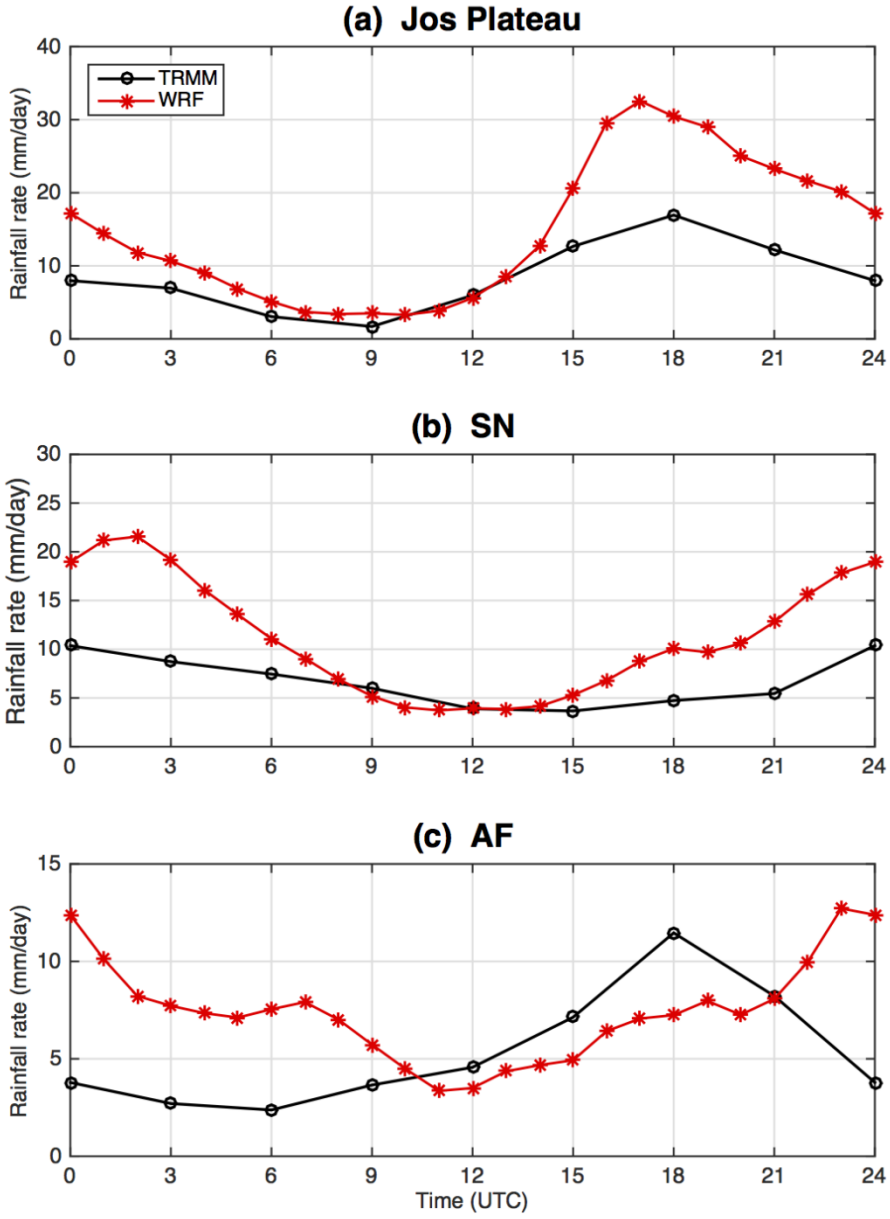

Figure 3.7. JJAS 2006 mean diurnal cycle of rainfall (mm day^{-1}) averaged in (a) Jos Plateau, (b) SN, and (c) AF domains.

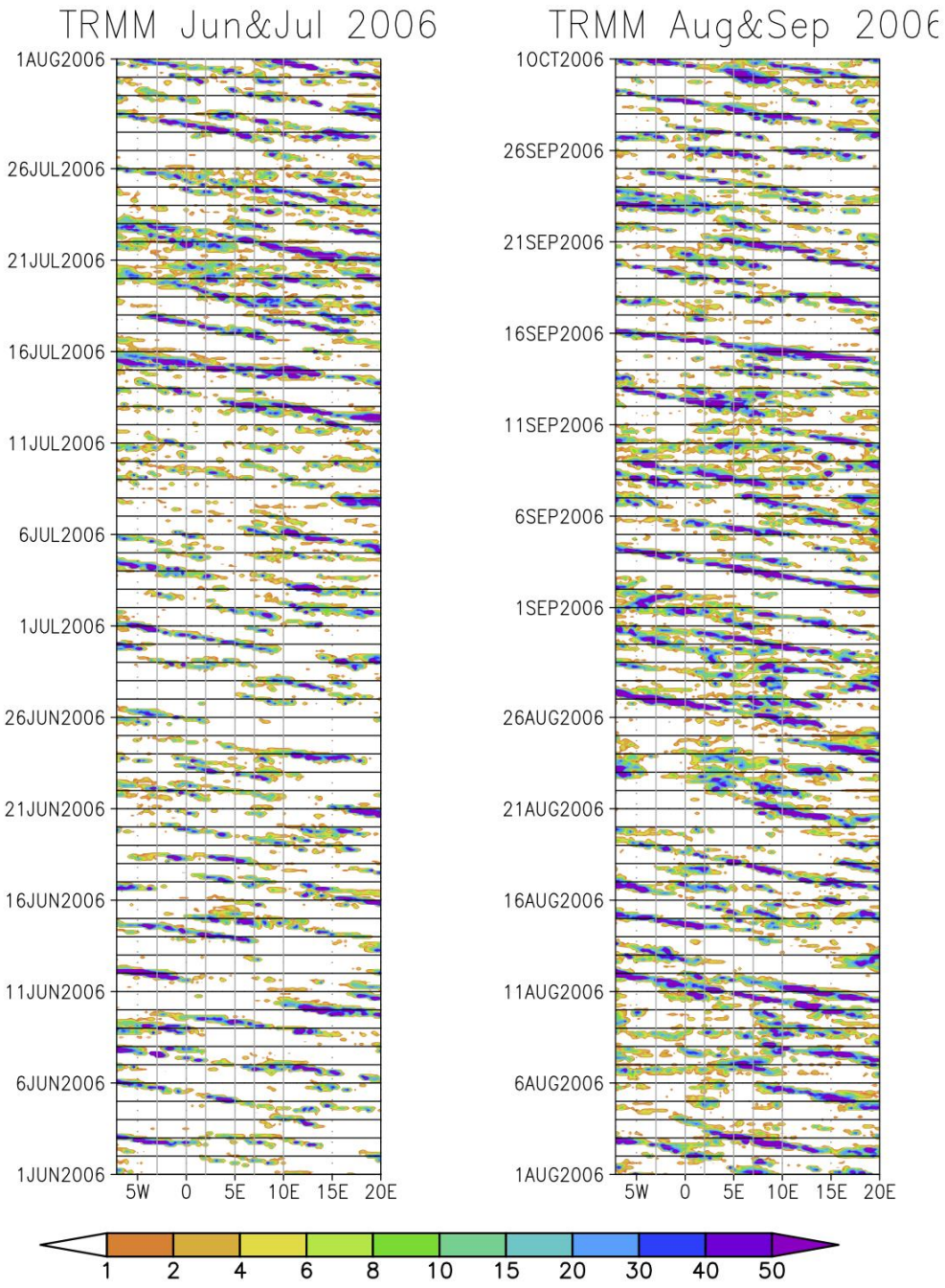
TRMM Jun&Jul 2006
TRMM Aug&Sep 2006
1AUG2006
26JUL2006
21JUL2006
16JUL2006
11JUL2006
6JUL2006
1JUL2006
26JUN2006
21JUN2006
16JUN2006
11JUN2006
6JUN2006
1JUN2006
10CT2006
26SEP2006
21SEP2006
16SEP2006
11SEP2006
6SEP2006
1SEP2006
26AUG2006
21AUG2006
16AUG2006
11AUG2006
6AUG2006
1AUG2006
5W 0 5E 10E 15E 20E
1 2 4 6 8 10 15 20 30 40 50

Figure 3.8.

Figure 3.8. Hovmöller diagram of TRMM 3-hourly rainfall (mm day^{-1}) averaged between 9°N-11.5°N for (a) June and July and (b) August and September of 2006. Grey lines denote the boundaries of the AF (3°W and 0°W), SN (2°E and 5°E), and JP (7°E and 10°E) domains.

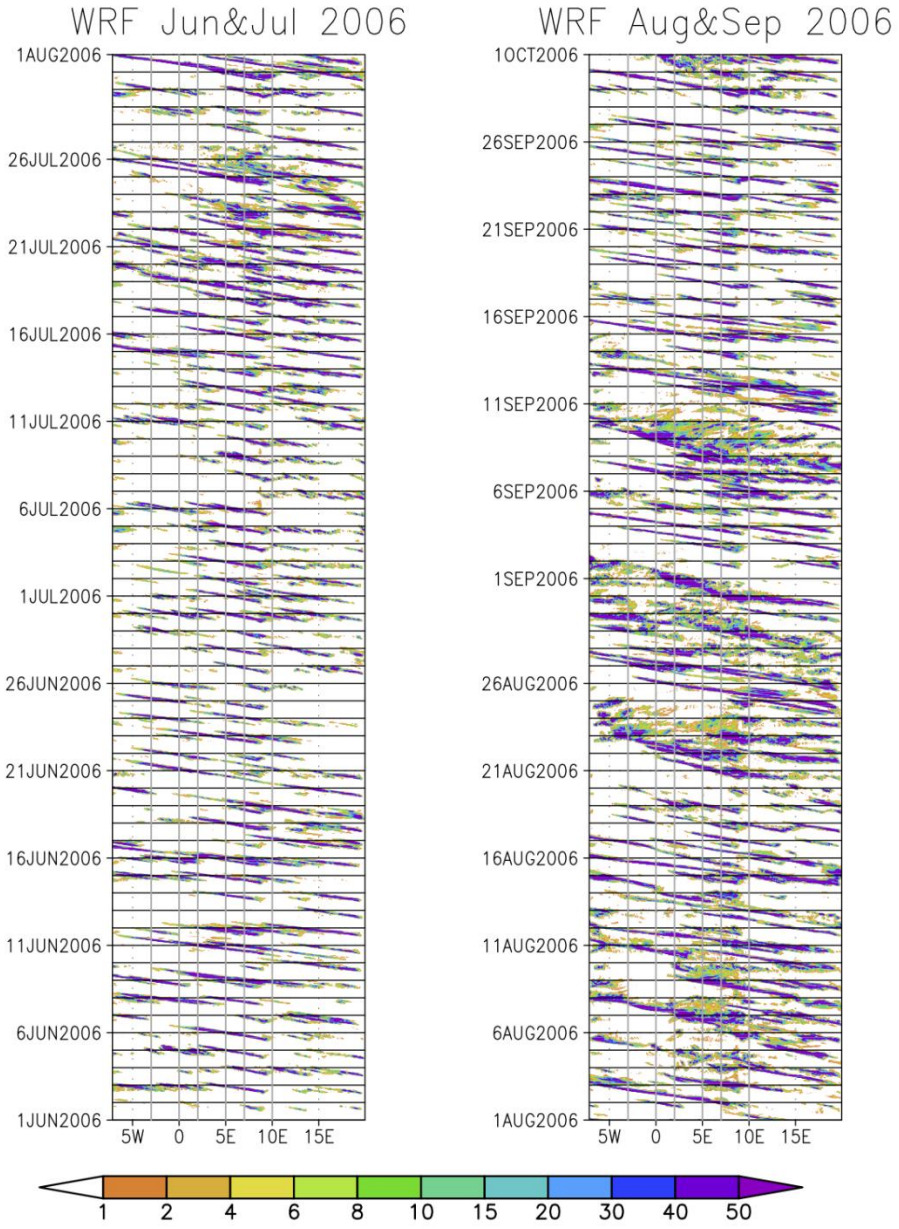

Figure 3.9. Same as Figure 3.8, but for the WRF convection-permitting simulation.

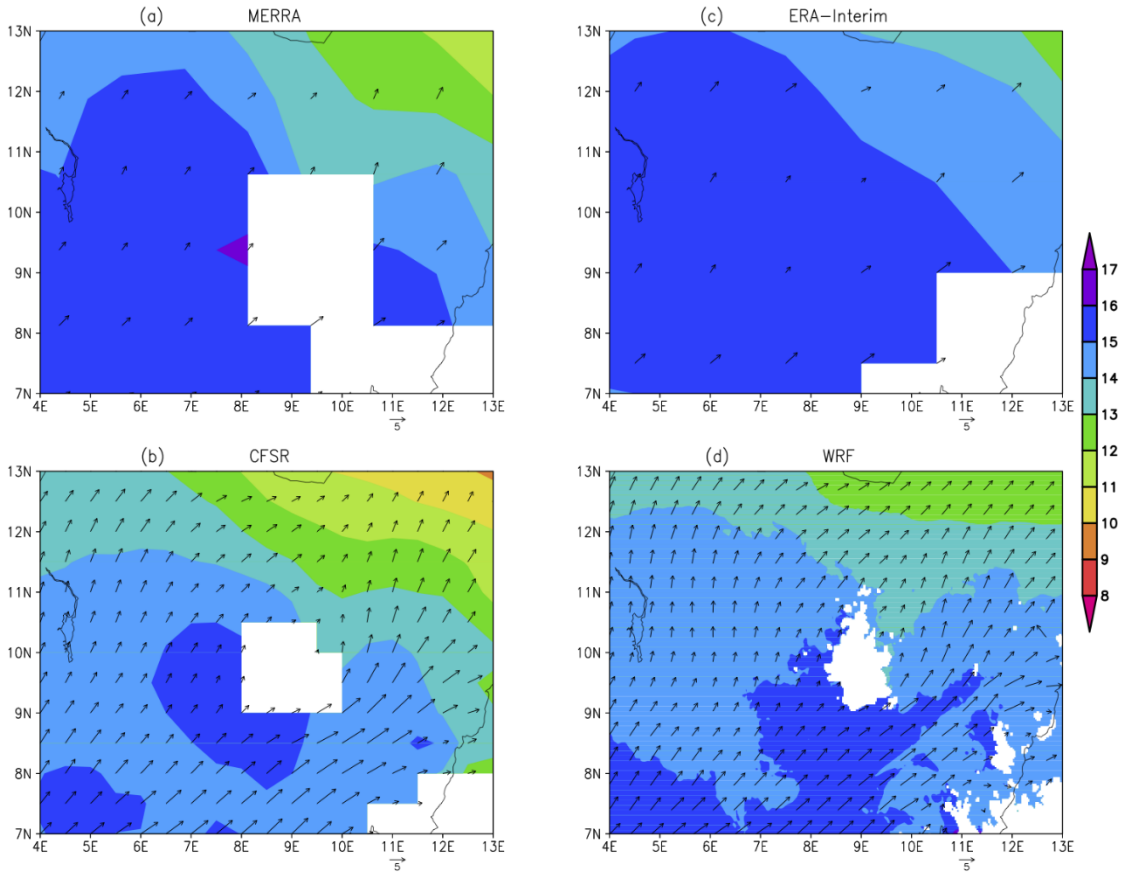

Figure 3.10. Jos Plateau region JJSA 2006 mean 925 hPa specific humidity (shaded, units g kg^{-1}) and wind (vectors, units m s^{-1}) in (a) MERRA, (b) CFSR, (c) ERA-Interim, and (d) the WRF convection-permitting simulation.

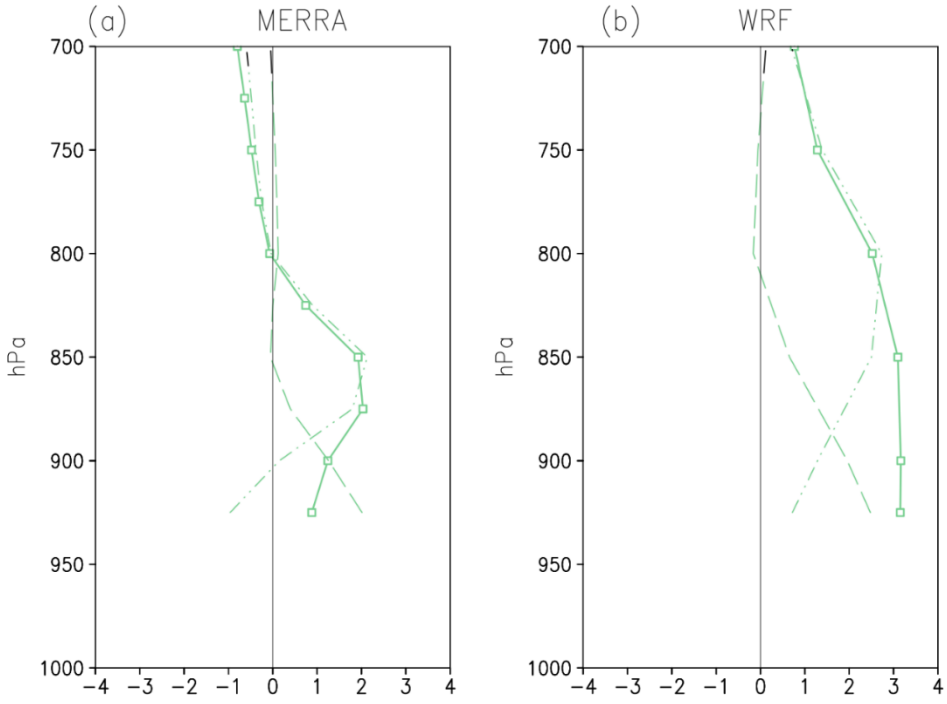

Figure 3.11. (a) Profiles of MERRA total MSE (solid lines; units: 10^3 m^2 s^{-2}), c_pT (dashed lines), and Lq (dot-dashed lines) anomalies at 15 UTC averaged a the domain (8.3°E-8.8°E, 9.5°N-10°N) to the west of the top of Jos Plateau. (b) Is the same as (a) but for the WRF convection. Units are 10^3 m^2 s^{-2}.

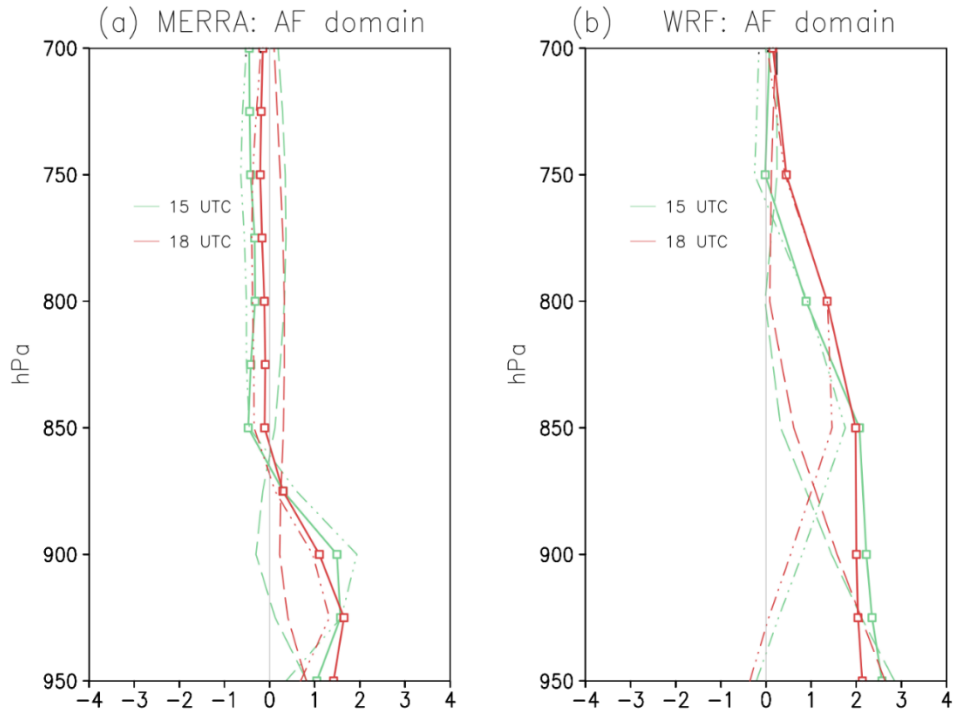

Figure 3.12. (a) Profiles of MERRA total MSE (solid lines; units: 103 m2 s-2), c_pT (dashed lines), and Lq (dot-dashed lines) anomalies averaged over the AF domain at 15 UTC (green) and 18 UTC (red). (b) Same as (a) but for the WRF convection-permitting simulation. Units are 103 m2 s-2.

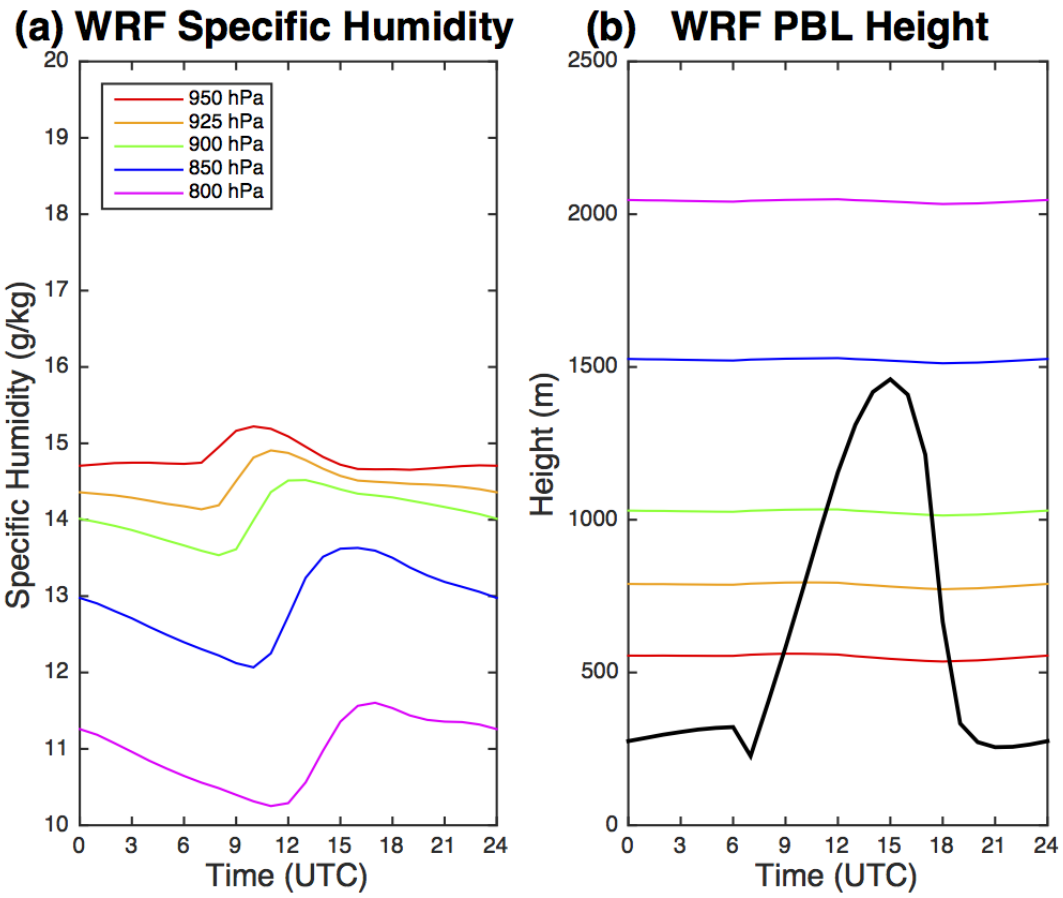

Figure 3.13. JJAS 2006 AF domain mean diurnal cycle of (a) low-level specific humidity (g kg^{-1}) and (b) geopotential height (color lines, units: m) and planetary boundary layer (PBL) height (bold line, units: m) in the WRF convection-permitting simulation.

Chapter 4: West African Monsoon Demise: Climatology, Interannual Variations, and Relationship to Seasonal Rainfall

ABSTRACT

The material from this chapter has been published on the Journal of Geophysical Research-Atmospheres (Zhang and Cook 2014) with Dr. Kerry H. Cook as the second author who supervised this research.

The climatology and interannual variations of the West African monsoon demise are investigated using the Tropical Rainfall Measuring Mission and the Global Precipitation Climatology Project precipitation datasets along with the ERA-Interim reanalysis. During monsoon demise, the rainfall maximum progresses southward from the Sahel to the Gulf of Guinea. The West African monsoon demise is smooth, with no evidence of a meridional jump of the rainfall maximum as occurs during monsoon onset.

The climatological monsoon demise date, defined by using a 2 mm day^{-1} rainfall threshold for the Sahel, is October 20th. The demise date varies up to 25 days during the 1979-2012 period, between October 5th and 30th. An early (late) demise is associated with an anomalously strong (weak) North Atlantic subtropical high, which extends over the Mediterranean and Sahara throughout the demise period.

The monsoon season total rainfall is found to be significantly correlated with the demise date. In a composite of early (late) demise cases, northerly (southerly) moisture flux anomalies, which enhance (reduce) moisture divergence, are associated with an anomalously strong (weak) North Atlantic subtropical high. In addition, the early (late)

demise of the West African monsoon is accompanied by cold (warm) sea surface temperature anomalies in the subtropical North Atlantic.

4.1 INTRODUCTION

The West African monsoon plays an important role in the regional climate and water resources of the Sahel. The monsoon has a significant influence on agricultural management as it brings most of the rainfall to West Africa during the course of a year. Therefore, an improved understanding of the physical processes that control the West African monsoon season is important because it will ultimately improve weather and climate forecasts for this region.

The onset of the Sahel monsoon season occurs typically in late June or early July with an abrupt shift of the rainfall maximum from the Guinean coast (~5°N) to the Sahel (~10°N); this is called the West African monsoon jump (Sultan and Janicot 2003; Hagos and Cook 2007). From late September to October, rainfall over the Sahel decreases gradually. Both the onset and demise dates are critical for agricultural planning. For example, a late onset may lead to late planting, and an early end of the rainy season might cause crop failure. While West African monsoon onset processes have been explored in several studies (Sultan and Janicot 2003; Ramel et al. 2006; Hagos and Cook 2007), less attention has been paid to the demise process.

The purpose of this paper is to better understand the basic dynamics of the West African monsoon demise, and its relationship to seasonal rainfall totals, from the perspectives of the climatology and interannual variations**.** The findings of this paper improve our understanding of the physical processes associated with the West African monsoon demise, and serve as a basis for modeling investigations. In addition, the

physical processes that regulate the monsoon demise provide support for operational weather and climate forecasts of the monsoon demise.

Current literature on the West African monsoon demise is reviewed in the following section. The datasets and methodology used in this paper are described in section 3. Results are presented in section 4, and conclusions are summarized in section 5.

4.2. BACKGROUND

The West African monsoon demise has been examined in several studies which focus more generally on the seasonal cycle of the West African monsoon climatology. The Sahel has a single rainy season, and a smooth monsoon demise in boreal fall. By defining monsoon demise as when daily precipitation consistently drops below its local annual mean, Liebmann et al. (2012) show that the climatological monsoon demise date over the Sahel ranges generally from September to November. Thorncroft et al. (2011) study the annual cycle of the West African monsoon and the associated atmospheric circulations using the Global Precipitation Climatology Project (GPCP) pentad precipitation dataset and the European Centre for Medium-Range Weather Forecasts (ECMWF) ERA-Interim reanalysis. They also find a smooth southward migration of the rainfall maximum from the Sahel to the Guinean coast during the monsoon demise, associated with an African Easterly Jet (AEJ) at 700 hPa located poleward of the rainfall maximum. In addition, they relate the southerly moisture flux of the monsoon flow with the location of the West African continental heat low.

Using radiosonde observations, Zhang et al. (2006) suggest that the southerly monsoon flow diminishes in both strength and depth during monsoon demise, and the

northerly flow over the Sahel at 700 hPa is stronger than at the monsoon peak. Nicholson and Grist (2003) show that, in the climatology, the AEJ weakens and moves southward during the monsoon demise in the National Centers for Environmental Prediction/National Center for Atmospheric Research (NCEP/NCAR) Reanalysis 1.

In addition to these climatological studies, interannual variations of Sahel rainfall are also associated with variations of the AEJ. By compositing wet and dry years for the Sahel, Grist and Nicholson (2001) conclude that the AEJ is stronger (weaker) and southward (northward) displaced during dry (wet) years.

Here we find that the timing of the monsoon demise is related to the eastward extension of the North Atlantic subtropical high (NASH) over the Mediterranean and Sahara throughout the demise period. A brief review of the known relationship between the NASH and the West African monsoon system is presented. Martin and Thorncroft (2013) discuss the impacts of the Atlantic Multidecadal Oscillation (AMO) on the seasonal cycle of the West African monsoon in observations and reanalyses. Their results show that, in both boreal summer (JAS) and fall (OND), warm (cold) North Atlantic SSTAs during the warm (cold) phase of the AMO are associated with negative (positive) anomalies of the NASH, and increased (decreased) rainfall over West Africa (the Sahel for JAS and the Guinean coast for OND). Especially in OND, the extension of the NASH over northern African and the Mediterranean is weaker (stronger) during the warm (cold) phase of the AMO. In a modeling study, Grosfeld et al. (2008) confirm that North Atlantic cold (warm) SSTAs are associated with high (low) sea level pressure on multidecadal timescales. However, these studies do not exclude the impacts of other ocean basins on the NASH.

The NASH can also be involved in the mid-latitude forcing of the West African monsoon. For example, Vizy and Cook (2009, 2013) propose a mechanism in which cold

air surges from the Mediterranean suppress convective activity of the West African monsoon. The strong low-level northerly flow that accompanies cold air surges is influenced by the NASH, which extends over northern Africa and the Mediterranean during the West African monsoon demise.

Several studies indicate that the timing of the West African monsoon demise may change in the future under global warming scenarios. Using climate projections from Coupled Model Inter-comparison Project phase 3 (CMIP3), Biasutti and Sobel (2009) suggest that the Sahel rainy season will be delayed in response to increased greenhouse gases. Both the onset and demise dates of the West African monsoon are shifted later in the year and the rainy season becomes shorter. Biasutti (2013) shows that the more recent CMIP5 coupled GCM simulations produce a similar prediction, i.e., a negative rainfall trend in the onset months (June-July) and positive trend in the demise months (September-October). A series of idealized simulations in this study reveal that this change of the seasonal cycle is caused by nonlinear interactions between the fast response (land–atmosphere system) and slow response (ocean–atmosphere system) to increasing greenhouse gases. Vizy et al. (2013), however, simulate an overall increase in Sahel precipitation, with no change in mid- and late-21st century seasonality. This result is based on well-validated regional climate model projections at 30 km resolution with lateral boundary conditions and sea surface temperatures constrained from present-day reanalysis plus future climate anomalies from CMIP5 projections. Such discrepancies in future projections indicate that the underlying physical processes of the seasonal cycle over West Africa need to be better understood and evaluated to enhance confidence in the projections.

Monsoon demise has also been investigated in other monsoon regions. For example, Wang and LinHo (2002) find that the Asian monsoon retreat is southward over

India and the western North Pacific, similar to West Africa, but over East Asia it progresses northward. In a detailed study of the Indian monsoon demise, Syroka and Toumi (2004) find that the interannual variability of the monsoon demise is larger than that of the onset, and that the demise date is the dominant factor in determining variability of the total rainfall. They suggest that the Indian monsoon demise is associated with a dry phase of the intraseasonal oscillation, and that an early (late) demise is associated with El Niño (La Niña) events on interannual timescales. Defining the Indian monsoon demise through vertically-integrated moisture fluxes, Fasullo and Webster (2003) also find a strong correlation between the monsoon demise date and the JJAS all-India rainfall.

Arias et al. (2012) study decadal variations of the North American monsoon seasonality and identify two dry periods on multidecadal timescales characterized by late onset, early demise, and weaker rainfall rates. Their statistical analysis shows that the 1949-1970 dry period is attributable to the positive phase of the AMO, while the 1991-2005 dry period with a more persistent early monsoon demise is associated with a combination of the AMO, the global warming trend, and an expansion of the NASH. For the South American monsoon, Zhou and Lau (1998) suggest that the monsoon demise, which manifests as a northeastward retreat of the rainfall maximum, is associated with a weakening of the low-level northwesterly monsoon flow and a double maximum in the upper tropospheric westerly jet. Raia and Cavalcanti (2008) show that the South American monsoon demise is associated with a westward displacement of the South Atlantic subtropical high toward the South American continent.

4.3. DATA AND METHODOLOGY

Two observational datasets of precipitation are used to characterize the seasonal evolution of the West African monsoon demise. The first is the 3-hourly Tropical Rainfall Measuring Mission (TRMM) precipitation product (3B42V7, *Huffman et al.* 2007) from 1998 to 2012. It covers latitudes from 50°S to 50°N with 0.25° latitude by 0.25° longitude horizontal resolution. The advantage of TRMM is that it provides fine-scale resolution for examining the geographical coherence of the monsoon demise over the Sahel. The second dataset is the 5-day GPCP precipitation analysis (2.5° latitude by 2.5° longitude) which is available from 1979 to 2012 (Xie et al. 2003). Although the monthly mean GPCP precipitation dataset (1979-2012) is longer than TRMM, it is not used here because the monthly timescale is inadequate for depicting the monsoon demise.

The ECMWF ERA-Interim reanalysis (ERAI; *Dee et al.* 2011) is used to analyze the atmospheric circulation associated with the West African monsoon demise. It is a global dataset available from 1979 to 2012, with 6-hourly frequency, 1.5° latitude by 1.5° longitude horizontal resolution and 37 vertical levels from the surface to 1 hPa.

Various thresholds have been proposed to define West African monsoon onset and/or demise (e.g., *Marteau et al.* 2009; *Liebmann et al.* 2012). Here we use a uniform threshold because it facilitates relating rainfall to the atmospheric circulation directly. Synoptic variations in the rainfall time series are removed by using a 15-day running average. Then, the demise date of each grid point is defined as the calendar date when the smoothed rainfall falls below the selected threshold without any recovery later in that year. Both of the TRMM and GPCP climatologies are used to explore the spatial distribution of the monsoon demise. Several choices of the threshold value are tested in section 4a before choosing 2 mm/day as the threshold.

The 5-day pentad GPCP precipitation dataset is used to characterize interannual variations because it has a better balance between data record length and frequency for this study. The TRMM dataset is only used to check the consistency for the years in common with the GPCP data. The averaging region is defined as 20ºW-22.5ºE, 7.5ºN-17.5ºN, which is named as "Sahel" for convenience of discussion. First, a climatological demise date for the Sahel precipitation climatology is defined by applying the 2 mm day^{-1} threshold to the area-averaged time series. Then, for each year, the demise date is found by applying the same threshold to the area-averaged Sahel rainfall.

Sensitivity tests show that the calculated demise date anomalies are sensitive to the latitudinal choice due to the strong meridional gradient of rainfall. Here we use 7.5ºN-17.5ºN to include a large number of grid points in the GPCP (4 grids in meridional direction) for robustness, and to capture the full latitudinal extent of the summer monsoon rainfall. We also test the robustness of the results by using different definitions of monsoon demise. Latitudinal variations of the Sahel averaging region are tested. In each test, we first calculate the spatial average, and then define the demise date when 95% of the GPCP climatological annual precipitation has fallen. The rainfall rate on the demise date is used as the threshold to define monsoon demise for each year. In addition, longitudinal variations are tested by separating the Sahel averaging box into two halves: (20ºW-0, 7.5ºN-17.5ºN) and (0-22.5ºE, 7.5ºN-17.5ºN), with the 2 mm/day threshold for defining the demise date). Although the demise date changes in these sensitivity tests, the conclusions about the physical processes remain the same. In this paper, we use the definition of monsoon demise using a 2 mm day^{-1} threshold and the Sahel averaging region (20ºW-22.5ºE, 7.5ºN-17.5ºN). To show the sensitivity, an additional example is presented using 95% percentage definition of demise date as mentioned above and the

southern half region (20ºW-22.5ºE, 7.5ºN-12.5ºN) where rainfall is heaviest during the monsoon demise.

Composite analysis is used to address the interannual variations of the West African monsoon demise. Each year is classified as an early, normal or late demise year by comparing its demise date with the climatological demise date. Differences between the early and late demise composites are analyzed to identify the physical processes responsible for interannual variations. Note that the demise dates for the climatology and each individual year depend on the choice of the uniform threshold, so the composites, especially for normal years, are sensitive to the threshold to some extent.

The moisture budget is used to connect rainfall and circulation anomalies. The vertically- integrated atmospheric moisture budget is

$$P = M + E + R = C + A + E + R, \tag{4.1}$$

where precipitation (P) is the sum of the vertically-integrated moisture convergence (M), evapotranspiration (E), and the residual (R) which includes topographic effects and numerical and sampling errors. M can be further divided into contributions from moisture convergence (C) and moisture advection (A) terms so that

$$M = -\frac{1}{g\rho_w}\int_{p_s}^{p_{top}}\left[\nabla_h \bullet \left(q\vec{v}\right)\right]dp = C + A, \tag{4.2}$$

$$C = -\frac{1}{g\rho_w}\int_{p_s}^{p_{top}}\left[q\nabla_h \bullet \vec{v}\right]dp, \tag{4.3}$$

and

$$A = -\frac{1}{g\rho_w}\int_{p_s}^{p_{top}}\left[\vec{v} \bullet \nabla_h q\right]dp, \tag{4.4}$$

where g is gravitational acceleration, ρ_w is the density of water, p is pressure, p_s and p_{top} are the pressure at the surface and the top of the atmosphere, respectively, q is the

specific humidity, and $\vec{v}$ is the horizontal wind vector. C and A can be further decomposed into zonal and meridional components denoted C_x, C_y, A_x, and A_y.

4.4. RESULTS

4.4.1. Climatology of the West African monsoon demise

Figures 1a and b display Hovmöller diagrams of the rainfall climatology averaged over the Sahel (20ºW-22.5ºE) from the TRMM and GPCP climatologies, respectively. The datasets show a similar seasonal progression of the West African monsoon, which validates the shorter TRMM climatology. The West African monsoon, measured as the rainfall rate over the Sahel, is maximum in August (Figure 1a), when the rainfall at 10ºN reaches about 10 mm day^{-1} and the 0.5 mm day^{-1} isoline reaches 20ºN. Starting in early September, the rainfall maximum weakens and progresses southward. As mentioned above, the monsoon demise is relatively smooth.

The position of the precipitation maximum is closely related to surface temperature and low-level wind. Figures 2a and b display the ERA-Interim climatology of surface skin temperature and 925 hPa meridional wind, respectively. As shown in Figure 2a, the warm Sahara and cold Gulf of Guinea during the summer maintain the thermal contrast that drives the West African monsoon. The Saharan heat low is important in maintaining the southwesterly monsoon flow. Therefore, the low-level meridional wind remains southerly during September and October (Figure 2b), while it decreases in association with the reduction in thermal contrast. After October, the land-sea thermal contrast reverses when the Sahara cools and Atlantic cold tongue declines (Figure 2a). The summer monsoon is entirely shutdown, with low rainfall rates and prevailing northerly wind over the Sahel by the end of October (Figure 2b).

Figures 3a-d show maps of the TRMM climatological monsoon demise date over the Sahel using 1 mm day^{-1}, 2 mm day^{-1}, 3 mm day^{-1}, 4 mm day^{-1} thresholds, respectively. Figures 3e-h display the climatological demise date maps for the GPCP climatology. The large-scale distribution in GPCP is similar to that in TRMM, suggesting a consistency between these two datasets. Overall, the climatological demise date over the Sahel ranges from early September to late November. An early (late) demise over the northern (southern) Sahel corresponds to an advanced (delayed) southward progression of the rainfall maximum during the boreal fall. The zonal distribution of the climatological demise date is generally uniform over the central and eastern Sahel, while the western coastal Sahel has a later demise in association with higher rainfall rates in this region.

The TRMM climatological demise dates along 15ºN and 10ºN are used below to represent the northern and southern Sahel, respectively. Using a 1 mm day^{-1} threshold (Figure 3a), the demise date along 15ºN varies from mid-September in the eastern Sahel to mid-October in the western Sahel. Along 10ºN, the demise date ranges from late October in the eastern Sahel to mid-November in the western Sahel. With a 2 mm day^{-1} threshold (Figure 3b), the demise date distribution is similar but generally about 10 days earlier than with a 1 mm day^{-1} threshold (Figure 3a). With a 3 mm day^{-1} threshold (Figure 3c), the demise date along 15ºN occurs before September 1st (shown as blank) over the central and eastern Sahel, and is in late October along 10ºN. The 4 mm day^{-1} map (Figure 3d) displays the earliest demise date distribution among the four maps.

These demise date maps are used to choose a uniform threshold for further analysis of interannual variations of the monsoon demise. Values of 3 and 4 mm day^{-1} are too high because they do not represent monsoon demise over the northern Sahel. The rainfall time series of an individual year may have large synoptic variations, which may

lead to unrealistic demise dates if 1 mm d^{-1} is used as the threshold. Therefore, we choose 2 mm day^{-1} to characterize the date of the monsoon demise.

Using the 2 mm day^{-1} threshold, the climatological demise date in GPCP is found to be October 20th. The date indicates the third day of a pentad, e.g., October 20th represents the pentad of October 18th -22nd. Therefore, it is not possible to pinpoint an exact day that is the actually climatological demise day in GPCP. The climatological demise date in TRMM is as same as in GPCP.

Figures 4a and b show the low-level circulation for August and October from the ERAI reanalysis climatology, respectively. Seasonal variations in the NASH (Davis et al. 1997) are apparent. In boreal summer (e.g., August), the NASH reaches its peak strength and is mainly confined over the North Atlantic basin, while the heat low covers much of the Sahara. During the monsoon demise season (e.g., October), the NASH becomes weaker, and extends eastward over northern Africa and the Mediterranean. Note that the heat low is centered on the equator at the time of the monsoon demise.

4.4.2. Interannual variations of the West African monsoon demise

Interannual variations of the West African monsoon demise and the associated atmospheric circulation are discussed in this section. Figure 5a displays the demise date anomaly (against the climatological date of October 20th) for the 1979-2012 period using the 2 mm day^{-1} threshold. In GPCP (bars in Figure 5a), the earliest monsoon demise is on October 5th and the latest monsoon demise date is October 30th. The demise dates in TRMM (stars in Figure 5a) are generally consistent with the GPCP dates during the common years of 1998-2012.

All 34 years of the 1979-2012 period are classified into early/normal/late monsoon demise composites according to positive/zero/negative anomaly of the GPCP demise date as shown in Figure 5. The numbers of years in the early, normal and late monsoon demise composites are 14, 9, and 11, respectively.

Two periods are defined for further analysis. Period 1 is from October 5th to 20th, during which the rainfall in the early demise composite falls below 2 mm day^{-1} while the rainfall in the late demise composite remains above 2 mm day^{-1}. Period 2 is from October 20th to 30th, during which the rainfall in the late demise composite drops below 2 mm day^{-1}. Separating these two periods can help explore the persistence of the physical processes controlling the monsoon demise.

Figure 5b is same as Figure 5a but using a 95% percentage definition of demise date and the southern half of the Sahel averaging region (20ºW-22.5ºE, 7.5ºN-12.5ºN). The demise threshold is 3.5 mm day^{-1} and the climatological demise date is October 15th. The demise date anomalies shown in Figure 5b are different from those in Figure 5a, indicating that the classification of early/normal/late composite is sensitive to the monsoon demise definition.

Next we will examine interannual variations of atmospheric circulation associated with the monsoon demise. Figures 6a-c display the 925 hPa geopotential height and wind anomalies in the early, normal and late demise composites, respectively, during Period 1. In the early demise composite (Figure 6a), a prominent anomalous high center occurs over the Mediterranean and the adjacent land, including southern Europe and the Sahara. Accompanying this positive anomaly is an anticyclonic wind anomaly, which is manifested as strong northerly/northeasterly wind anomalies over the northern Sahel. The southerly monsoon flow to the south of the Sahel has relatively small anomalies.

In the normal demise composite (Figure 6b), only weak negative geopotential height anomalies are shown over West Africa and adjacent oceans. In the late demise composite (Figure 6c), there are strong negative geopotential height anomalies over southern Europe, the Mediterranean and the Sahara, which is opposite to the early demise composite (Figure 6a). Pronounced southerly wind anomalies are found to the north of the Sahel, part of the anomalous cyclonic flow associated with the low anomalies. In addition, there is no evident southerly flow anomaly along the southern boundary of the Sahel.

The composites for Period 2 are shown in Figures 6d-f. In the early demise composite (Figure 6d), positive geopotential height anomalies remain over the Mediterranean and Sahara, while the center shifts northward to Europe. Similar to Period 1, strong northerly/northeasterly wind anomalies occur over the northern Sahel. The normal demise composite (Figure 6e) features positive geopotential height anomalies over the subtropical North Atlantic and Mediterranean, which is different from Period 1 (Figure 6b). In the late demise composite (Figure 6f), in contrast to the early demise composite (Figure. 6d), the subtropical high over the Mediterranean and Sahara has negative anomalies, associated with southerly/southwesterly wind anomalies over the northern Sahel.

The subtropical high anomalies at 925 hPa are also present at other levels in the lower troposphere (below 500 hPa; not shown). We conclude that, in both Periods 1 and 2, an early (late) demise of the West African monsoon is associated with an anomalously strong (weak) subtropical high over the North Atlantic and Sahara.

Figure 7 is the same as Figure 6 but using the composites according to Figure 5b. The above conclusions concerning the role of the subtropical high are valid for this sensitivity test and other sensitivity tests using different averaging latitudes (not shown).

Note that, as suggested by Figures 6 and 7, the heat low is not an important factor in the dynamics of the monsoon demise because the associated low-level geopotential height anomalies are relatively small and very few of the wind vector anomalies over this region are significant at the 95% confidence interval. In the following, only the analysis using the 2 mm day^{-1} threshold to define the demise date is presented because the physical processes are the same.

The AEJ is stronger in the early demise composite over the western Sahel, weaker in the late demise composite, and has no obvious anomaly in the normal demise composite, during Period 1 (not shown). This is consistent with the observations that a dry (wet) monsoon season is associated with a stronger (weaker) AEJ (Grist and Nicholson 2001).

During Period 2, a similar conclusion is valid to the south of the Sahel (near the equator). However, no obvious difference occurs over the Sahel. It is not possible to distinguish causality between the AEJ and the monsoon demise because the generation of the AEJ is related to the meridional soil moisture gradient between the Sahara and tropical Africa, which is tightly coupled with precipitation (Cook 1999).

4.4.3. Relationship between the West African monsoon demise and rainfall

Figure 8 shows the seasonal cycle of the area-averaged Sahel rainfall (15-day running averaged) in the GPCP climatology, the early demise composite and the late demise composite. Large differences can be seen in October between the early and late demise composites, which distinguish them from the climatology. Comparing the early and late demise composites in other periods of the monsoon season, there is no prominent difference in the developing phase (June and July) but there is a large difference in

August, which is the peak month of the West African monsoon. Differences in the timing of monsoon demise may be linked to differences during the monsoon peak through a positive feedback mechanism at the seasonal time-scale. For example, West Africa is identified as a hotspot of strong land-atmosphere coupling (Koster et al. 2006), which might support a positive soil moisture-rainfall feedback on seasonal timescales. However, the rainfall differences in September are smaller than in August, which is not in good agreement with the positive feedback hypothesis. While testing such a hypothesis is beyond the scope of this paper, it suggests that the monsoon demise cannot be fully attributable to the strength of the monsoon peak through a positive feedback.

We use the same 2 mm day^{-1} threshold to define the West African monsoon onset. The rainfall accumulated between onset and demise dates is defined as monsoon season total rainfall. It is clear from Figure 8 that the early demise composite has less monsoon season total rainfall than the late composite. This is also evident in Figure 5. Note that 8 out of 14 early demise years are in the 1980s which is known as part of the "Sahel drought" period, while 5 out of 11 late demise years are in 1990s which is the "recovery" period of the decadal drought (Hagos and Cook 2008).

Correlations among the monsoon season total rainfall and demise date are displayed in Table 1. The GPCP monsoon season rainfall and the GPCP demise date are significantly correlated (correlation coefficient is 0.56 and *p*-value is 0.0006). The correlation of these two variables is not significant in the TRMM 1998-2012 time series because the data record is not long enough. Even using GPCP, seasonal rainfall and demise date are also not significantly correlated if only 1998-2012 (the common period with TRMM) is used.

Figure 9 compares the demise date and seasonal rainfall anomalies year by year in both GPCP and TRMM. The high correlations, shown in Table 2, suggest good agreement between GPCP and TRMM for the monsoon demise date and total rainfall.

An atmospheric moisture budget analysis is conducted to explore connections between the monsoon demise and circulation anomalies, especially the NASH variations and extensions over the Sahara. Figure 10a shows the GPCP rainfall climatology during Period 1. The rainfall is concentrated over 7.5-12.5°N. Figure 10b displays the climatology of the vertically-integrated moisture flux and convergence during Period 1. Moisture divergence covers most of the Sahel except over the southern boundary, suggesting that evapotranspiration during this period is higher than the rainfall. The prevailing moisture flux vectors are easterly/northeasterly, transporting moisture to the North Atlantic and the Gulf of Guinea. The Atlantic Inter-tropical Convergence Zone (ITCZ) is centered at about 7°N, as indicated by the moisture flux convergence.

Figure 10c shows the rainfall anomalies during Period 1 for the early demise composite and Figure 10d displays the vertically-integrated moisture flux and convergence anomalies. The rainfall anomalies are larger than 0.5 mm day^{-1} over the southern Sahel. The moisture convergence in Figure 10d is comparable to these rainfall anomalies, indicating that the rainfall anomalies are mainly supported by the vertically-integrated moisture flux convergence. The northerly moisture flux anomalies over the southern Sahel, which enhance moisture divergence, are associated with the northerly wind anomalies in the lower troposphere due to the strengthening of the NASH. Figure 10e,f show the late demise composite anomalies of rainfall and vertically-integrated moisture flux and convergence, respectively. Rainfall anomalies larger than 1 mm day^{-1} are found over the western Sahel (Figure 10e), which is also mainly associated with vertically-integrated moisture flux convergence (Figure 10f). The southerly/southwesterly

moisture fluxes in Figure 10f reduce the moisture divergence compared with the climatology in Figure 10b. The southerly moisture flux anomalies are associated with southerly wind anomalies as a consequence of the weakening of the NASH.

Figures 11a-f are the same as Figs. 10a-f but for Period 2. With monsoon demise, the southern Sahel rainfall climatology (Fig 11a) falls below 2 mm day^{-1} (by our definition of demise). Similar to Period 1, the divergence of the vertically-integrated moisture flux is dominant over the Sahel. The Atlantic ITCZ is shifted slightly southward compared with Period 1. Since the NASH anomalies in Period 1 persist during this time, Figures 10c-f lead to the same conclusions as those for Period 1.

The vertical profiles of individual moisture flux convergence terms are analyzed in cross sections at 10.5°N shown in Figure 12, where the rainfall anomalies are relatively strong. The zonal convergence and advection terms are omitted because there is no spatial coherence. The differences above 500 hPa are negligible because the specific humidity is very low.

Figure 12a shows the difference of meridional convergence term (C_y) between the early and late demise composites (early minus late) in Period 1. The full field of C_y in the early composite is shown in Figure 12e. There is a shift in meridional convergence from low-levels (surface to about 850 hPa) to mid-levels (about 850 hPa to 500 hPa). The low-level southerly monsoon flow exhibits no evident change between the early and late demise composites (Fig 6). However, in the early demise composite, northerly wind anomalies enhance meridional convergence. The opposite applies for the late demise case. Therefore, the differences in the low-levels are positive, indicating stronger wind convergence in the early demise composite. However, in mid-levels, there is no monsoon flow to converge with the northerly wind. The northerly wind anomalies in the early demise composite are associated with stronger wind divergence and the opposite occurs

in the late demise composite. Thus, negative differences for the meridional convergence term are exhibited at these levels.

Figure 12b displays the meridional moisture advection (A_y) differences between the early and late demise composites (early minus late) and Figure 12f shows the full field in early composite. The meridional gradient of atmospheric specific humidity is negative in this region, with drier air to the north. Negative anomalies dominate from the surface to 500 hPa except at low levels near 0ºE. This suggests that more dry air is advected southward through this cross section in the early demise case than in the later demise case. These differences are related to the presence of stronger (weaker) northerly winds in the early (late) demise composite, in association with the NASH anomalies.

Meridional convergence and advection differences are shown in Figure 12c and 12d, respectively, for Period 2. The anomalous structures are similar to those in Period 1, except the largest anomalies are closer to the surface.

In summary, when there is an early demise in the monsoon rainfall in the Sahel, the NASH is anomalously strong and accompanied by anomalous mid-level moisture divergence and low-level moisture convergence. Also present are negative meridional moisture advection (A_y) anomalies over the southern Sahel. The opposite applies for the late monsoon demise case.

When an anomalously strong NASH is positioned over the Sahara and the Mediterranean region, the resulting northerly wind anomalies favor the formation of synoptic-scale cold air surges which transport relatively cold and dry air from the Mediterranean and Sahara to the Sahel (Vizy and Cook 2009, 2013). These cold air surges tend to stabilize the atmospheric profile over the Sahel and, while this paper does not analyze cold air surges, we note that this is a mechanism that provides a linkage between the NASH and the Sahel rainfall anomalies on synoptic time scales. In addition,

on seasonal timescales, Vizy and Cook (2013) show that the reduced rainfall in the Sahel and tropical Africa is associated with eastern Saharan low-level colder conditions.

4.4.4. Linkages between the West African monsoon demise and large-scale SSTs

We have demonstrated that interannual variations of the West African monsoon demise are associated with interannual variations of the NASH. Here we investigate the linkages between the NASH and the underlying North Atlantic sea surface temperatures (SSTs). Figures 13a-c show the Period 1 anomalies of sea surface temperature from the ERA-Interim reanalysis for the early, normal and late demise composites, respectively. To isolate natural North Atlantic SST variations from the global warming trend in recent decades, we subtract global mean SSTs averaged between 60°S and 60°N at each time step (Trenberth and Shea 2006). The resulting time series is used to calculate the SSTAs. For Period 1, the removed global SST values in the early composite are about 0.1 K colder than in the late demise composite.

Cold SSTAs, up to 0.3 K in the tropical and subtropical North Atlantic, are associated with the stronger NASH of the early demise composite during Period 1 (Figure 13a). Warm SSTAs are located to the south of the equator. For the late demise composite, there are warm SSTAs in the subtropical and western tropical North Atlantic, and cold SSTAs in the eastern tropical Atlantic along the West African coast and Gulf of Guinea (Figure 13c).

Similar SSTA patterns persist through Period 2 as shown in Figures 13d-f. We conclude that in both Period 1 and 2, the anomalously strong (weak) NASH is associated with cold (warm) SSTAs in the underlying subtropical North Atlantic.

This association can be explained by local thermodynamics, i.e., cold (warm) SSTs correspond to a high (low) sea-level pressure, which is revealed in some observational (Martin and Thorncroft 2013) and modeling (Grosfeld et al. 2008) studies. Here we are not excluding the impacts of remote SSTs on the NASH. Globally, the subtropical highs are related to the descending branch of the Hadley cell from the perspective of the global zonal mean circulation. Therefore, some remote tropical SSTs could be linked to the NASH through teleconnections. In addition, NASH is also influenced by monsoonal heating over land and local air-sea interactions (Rodwell and Hoskins 2001; Seager et al. 2003). Further analysis is needed to isolate the role of SSTs in different ocean basins in influencing the demise of the West African monsoon. For example, the ENSO signals in the east and central Pacific shown in Figure 13 counteract the conclusion of previous studies (e.g. *Janicot et al.* 1996; *Rowell* 2001) that El Niño is associated with lower rainfall amount in the Sahel.

Although the early (late) demise composite indicates that there are warm (cold) SSTAs in the southwest corner of the Sahel averaging region, the Sahel rainfall is not sensitive to them because no significant low-level geopotential height anomalies corresponding to these SSTAs occur (Figures 6 and 7). The offshore (onshore) wind anomalies in the early (late) demise composite have a much larger spatial scale than these SSTAs, indicating that the wind anomalies are determined by processes operating on a much larger spatial scale, i.e. the NASH.

4.5. CONCLUSIONS

The observed climatology and interannual variations of the West African monsoon demise are examined using TRMM 1998-2012 daily data and GPCP 1979-2012

5-day pentad data. The atmospheric circulations and large-scale SSTAs associated with interannual variations of the monsoon demise are analyzed in the ERA-Interim reanalysis.

In the climatology, the demise of the West African monsoon occurs from September to early November as the rainfall maximum progresses southward from the Sahel to the Gulf of Guinea. The southerly monsoon flow into the Sahel (8ºN) decreases from more than 2 m s^{-1} in early September to less than 1 m s^{-1} in late October. Distinct from the abrupt onset, the monsoon demise is smooth with no evident meridional jump of the rainfall maximum. Applying uniform thresholds to indicate monsoon demise, the demise date is zonally uniform over the central and eastern Sahel, while the western Sahel has a later demise. Using a 2 mm day^{-1} threshold, the demise date varies from early September over the northern Sahel to early November over the southern Sahel. The climatological demise date for the Sahel region is October 20^{th} if the 2 mm day^{-1} threshold is applied to the area-averaged time series of the GPCP climatology.

The demise date varies by up to 25 days during the 1979-2012 period, with earliest and latest demise on October 5^{th} and 30^{th}, respectively. The interannual variations are analyzed by compositing early, normal and late monsoon demise years. Two periods are studied: October 5^{th}-20^{th} (Period 1) and October 20^{th} -30^{th} (Period 2).

An early (late) demise of the West African monsoon is associated with an anomalously strong (weak) NASH, which extends over the Mediterranean and Sahara, during both Period 1 and 2. Anticyclonic (cyclonic) flow anomalies corresponding to a stronger (weaker) NASH are shown as northerly/northeasterly (southerly/southwesterly) wind anomalies over the Sahel. The southerly monsoon flow shows no difference between the early and late demise composites.

Years with an early monsoon demise have less total rainfall than years with a late demise. The monsoon season total rainfall is significantly correlated with the demise date.

The atmospheric moisture budget is examined using values from the 6-hourly ERA-Interim reanalysis. The rainfall anomalies are mainly supported by anomalies in the vertically-integrated moisture flux convergence. Over the southern Sahel, the vertically-integrated moisture fluxes are divergent in the climatology for both Periods 1 and 2. In the early (late) demise composite, the northerly (southerly) moisture flux anomalies, which enhance (reduce) moisture divergence, are associated with northerly (southerly) wind anomalies in the lower troposphere due to an anomalously strong (weak) NASH. Analysis of the moisture convergence profiles in the southern Sahel (10.5°N) reveals that, corresponding to an early monsoon demise, a stronger NASH is associated with mid-level divergent and low-level convergent anomalies of the meridional moisture term (C_y); and negative anomalies of the meridional moisture advection (A_y) over the southern Sahel. The opposite applies for a late monsoon demise. These results connect the NASH variations with the rainfall anomalies over the Sahel.

The early (late) demise of the West African monsoon is accompanied by cold (warm) SSTAs in the subtropical North Atlantic. There is potential to use these findings for seasonal prediction of the date of the monsoon demise in the Sahel and, therefore, seasonal rainfall totals.

Table 4.1. Correlation coefficients of monsoon season total rainfall and demise date

Items	Correlation coefficient	*p*_value
GPCP total rainfall and GPCP demise date	0.56	0.0006
TRMM total rainfall and TRMM demise date	0.40	0.1363
GPCP total rainfall and GPCP demise date (1998-2012)	0.44	0.1032

Table 4.2. Correlation coefficients between GPCP and TRMM during the common period (1998-2012) for monsoon demise date and total rainfall.

Items	Correlation coefficient	*p*_value
GPCP demise date and TRMM demise date (1998-2012)	0.98	3.81×10^{-10}
GPCP total rainfall and TRMM total rainfall (1998-2012)	0.96	9.65×10^{-9}

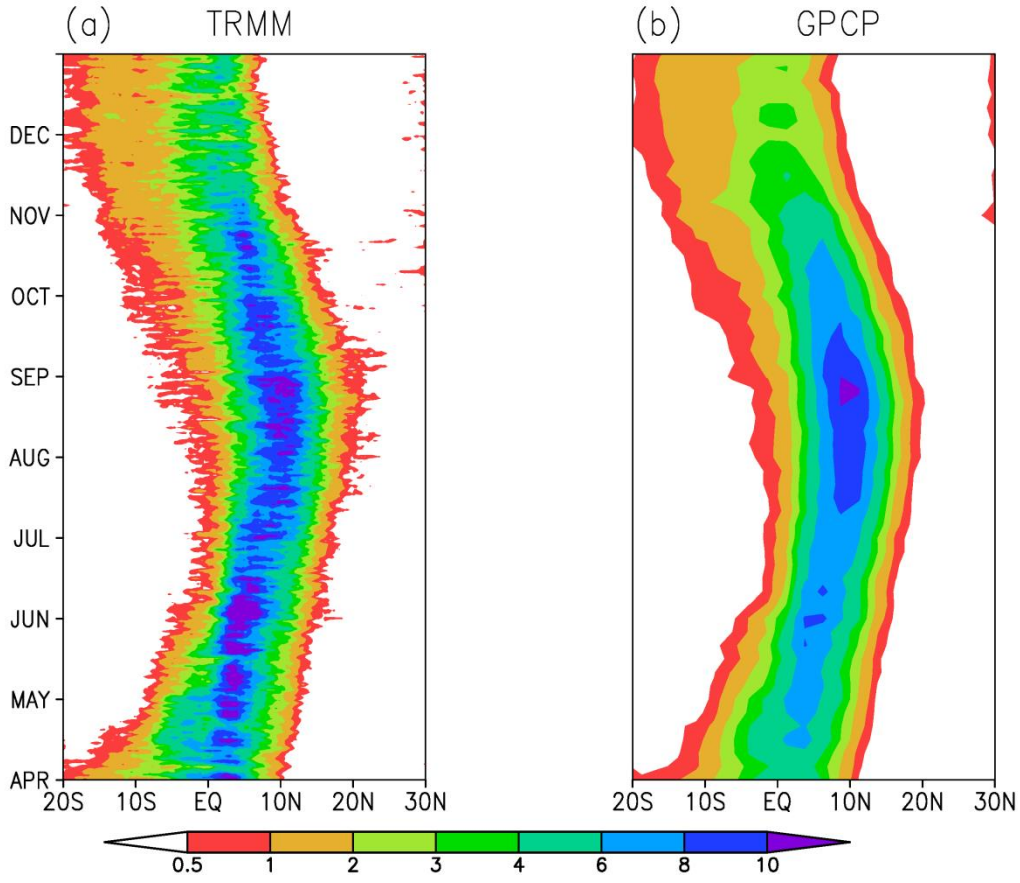

Figure 4.1. Hovmöller diagram of rainfall climatology (mm day^{-1}) from (a) TRMM (1998-2012) and (b) GPCP (1979-2012) averaged over the Sahel (20ºW-22.5ºE).

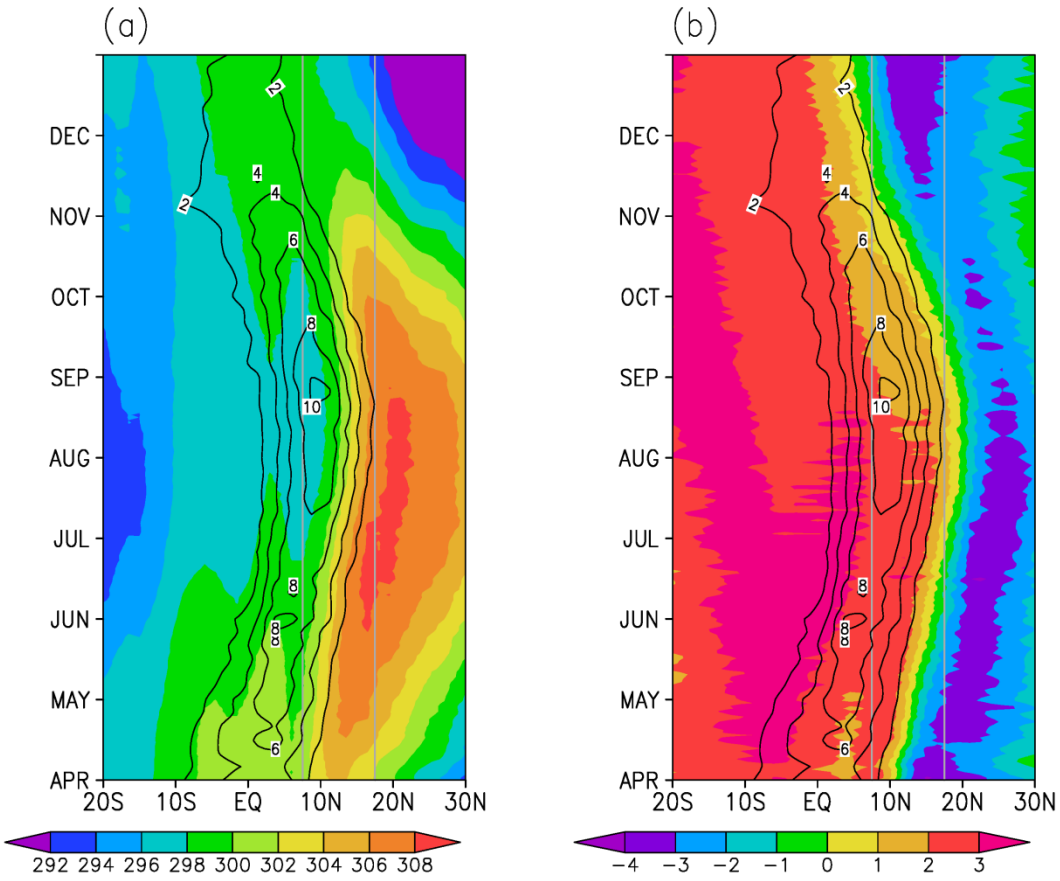

Figure 4.2. Hovmöller diagram (shaded) from the ERA-Interim climatology (1979-2012) of the (a) surface skin temperature (K) and (b) 925 hPa meridional wind (m s^{-1}) averaged over the Sahel (20ºW-22.5ºE). Black contours are Hovmöller diagram of rainfall climatology (mm day^{-1}) from GPCP as in Figure 1(b) for reference. Two grey lines indicate 7.5ºN and 17.5ºN, respectively.

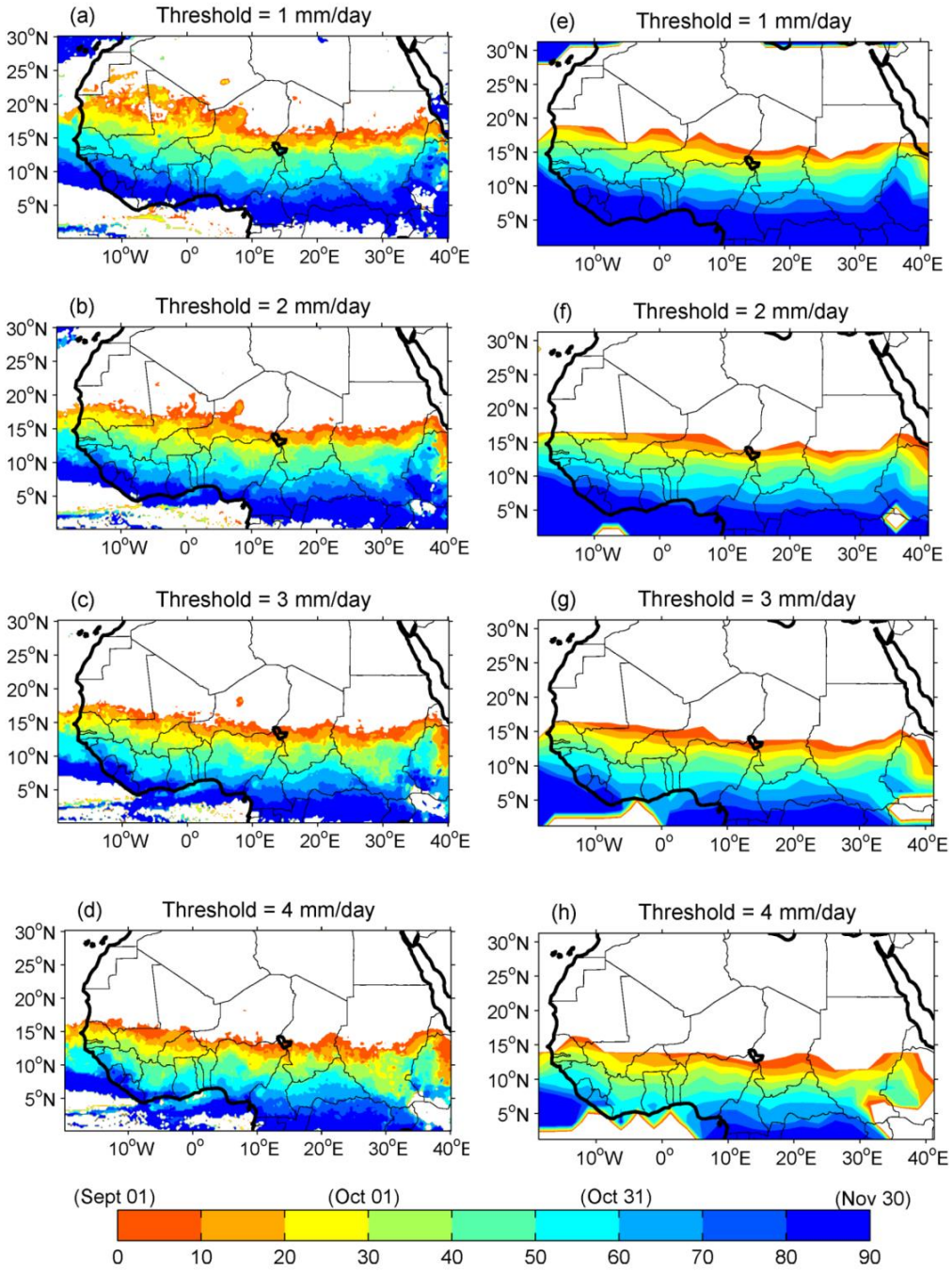
(a) Threshold = 1 mm/day
(e) Threshold = 1 mm/day
(b) Threshold = 2 mm/day
(f) Threshold = 2 mm/day
(c) Threshold = 3 mm/day
(g) Threshold = 3 mm/day
(d) Threshold = 4 mm/day
(h) Threshold = 4 mm/day
30°N
25°N
20°N
15°N
10°N
5°N
10°W
0°
10°E
20°E
30°E
40°E
(Sept 01)
(Oct 01)
(Oct 31)
(Nov 30)
0
10
20
30
40
50
60
70
80
90

Figure 4.3.

Figure 4.3. Map of demise dates from the TRMM climatology (1998-2012) using (a) 1 mm day^{-1}, (b) 2 mm day^{-1}, (c) 3 mm day^{-1}, and (d) 4 mm day^{-1} thresholds. The demise date is calculated for each grid point, and those earlier than September 1st or later than November 30th are blanked. (e)–(h) are the same as (a)–(d) but for the GPCP climatology (1979-2012).

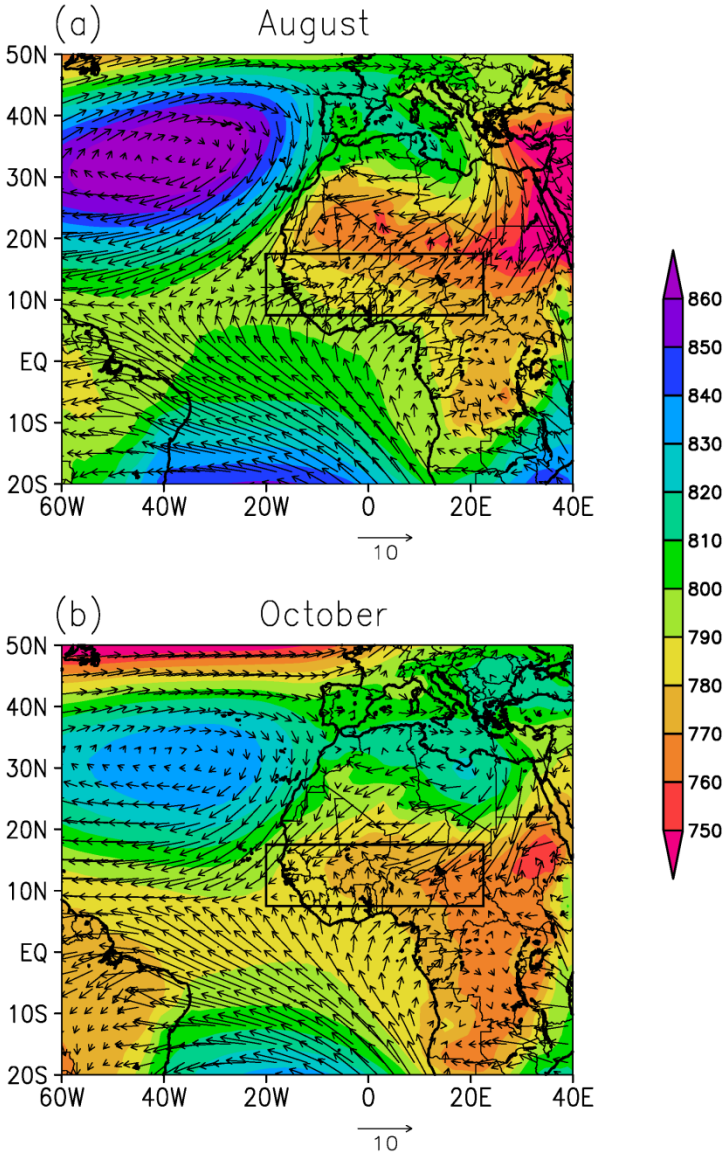

Figure 4.4. The 925-hPa geopotential height (gpm, shaded) and wind (m s^{-1}, vectors) from the ERA-Interim 1979-2012 climatology for (a) August and (b) October. Box indicates the Sahel averaging region (20ºW-22.5ºE, 7.5ºN-17.5ºN).

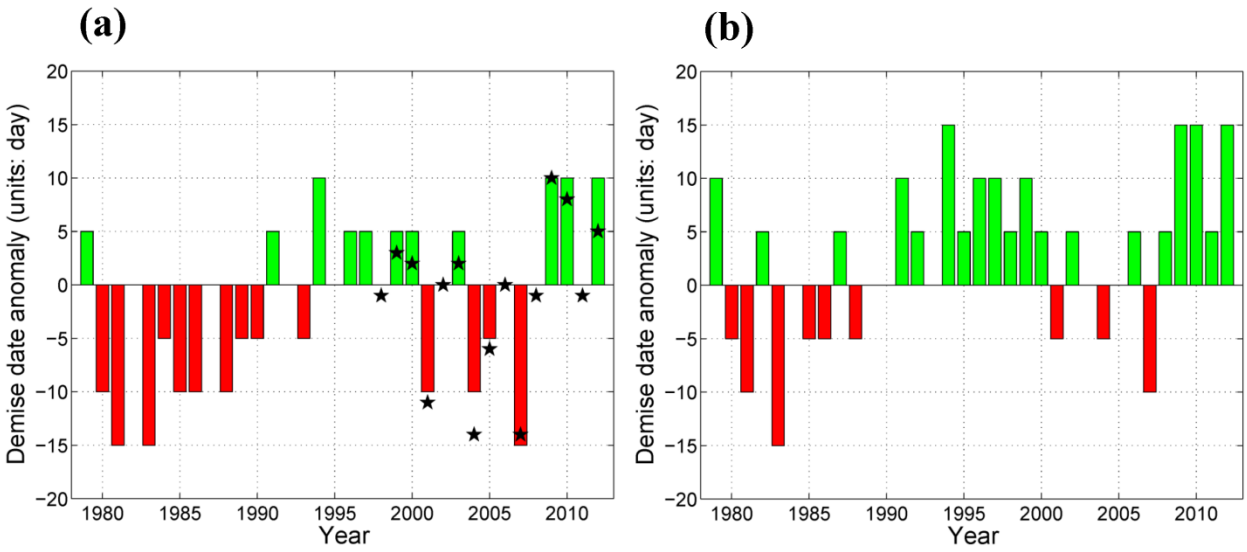

Figure 4.5. (a) West African monsoon demise date anomaly (day) in GPCP for 1979-2012. Bar (star) indicates the monsoon demise date anomaly in GPCP (TRMM). Both the GPCP and TRMM data place the climatological demise date on October 20th. (b) Same as (a) but for the sensitivity test using the southern half box and only GPCP data. The climatological demise date is October 15th.

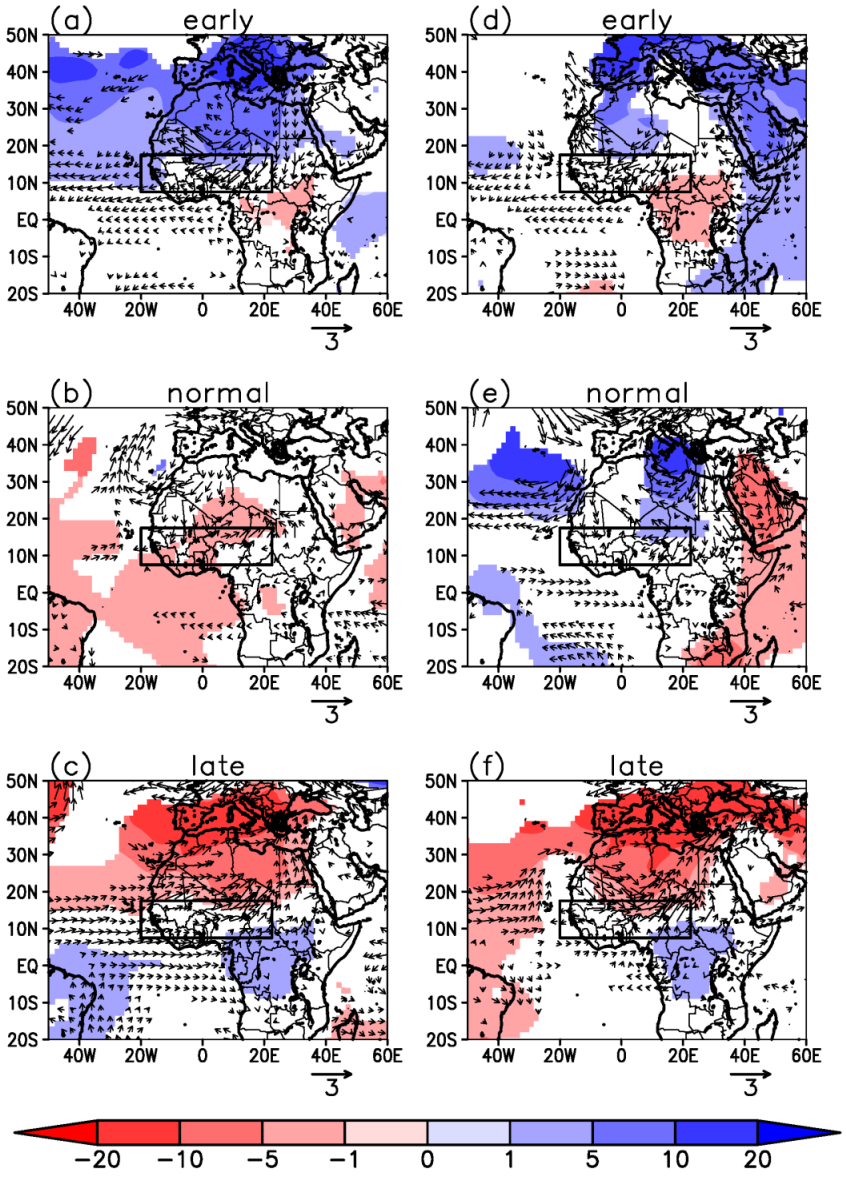
(a) early
(d) early
(b) normal
(e) normal
(c) late
(f) late
50N
40N
30N
20N
10N
EQ
10S
20S
40W
20W
0
20E
40E
60E
3
−20
−10
−5
−1
0
1
5
10
20

Figure 4.6.

Figure 4.6. Anomalies of 925 hPa geopotential height (gpm, shaded) and wind (m s^{-1}, vectors) averaged over Period 1 (October 5th -20th) in the (a) early demise composite, (b) normal demise composite, and (c) late demise composite. (d)-(f) As in (a)-(c), but for Period 2 (October 20th-30th). Only anomalies statistically significant at the 95% confidence interval are shown.

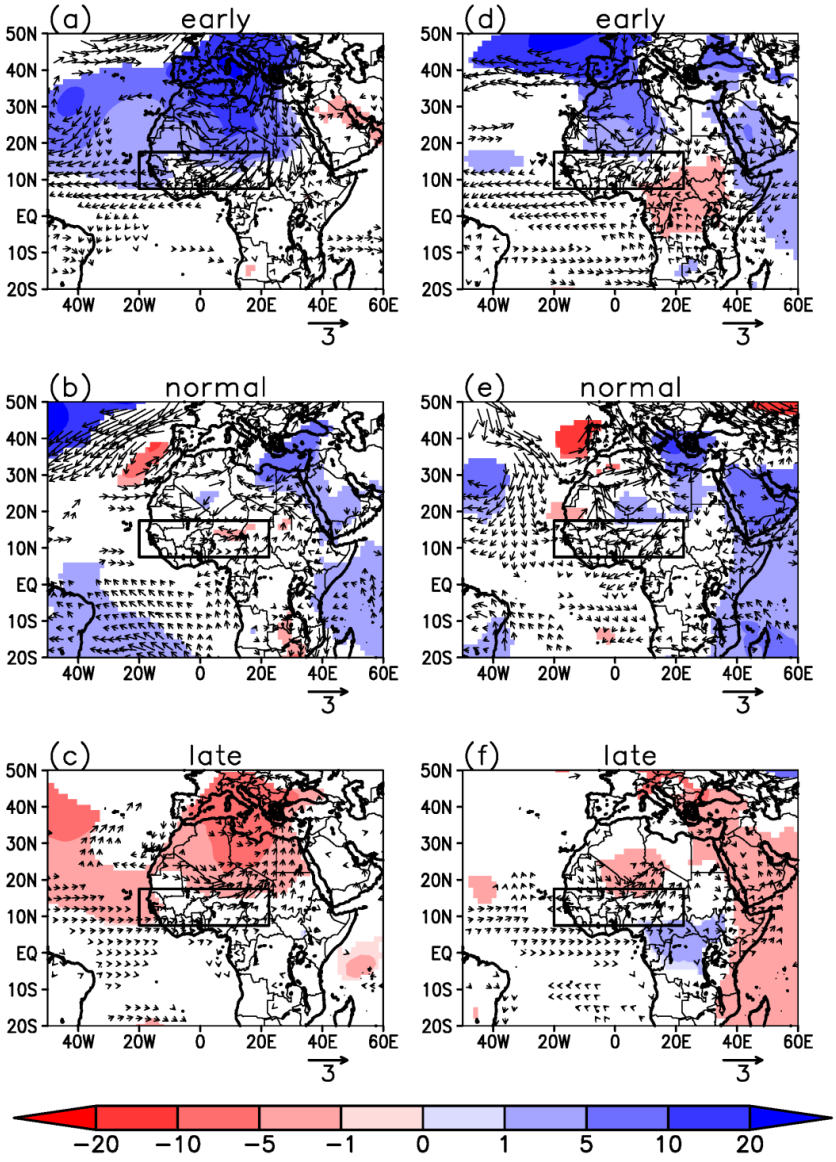

Figure 4.7. Same as Figure 4.6, but for the sensitivity test using the southern half box.

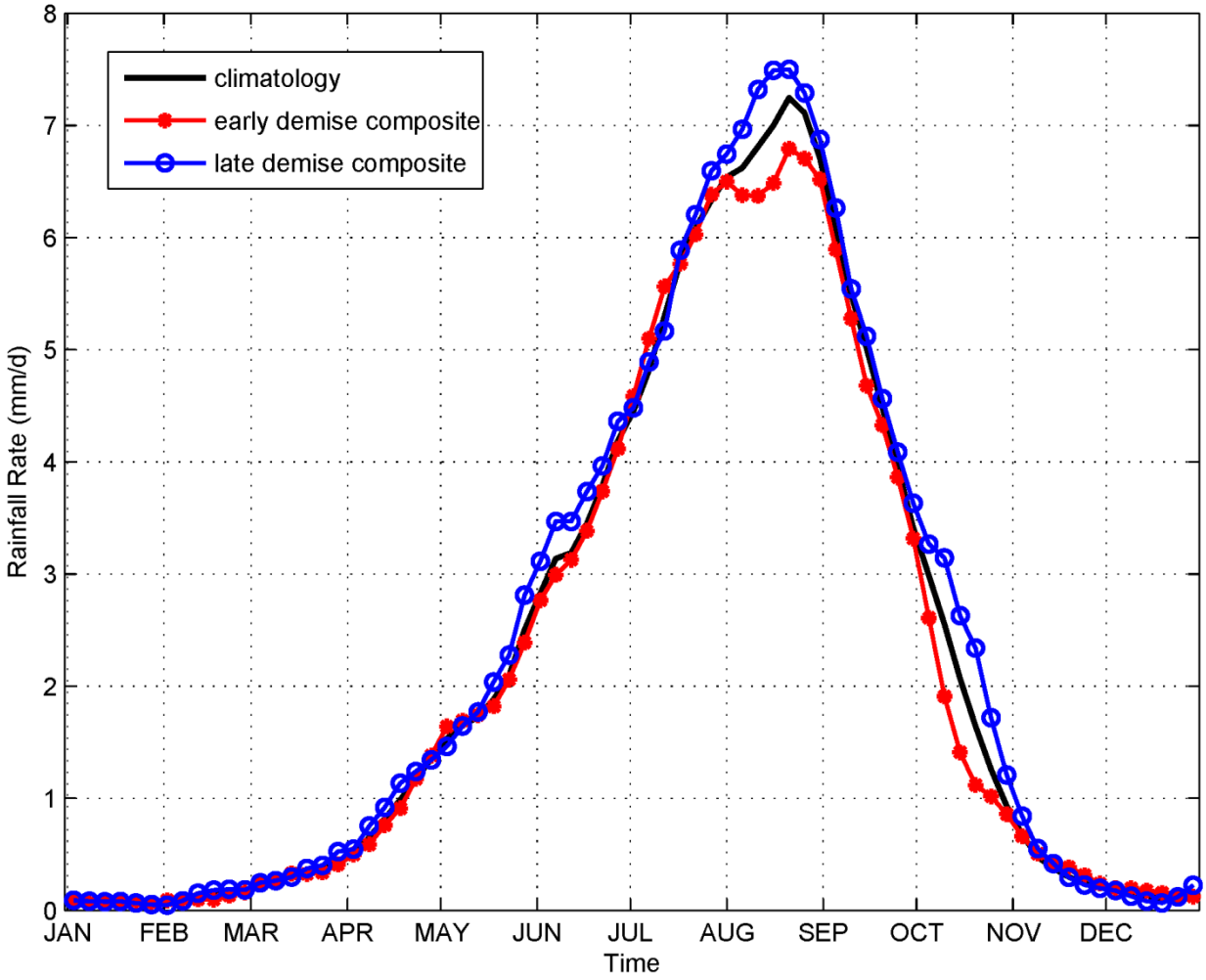

Figure 4.8. Seasonal cycle of the area-averaged Sahel rainfall (mm day^{-1}) in the GPCP climatology, early demise composite and late demise composite. A 15-day running average is applied.

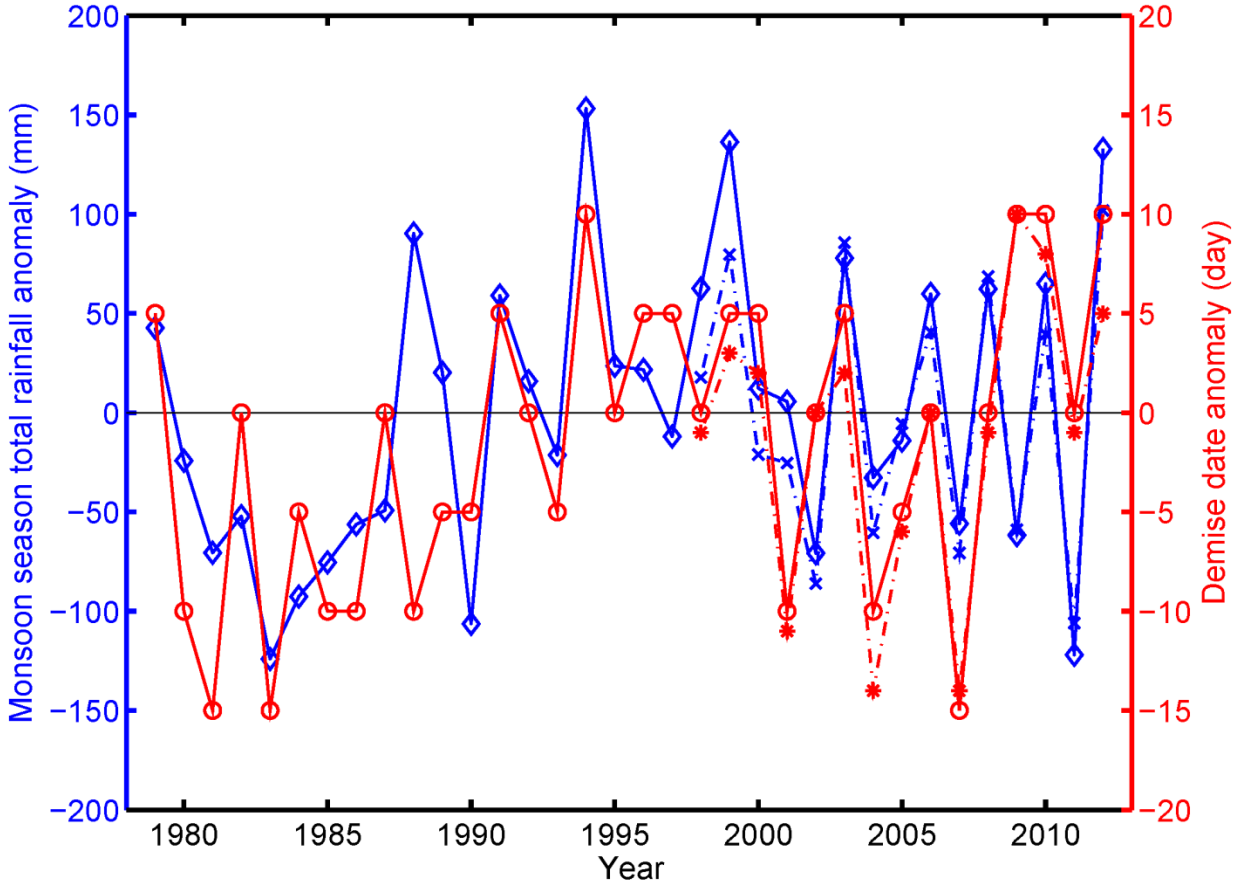

Figure 4.9. Monsoon season total rainfall anomaly (mm) and demise date anomaly (day). Blue solid (dotted-dashed) line denotes monsoon season total rainfall anomaly from GPCP for 1979-2012 (TRMM for 1998-2012). Red solid (dotted-dashed) line denotes demise date anomaly from GPCP for 1979-2012 (TRMM for 1998-2012).

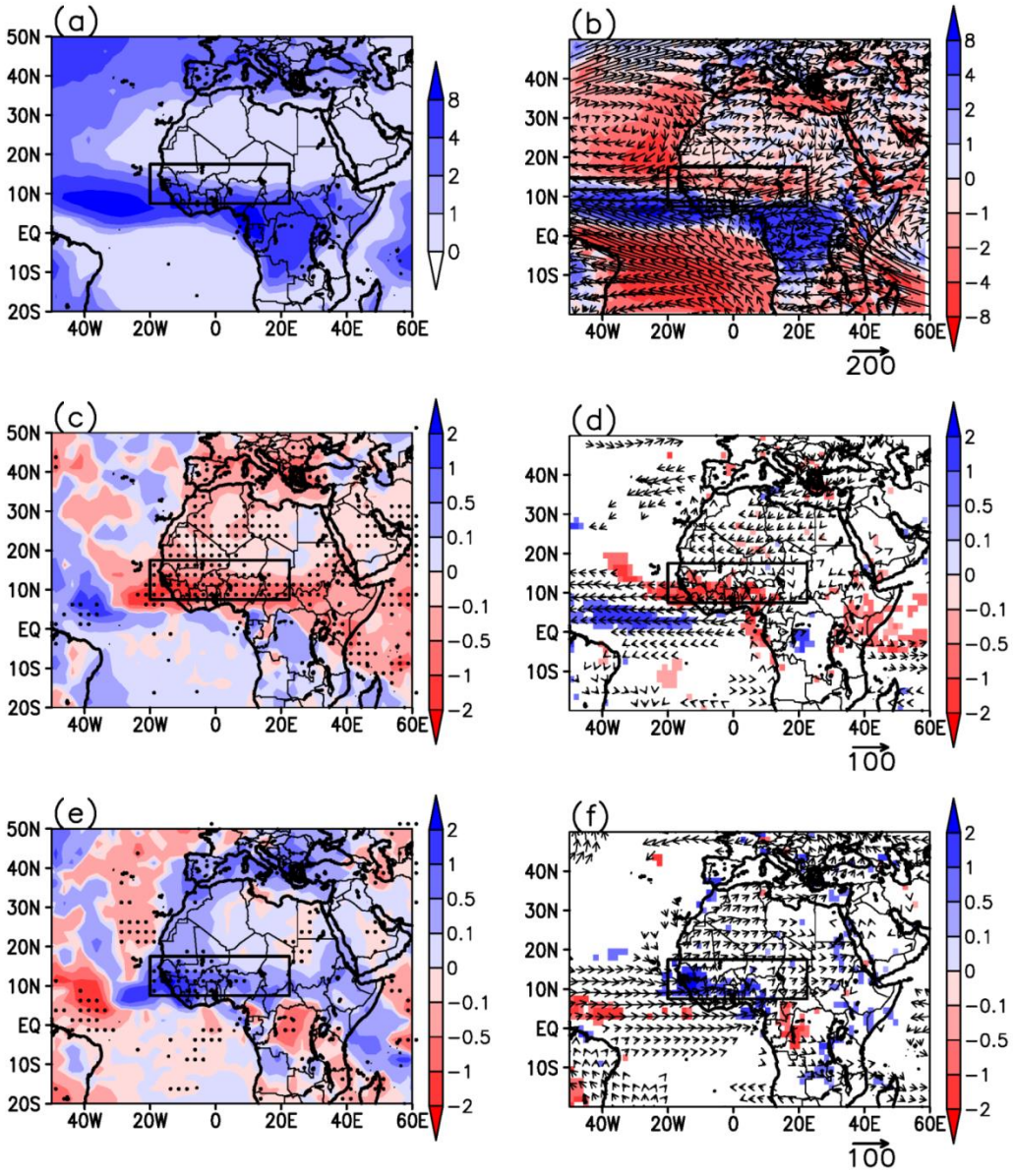
(a)
(b)
(c)
(d)
(e)
(f)
50N
40N
30N
20N
10N
EQ
10S
20S
40W
20W
0
20E
40E
60E
8
4
2
1
0
−1
−2
−4
−8
0.5
0.1
−0.1
−0.5
200
100

Figure 4.10.

Figure 4.10. Period 1 (October 5th -20th) climatology of (a) GPCP rainfall (mm day^{-1}) and (b) vertically-integrated moisture flux (kg m^{-1}s^{-1}, vector) and convergence (mm day^{-1}, shaded). (c)-(d) As in (a)-(b) but for anomalies in the early demise composite, and (e)-(f) as in (a)-(b) but for anomalies in the late demise composite. In (c) and (e), anomalies statistically significant at the 95% confidence interval are stippled; in (b) and (f), only anomalies statistically significant at the 95% confidence interval are shown.

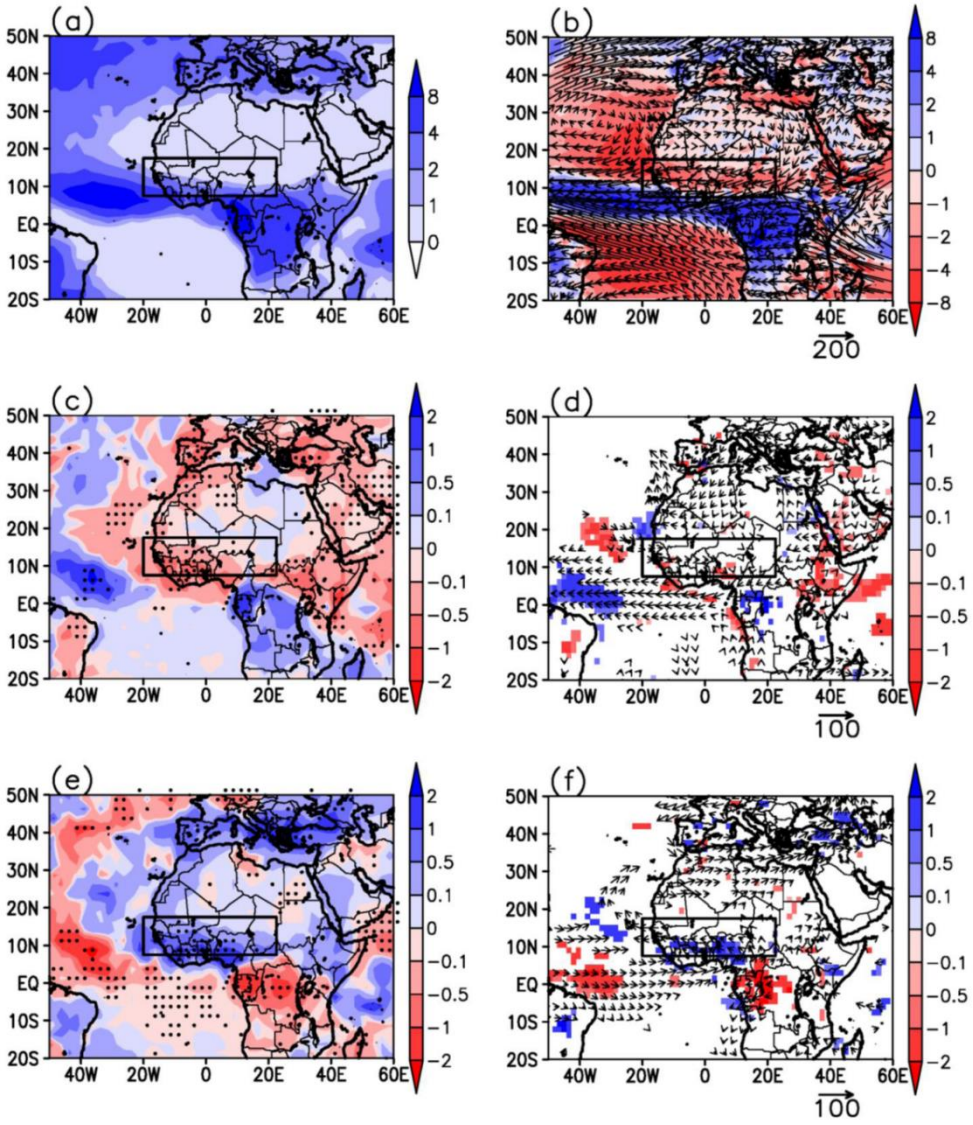

Figure 4.11. Same as Figure 4.10, but for Period 2 (October 20th-30th).

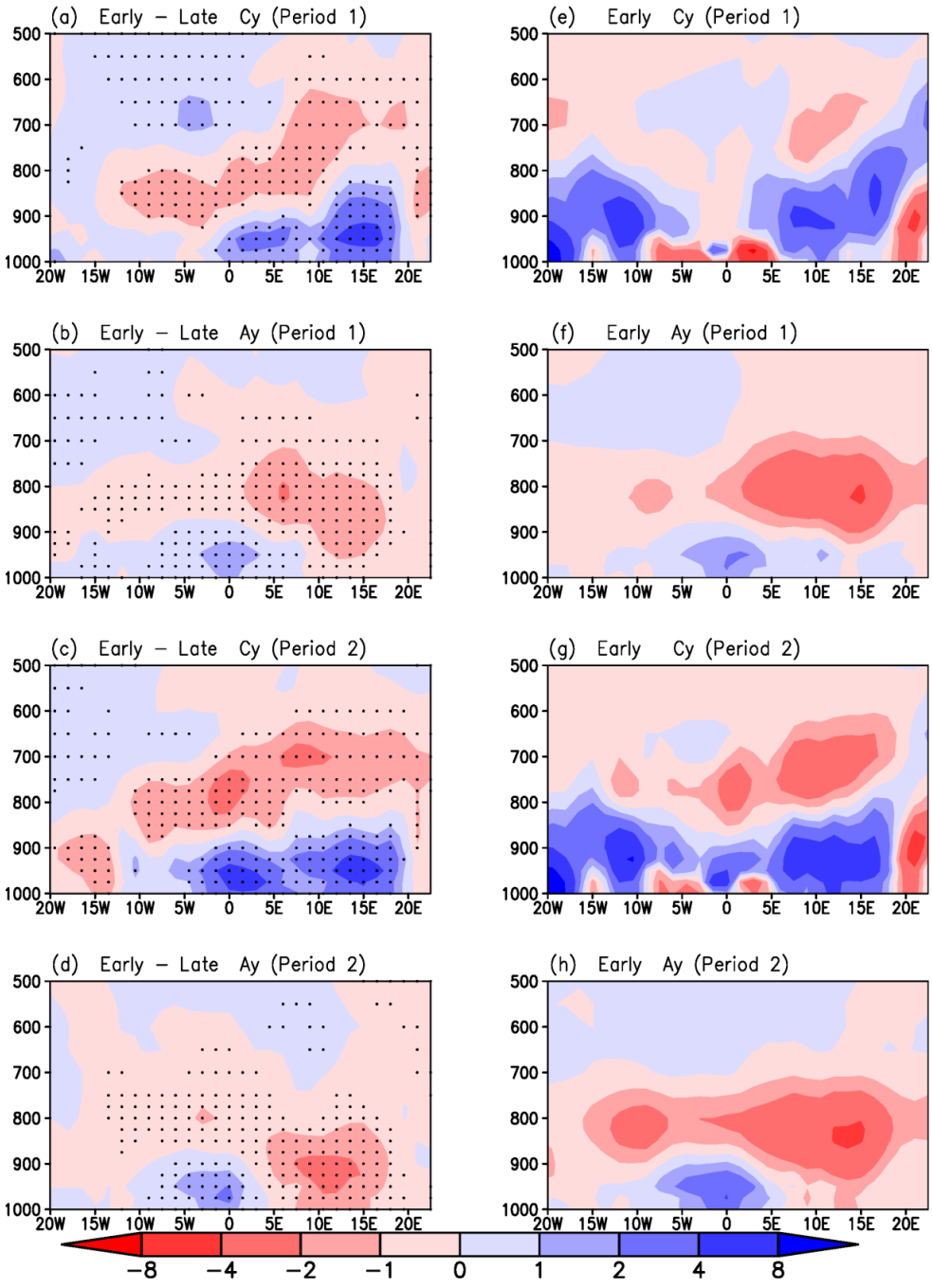
(a) Early – Late Cy (Period 1)
(e) Early Cy (Period 1)
(b) Early – Late Ay (Period 1)
(f) Early Ay (Period 1)
(c) Early – Late Cy (Period 2)
(g) Early Cy (Period 2)
(d) Early – Late Ay (Period 2)
(h) Early Ay (Period 2)
500
600
700
800
900
1000
20W 15W 10W 5W 0 5E 10E 15E 20E
−8 −4 −2 −1 0 1 2 4 8

Figure 4.12.

Figure 4.12. Cross section at 10.5 ºN of differences between early and late (early minus late) demise composites of the (a) meridional convergence term (C_y) and (b) meridional advection term (A_y) for Period 1 (October 5^{th} -20^{th}). (c)-(d) As in (a)-(b) but for Period 2 (October 20^{th}-30^{th}). Units are 10^{-8} kg(H_2O) kg(air)$^{-1}$ s^{-1}. Differences statistically significant at the 95% confidence interval are stippled. (e)-(h) Shows the full field of each term in the early demise composite, corresponding to (a)-(d), respectively.

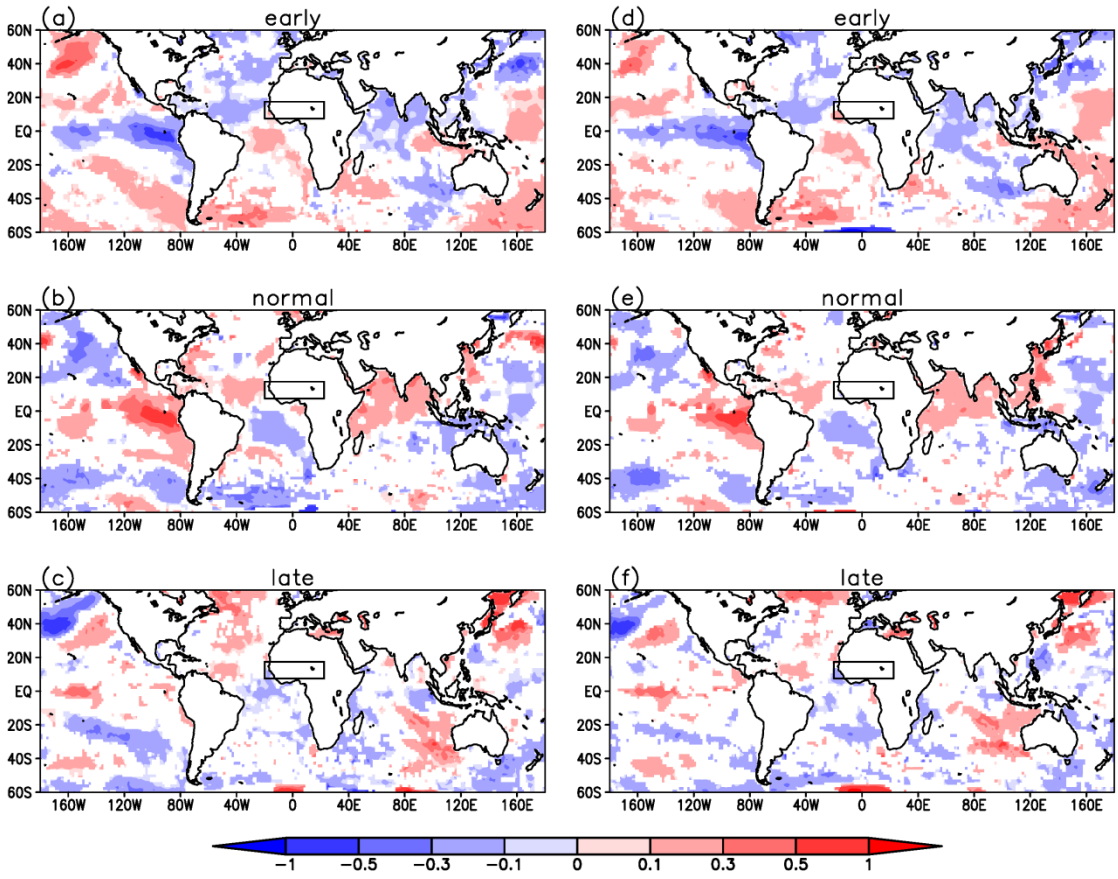

Figure 4.13. ERA-Interim sea surface temperature anomalies (K) for Period 1 (October 5th -20th) in the (a) early demise composite, (b) normal demise composite, and (c) late demise composite. (d)-(f) As in (a)-(c), but for Period 2 (October 20th-30th). The global warming trend is removed by subtracting the global mean SST averaged between 60ºS and 60ºN. Only anomalies statistically significant at the 95% confidence interval are shown.

Chapter 5: Sensitivity of Tropical Climate Dynamics to An Increase of CO_2 in Idealized Simulations

ABSTRACT

To understand the climate sensitivity in the tropics given an increase greenhouse gases, regional climate model simulation are conducted with boundary conditions of ideally shaped continents and oceans. The model domain is from 150°W to 150°E and from 50°S to 50°N. Two ideal continents are configured in the domain, the western continent at 120°W-60°W and 30°S-30°N, and the eastern continent at 60°E-120°E and 30°S-30°N. The rest of the domain is covered by ocean and modeled by the ocean mixed-layer model coupled within the regional model. Two groups of simulations are conducted: the control simulation (CTL) with modern level of CO2 concentration and future simulation (2×CO2) in which the CO2 concentration is twice of the modern level.

Model simulations show that the northwestern part of the western continent is up to 6 K warmer in the 2×CO2 simulation than in the CTL. In the 2×CO2 simulation, the continental heat low is deeper and the subtropical highs in both northern and southern hemispheres are stronger than in CTL. Over the western continent, the rainfall maxima shift southward, with a larger slope of northeast-southwest orientation. In addition, over the eastern continent, the rainfall maxima remain zonally oriented, with a decrease of rainfall over the center.

5.1. INTRODUCTION

Dynamics of the tropical climate is an essential component in global climate system and hydrological cycle. Under the global warming scenarios with increasing

greenhouse gases, it is important to understand how the tropics responses to this forcing. Some of the tropical regions, e.g. the semi-arid West African Sahel region, are sensitive to climate changes. A better understanding of climate sensitivity in the tropics will help people in these regions prepare for mitigation and adaption of agricultural practices, water resource management, etc.

One important driver of the tropical climate sensitivity is the land-sea distribution. Land has a smaller heat capacity; therefore it always warms or cools faster than the oceans. This thermal contrast is an important driver of tropical climate sensitivity given the same greenhouse gases forcing. However, in the real world, the signal of the land-sea contrast is complicated due to the shape and location of the continents on the Earth. To better understand the climate sensitivity in the tropics related to the land-sea distribution, in this chapter we use a coupled regional climate with idealized continents and oceans. This idealized approach will reduce other factors involved in the tropical climate and highlight the role of land-sea distribution, which has been widely used in studying climate dynamics. The idealized model can be built up with more complexity until reached to the full complexity of an operational climate system model. This hierarchical structure in modeling the climate system has the advantage that any finding in the idealized models can be easily transferred and applied to understand the full-complexity model.

Current literature on tropical climate sensitivity and idealized simulations is reviewed in the following section. The methodology used in this chapter is described in section 3. Results are presented in section 4, and conclusions are summarized in section 5.

5.2. BACKGROUND

Current literature on the sensitivity of tropical climate is mainly focused on the regional climate trend in the past century and future climate projections under global warming scenarios. Deser et al. (2010) show significant trend of tropical SSTs in the 20th century, with warming in the whole tropics except northwestern Atlantic. They also suggest that the maxima of the SST warming trend are located in both northern and southern mid-latitudes. In recent decade, the global warming rate slows down, which is referred as "global warming hiatus". Using global model experiments, Kosaka and Xie (2013) suggest that the recent global warming hiatus is related to a cold phase of ENSO-like decadal cooling, due to the natural variability of the climate system. The warming or cooling of SSTs also has profound regional impacts on the atmospheric and/or ocean circulations. For example, Tokinaga et al. (2012) find that the observed weakening of the Walker Circulation during 1950-2009 is caused by a decrease of zonal SST gradient in the Pacific Ocean, which is related to the SST warming patterns. Another example of the sensitivity of regional SST warming is that, Wu et al. (2012) find that in the past century there is an accelerated warming trend of SSTs over the regions of subtropical western boundary currents. Associate with this enhanced warming, the global western boundary currents intensify and/or shift poleward.

The warming trend for the land surface is also studied. For example, Cook and Vizy (2015) suggest an amplified surface warming in the Sahara desert in response to enhanced greenhouse gas forcing. Due to the difference in heat capacity, the land and the ocean respond to the greenhouse gas forcing at different warming rate. Using global model simulations in Coupled Model Inter-comparison Project Phase 3 (CMIP3), Sutton et al. (2007) conclude that the global land/sea warming ration is about 1.36-1.84, and this ratio is time-invariant, which means an amplifying of land/sea thermal difference with

time. The land/sea warming difference is important to the atmospheric circulations and rainfall over the tropical and subtropical regions. Cook (2000) explores the basic dynamics of the South Indian convergence zone (SICZ) and suggests that the SICZ shifts northeastward in response to an ENSO-like warming in the eastern Pacific.

Besides the modeling studies using full-complexity regional and/or global models with real world configuration, the idealized simulation is also an invaluable approach in understanding the physical processes and separating climate feedbacks. The author's supervisor, Dr. Kerry H. Cook, has conducted several modeling studies in the past by applying idealized model simulations in understanding the basic dynamics of the climate. For example, Cook and Gnanadesikan (1991) use a GCM with idealized boundary conditions for the African continent to explore the impacts of land surface on tropical rainfall. Cook et al. (2004) also use idealized simulations with a GCM to reveal the interactions between the African climate and South American climate. The idealized simulation is not only useful for the tropics, but also for other regions on the Earth. For example, Shi and Durran (2014) apply ideally shaped continents and mountains in the mid-latitudes in a GCM to investigate the response of orographic rainfall to greenhouse gases forcing. Besides GCMs, Shi and Durran (2015) also use a regional climate model, i.e., the Weather Research and Forecasting (WRF) model, for a similar study but with a focus on extreme rainfall.

5.3. METHODOLOGY

This study is built on "idealized simulations", i.e., regional climate simulations with idealized configuration of continents and oceans on the Earth. The model we choose is a coupled regional ocean-atmosphere model, which enables us to study to two-way

interaction between the atmosphere and the ocean. Also, a land surface model is always included in an atmospheric model; therefore, the land-atmosphere interactions are also included in the coupled regional climate model. The atmospheric component of the coupled regional climate model is the Weather Research and Forecasting (WRF) model version 3.1 (Skamarock et al. 2008). The ocean component of the coupled regional climate model is an intermediate-complexity ocean mixed-layer model developed within the author's supervisor, Dr. Kerry H. Cook's group (Hagos and Cook 2009). This model is further developed and applied successfully in the Atlantic Ocean (Vizy and Cook 2014). In this chapter, this coupled model is extended to a broad tropical domain with ideal continents and oceans.

Figure 1 shows the domain of the idealized simulations for this chapter. The domain covers from 150°W to 150°E and from 50°S to 50°N. The domain is chosen to be larger than what we need in order to avoid analyzing outputs near the lateral boundaries. Two ideal continents are configured in the domain, the western continent at 120°W-60°W and 30°S-30°N, and the eastern continent at 60°E-120°E and 30°S-30°N. Both of the continents are flat with a uniform elevation of 500 m. The land properties are uniformly set to reduce complexity. The soil type is set as clay and vegetation type is set as savanna, which are typical over tropical continents. The fraction of vegetated area in a grid box is set as 70% constantly. The rest of the domain is covered by ocean, represented by the ocean mixed-layer in the coupled model.

Two groups of simulations are conducted: the control simulation (CTL) with modern level of CO_2 concentration and future simulation ($2\times CO_2$) in which the CO_2 concentration is twice of the modern level. The model is run at 90 km resolution. The simulations are initialized at 00 UTC on 15 October 2005 and run through 15 October 2006. The boreal summer warm season (i.e., June to August, JJA) is analyzed. Initial and

boundary conditions for the atmosphere are taken from the 6-hourly National Centers for Environmental Prediction (NCEP) II Reanalysis (Kanamitsu et al. 2002). Although the model is configured ideally, we still supply realistic 6-hourly lateral boundary conditions because this will keep the transient eddies on the lateral boundaries. Our domain is large enough to avoid influence of the lateral boundary conditions on the interior domain analysis. Note that this is a coupled ocean-atmosphere model; therefore SST is only need as the initial condition. The ocean mixed-layer model is initialized with zonally uniform SST field derived from October monthly mean climatology in NCEP II reanalysis. Figure 2 displays the variations of initial SST along the latitudes of the domain.

Physical parameterizations selected for use in the simulation include: Lin et al. microphysics scheme (Chen and Sun 2002), RRTM longwave radiation scheme (Mlawer et al. 1997), Dudhia shortwave radiation scheme (Dudhia 1989), Yonsei University boundary layer scheme (Hong et al. 2006), MM5 Monin-Obukhov surface layer scheme (Skamarock et al. 2008), Noah land surface model (Chen and Dudhia 2001), and Kain-Fritsch (Kain 2004) scheme of cumulus convection parameterization The model integration time step is 180 seconds, and 6-hourly model output is archived for analysis.

5.4. RESULTS

5.4.1 Surface response to doubling CO_2

The boreal summer (JJA) is analyzed to investigate the differences between the CTL and $2\times CO_2$ simulations. Our focus is the thermal contrasts between the idealized continents and the oceans in response to the increase of CO_2. First, the surface temperature of both land and oceans are examined. Figure 1a shows the CTL simulation of surface temperature, which is SST over the oceans simulated by the ocean-mixed

model, and land surface temperature over the two square continents simulated by the Noah land surface model. As expected, the model produces a higher temperature over the continents in the northern hemisphere, compared with adjacent oceans. Figure 3a also shows the ocean mixed-layer currents as vectors. The currents are mainly poleward in both hemispheres. Strongest currents are shown near the equator, and the current speed decreases from low to high latitudes in general.

Figure 3b displays the surface temperature and ocean mixed-layer currents in the $2\times CO_2$ simulation and Figure 3c shows the difference between $2\times CO_2$ and CTL ($2\times CO_2$ minus CTL). No obvious difference is found for the SSTs and ocean mixed-layer currents. One prominent feature is that the northwestern part of the western continent, near the northern coast, is up to 6 K warmer in the $2\times CO_2$ simulation than in the CTL.

5.4.2 Impacts on low-level circulation and rainfall

The warming over the northern hemisphere continents is associated with solar heating during the boreal summer, and it influences the low-level atmospheric circulation. Figure 4a displays 900 hPa geopotential height and wind in CTL simulation. Over the continents in the northern hemisphere, the model produces continental heat lows. The continental heat low is stronger in the western continent than in the eastern one, with maxima located at 110°W and 15°N. The continental heat low in the eastern continent is much weaker and more confined.

In addition, a profound subtropical high pressure system is simulated in the northern hemisphere, centered along 30°N over the oceans. Accompanying this subtropical high is anticyclonic winds in the subtropical regions. The counterpart of this

subtropical high in the southern hemisphere is much weaker and located mainly in the eastern section of the domain.

Figure 4b shows the 900 hPa geopotential height and wind in the $2\times CO_2$ simulation and Figure 4c shows the difference between $2\times CO_2$ and CTL ($2\times CO_2$ minus CTL). Because the center of the continental heat low has a warming with doubling CO_2 (Figure 3), the continental heat low is deepened in the $2\times CO_2$ simulation, suggested by the negative anomalies of geopotential height in Figure 4c. In the subtropics, the subtropical highs in both northern and southern hemispheres are stronger in $2\times CO_2$ than in CTL, associated with anticyclonic wind anomalies around the subtropical high.

The low-level circulation patterns are associated with tropical rainfall distributions, e.g., the inter-tropical convergence zones (ITCZ) and the monsoons. For example, in Chapter 4, we conclude that the demise of the West African monsoon is associated with the variability of the North Atlantic subtropical high (NASH) (Zhang and Cook 2014). Here we explore the rainfall changes between these two simulations.

Figure 5a shows the JJA seasonal mean rainfall simulated in the CTL simulation. The model captures the ITCZ, but also produces a secondary rainfall maximum between 60°W and 0°. This secondary maximum suggests that the coupled model may also suffer the common "double ITCZ" problem in coupled AOGCMs.

Over the continents, the model produces rainfall maxima in the northern hemisphere land regions where the continental heat lows are located. The rainfall maxima over the western continent show a northeast-southwest orientation between 10°N and 25°N. The rainfall maxima over the eastern continent is more zonal, and within a small region, which is consistent with the fact that the continental heat low is also weaker and confined over this continent.

Figure 5b shows the JJA seasonal mean rainfall simulated in the $2\times CO_2$ simulation and Figure 5c shows the difference between $2\times CO_2$ and CTL ($2\times CO_2$ minus CTL). The large-scale rainfall pattern is similar between these two simulations. Over the western continent, the rainfall maxima shift southward over the northwestern part of the continent, with a larger slope of northeast-southwest orientation. Therefore, it generates more rainfall interior of the continent. However, over the eastern continent, the rainfall maxima remain zonal. But the rainfall rate is reduced over the center.

5.5. CONCLUSIONS

To advance the understanding of climate sensitivity in the tropics under the scenario of increasing greenhouse gases, a series of regional climate model simulations are conducted with idealized continents and oceans. This idealized approach simplifies the physical processes and feedbacks involved in the climate system and helps better identify the sensitivity of the climate system to greenhouse gas changes.

Two groups of simulations are conducted: the control simulation (CTL) with modern level of CO_2 concentration and future simulation ($2\times CO_2$) in which the CO_2 concentration is twice of the modern level. The boreal summer warm season (i.e., June to August, JJA) is analyzed. In both experiments, the model produces a higher temperature over the continents in the northern hemisphere, compared with adjacent oceans. The ocean mixed-layer currents are mainly poleward in both hemispheres. Strongest currents are shown near the equator, and the current speed decreases from low to high latitudes in general. No obvious difference is found for the SSTs and ocean mixed-layer currents between the $2\times CO_2$ simulation and the CTL, probably due to a relatively short period of

spin-up. One prominent feature is that the northwestern part of the western continent, near the northern coast, is up to 6 K warmer in the $2\times CO_2$ simulation than in the CTL.

In the CTL simulation, the continental heat low is stronger in the western continent than in the eastern continent, with maxima located at 110°W and 15°N. The continental heat low in the eastern continent is much weaker and more confined. A profound subtropical high is simulated in the northern hemisphere, centered along 30°N over the oceans. The counterpart of this subtropical high in the southern hemisphere is much weaker and located mainly in the eastern section of the domain. In the $2\times CO_2$ simulation, the continental heat low is deeper and the subtropical highs in both northern and southern hemispheres are stronger than in CTL.

Over the continents, the model produces rainfall maxima over the northern hemisphere land associated with the continental heat lows. The rainfall maxima over the western continent show a northeast-southwest orientation. The rainfall maxima over the eastern continent are more zonal, and limited within a small region. In the $2\times CO_2$ simulation, the large-scale rainfall pattern is similar to the CTL. However, over the western continent, the rainfall maxima shift southward, with a larger slope of northeast-southwest orientation. In addition, over the eastern continent, the rainfall maxima remain zonal, with a decrease of rainfall over the center.

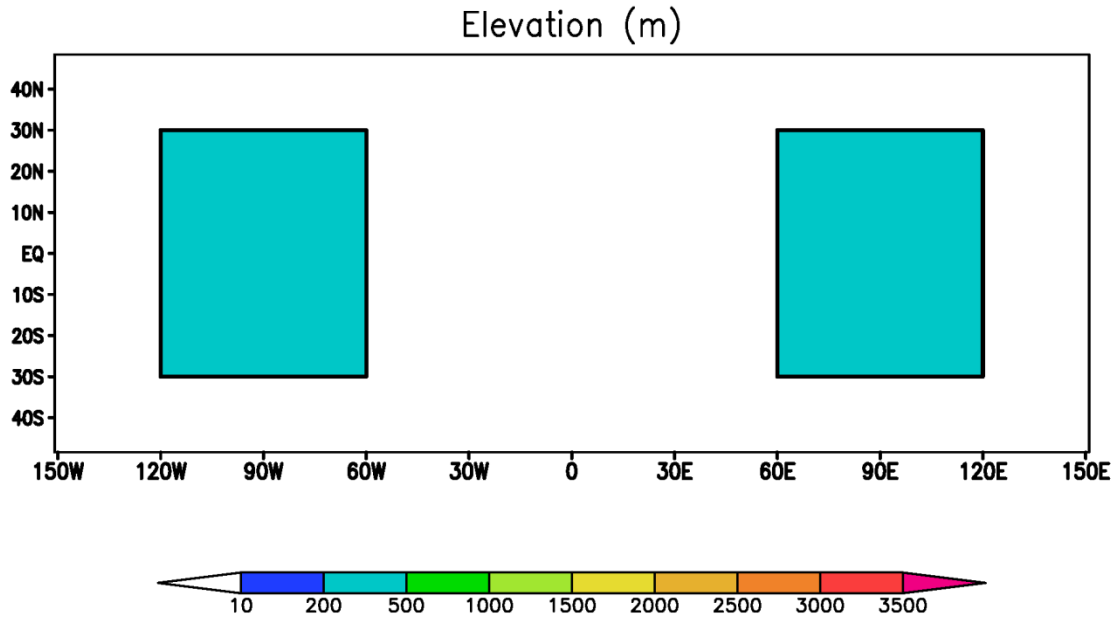

Figure 5.1. Model domain for the idealized simulations. Elevation (m) of the continents is shaded, and the ocean is shown as white.

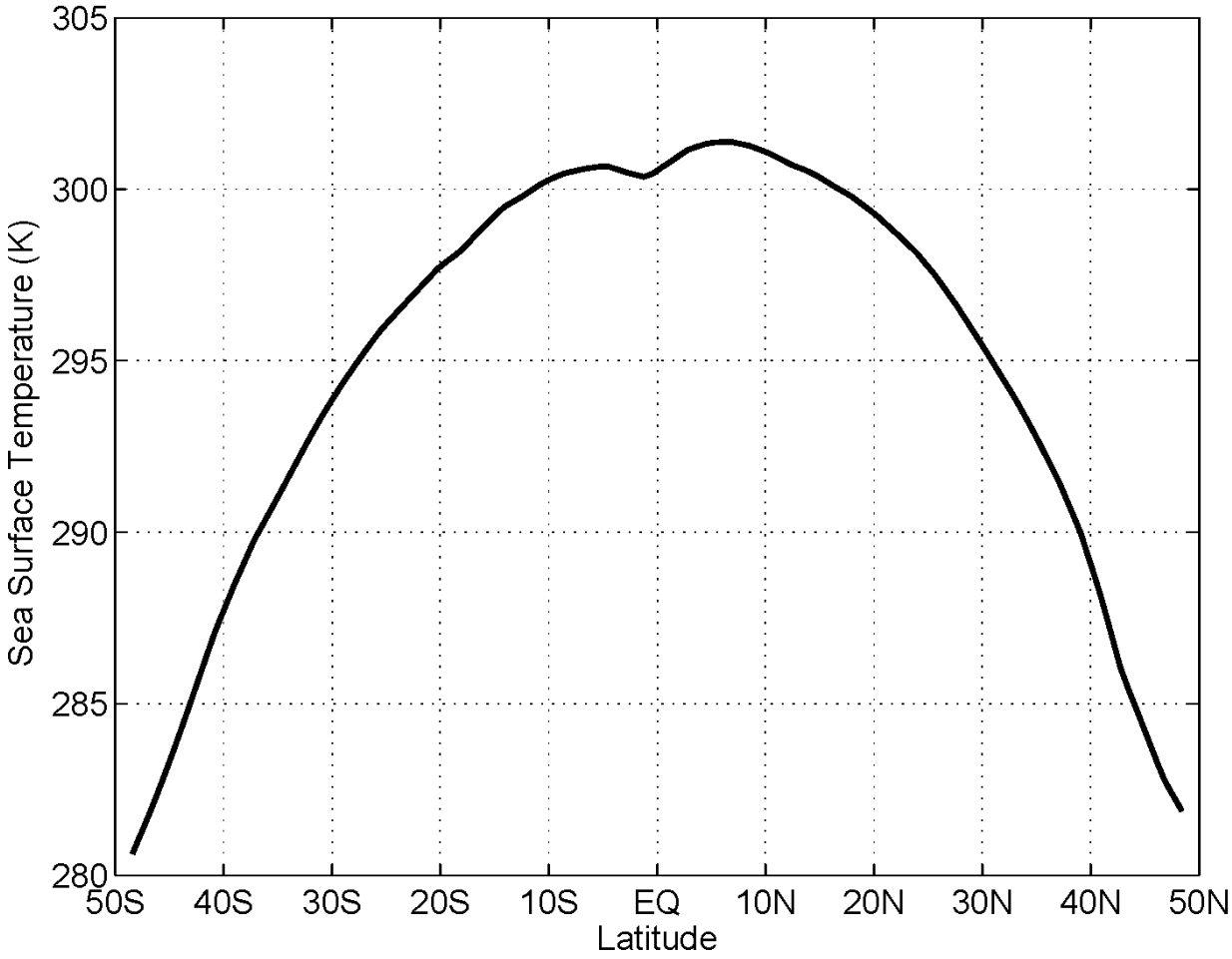

Figure 5.2. Zonally uniform sea surface temperature (SST, K) derived from October climatology in NCEP II reanalysis.

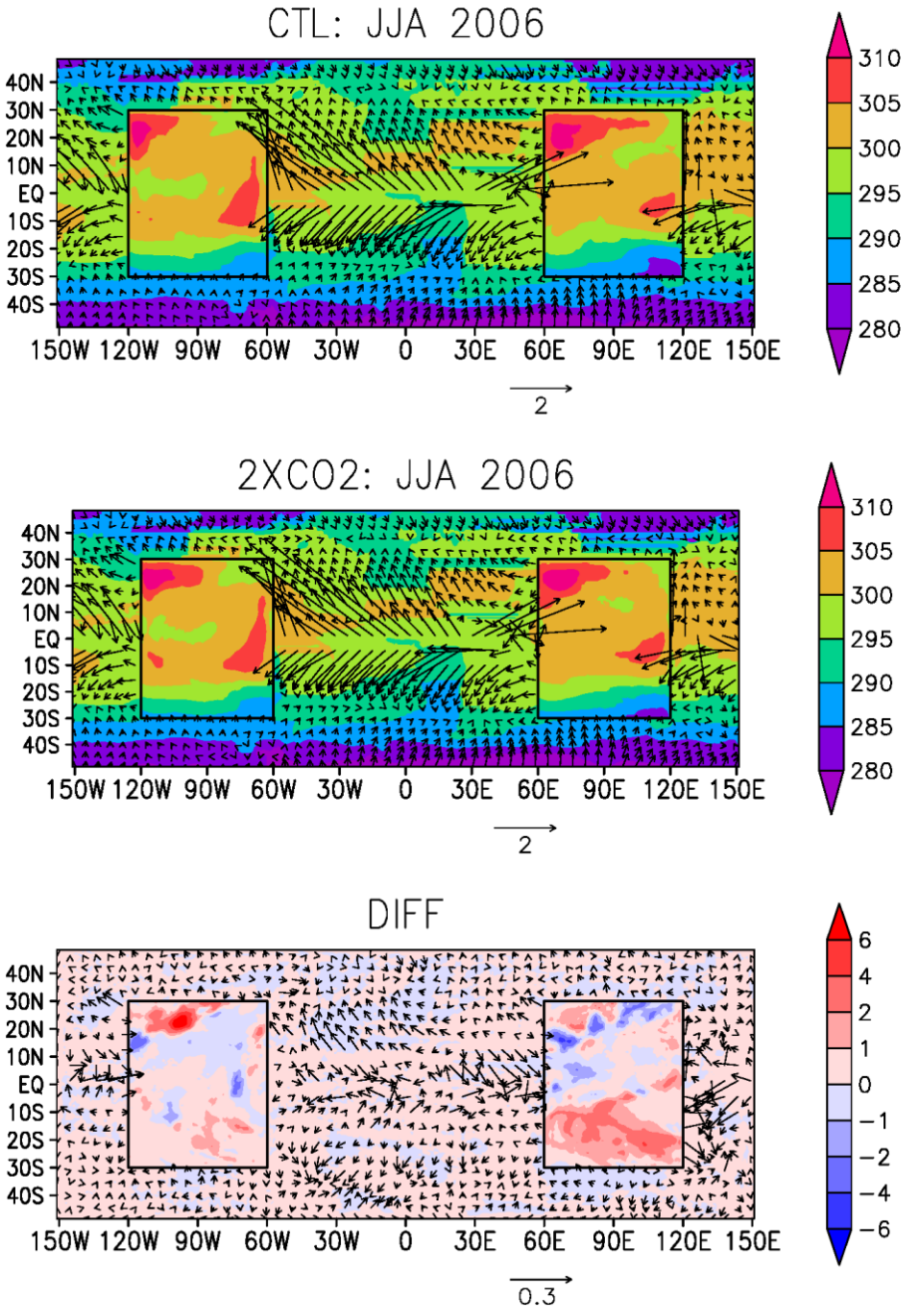
CTL: JJA 2006
40N
30N
20N
10N
EQ
10S
20S
30S
40S
150W 120W 90W 60W 30W 0 30E 60E 90E 120E 150E
2
310
305
300
295
290
285
280
2XCO2: JJA 2006
40N
30N
20N
10N
EQ
10S
20S
30S
40S
150W 120W 90W 60W 30W 0 30E 60E 90E 120E 150E
2
310
305
300
295
290
285
280
DIFF
40N
30N
20N
10N
EQ
10S
20S
30S
40S
150W 120W 90W 60W 30W 0 30E 60E 90E 120E 150E
0.3
6
4
2
1
0
−1
−2
−4
−6

Figure 5.3.

Figure 5.3. The JJA 2006 surface temperature (K, shaded) and ocean mixed-layer current (m s^{-1}, vectors) for (a) CTL simulation and (b) $2\times CO_2$ simulation. (c) Differences of (b) and (a) ($2\times CO_2$ minus CTL).

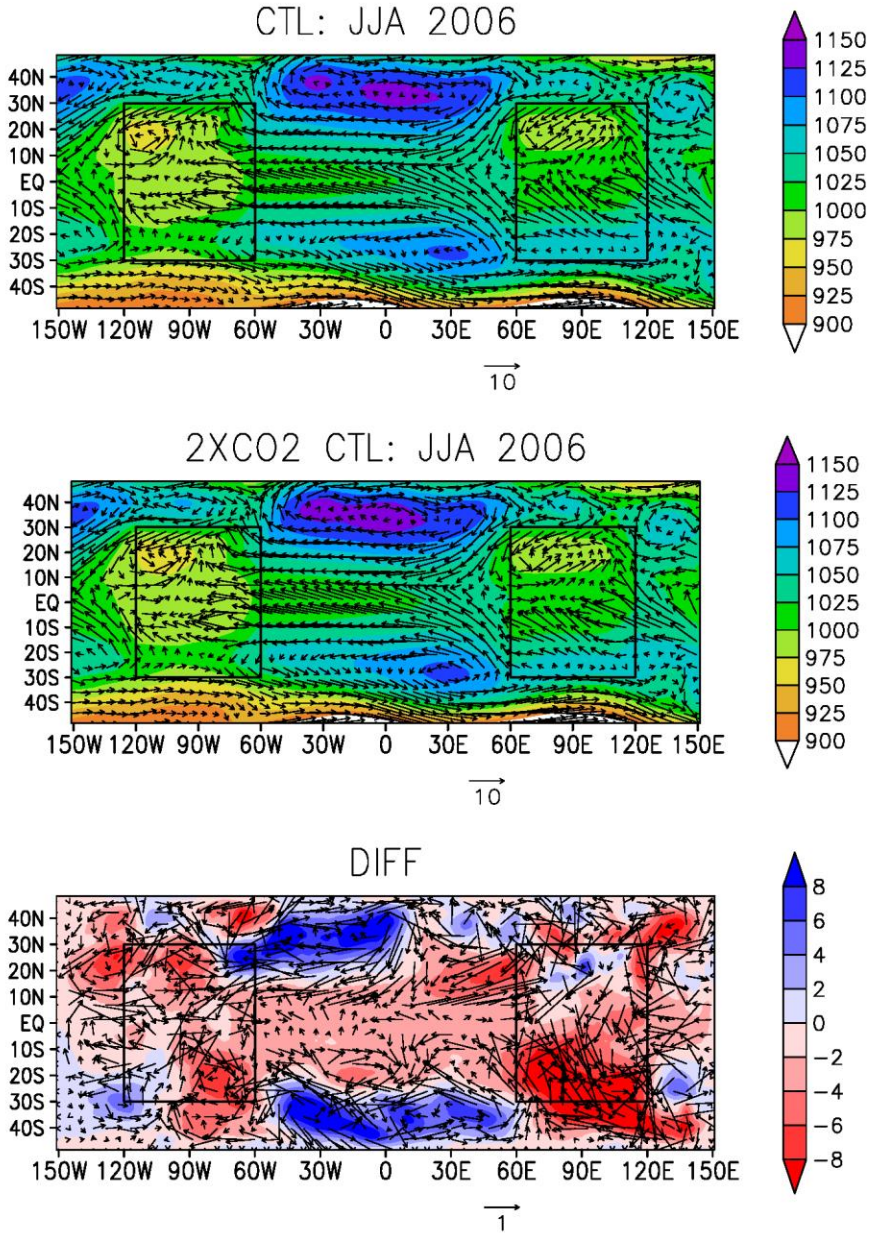

Figure 5.4. The JJA 2006 900 hPa geopotential height (m, shaded) and wind (m s^{-1}, vectors) for (a) CTL simulation and (b) 2×CO_2 simulation. (c) Differences of (b) and (a) (2×CO_2 minus CTL).

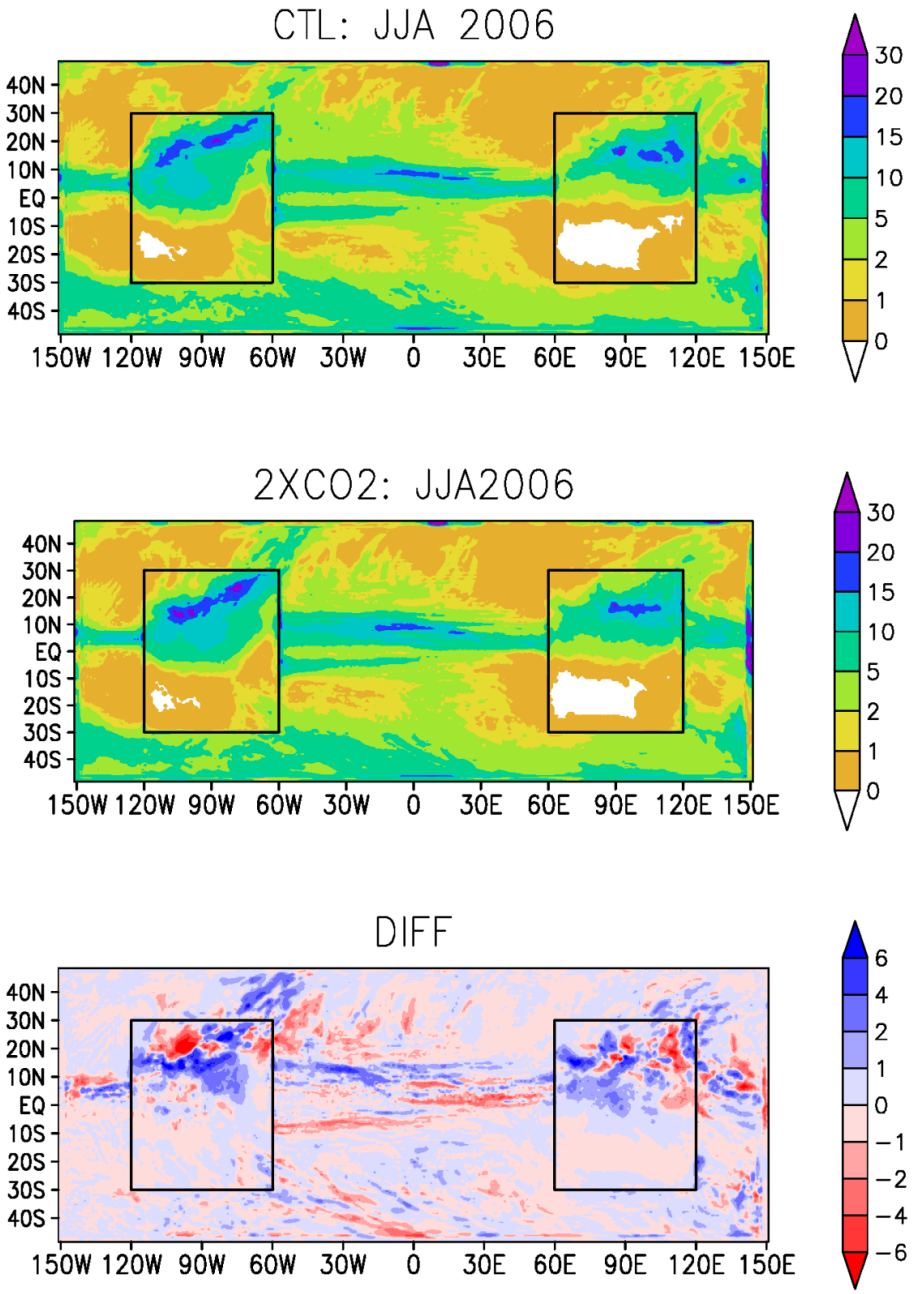
CTL: JJA 2006
40N
30N
20N
10N
EQ
10S
20S
30S
40S
150W 120W 90W 60W 30W 0 30E 60E 90E 120E 150E
30
20
15
10
5
2
1
0
2XCO2: JJA2006
40N
30N
20N
10N
EQ
10S
20S
30S
40S
150W 120W 90W 60W 30W 0 30E 60E 90E 120E 150E
30
20
15
10
5
2
1
0
DIFF
40N
30N
20N
10N
EQ
10S
20S
30S
40S
150W 120W 90W 60W 30W 0 30E 60E 90E 120E 150E
6
4
2
1
0
−1
−2
−4
−6

Figure 5.5.

Figure 5.5. The JJA 2006 mean rainfall rate (mm day^{-1}, shaded) for (a) CTL simulation and (b) $2\times CO_2$ simulation. (c) Differences of (b) and (a) ($2\times CO_2$ minus CTL).HIDDEN TEXT: The following sample text and headings are for information only. Delete them after browsing.

Chapter 6: General Conclusions

6.1 CONCLUSIONS

This dissertation is focused on advancing the current knowledge of the tropical climate dynamics and rainfall variability, by using observational analysis and climate modeling studies. In addition to the first chapter as general introduction and this chapter as general conclusion, this dissertation includes four major chapters: (1) The diurnal cycle of warm season rainfall over West Africa: Observations as Chapter 2 and high-resolution simulation as Chapter 3; (2) West African Monsoon Demise: Climatology, Interannual Variations, and Relationship to Seasonal Rainfall as Chapter 4; and (3) Sensitivity of tropical climate dynamics to an increase of CO_2 in idealized simulations as Chapter 5.

In Chapter 2, we investigate the geographical distribution of the diurnal cycle of West African warm season (JJAS) rainfall and explore its underlying physical processes using the satellite-derived TRMM precipitation and atmospheric dynamics fields from the MERRA reanalysis. In addition, a convection-permitting regional model simulation is analyzed to investigate the model's ability to capture the physical processed that control the diurnal cycle of rainfall. The diurnal cycle of rainfall is analyzed in the TRMM climatology for 1998-2013. We also evaluate the 2006 warm season (JJAS) as a case study to facilitate a more detailed investigation on synoptic timescales.

The conclusions from this observational analysis in Chapter 2 are summarized as follows. Most regions of West Africa (98% in the climatology and 78% in 2006) have a single diurnal peak of rainfall in either the afternoon (i.e., 15 and 18 UTC) or at night (i.e., 21, 00, and 03 UTC). This finding is in contrast to several previous studies (see

section 2.) that suggest that the diurnal cycle of rainfall over West Africa is characterized by two peaks. This is a vestige of averaging over a large area, and the result does not apply locally or regionally. Two types of regions experience afternoon rainfall peaks. One is regions with topographic features, and the other is regions far removed from upstream topography. In these regions, local instability processes dominate. A moist static energy analysis is used to show that the afternoon rainfall peaks are associated with unstable atmospheric profiles dominated by diurnal temperature variations in the lower troposphere; boundary layer moisture variations play a minor role. Coherent regions with nocturnal rainfall peaks are located 3°-10° of longitude downstream (i.e., to the west) of regions with afternoon rainfall maxima. These rainfall peaks are associated with the westward propagation of rainfall systems, but not with local instability. The diurnal cycle of rainfall is closely associated with the timing of extreme rainfall events. 12 extreme events that occurred at night during the summer of 2006 are examined, and each is found to be associated with an MCS that originated on the previous afternoon to the east and propagated to the west.

Results from the convection-permitting regional model simulations in Chapter 3 are the following. The model realistically simulates seasonal mean rainfall and low-level circulation fields. Moreover, the westward propagating nature of rainfall is well-captured in the convection-permitting simulation, which is a distinct advantage compared to the rainfall simulated in GCMs or regional climate models at coarser resolutions with convective parameterization activated. The convection-permitting simulation captures the afternoon rainfall peaks associated with elevated topography, e.g., around the Jos Plateau. Nocturnal rainfall peaks downstream of the topographic afternoon rainfall are also well-simulated. The model fails to reproduce the observed afternoon rainfall peaks. Nocturnal

rainfall is too widespread and, as a result, localized convective instability does not develop with sufficient vigor.

In Chapter 4, the observed climatology and interannual variations of the West African monsoon demise are examined using TRMM 1998-2012 daily data and GPCP 1979-2012 5-day pentad data. The atmospheric circulations and large-scale SSTAs associated with interannual variations of the monsoon demise are analyzed in the ERA-Interim reanalysis. In the climatology, the demise of the West African monsoon occurs from September to early November as the rainfall maximum progresses southward from the Sahel to the Gulf of Guinea. The southerly monsoon flow into the Sahel (8ºN) decreases from more than 2 m s^{-1} in early September to less than 1 m s^{-1} in late October. Distinct from the abrupt onset, the monsoon demise is smooth with no evident meridional jump of the rainfall maximum. Applying uniform thresholds to indicate monsoon demise, the demise date is zonally uniform over the central and eastern Sahel, while the western Sahel has a later demise. Using a 2 mm day^{-1} threshold, the demise date varies from early September over the northern Sahel to early November over the southern Sahel. The climatological demise date for the Sahel region is October 20^{th} if the 2 mm day^{-1} threshold is applied to the area-averaged time series of the GPCP climatology.

The demise date varies by up to 25 days during the 1979-2012 period, with earliest and latest demise on October 5^{th} and 30^{th}, respectively. The interannual variations are analyzed by compositing early, normal and late monsoon demise years. Two periods are studied: October 5^{th}-20^{th} (Period 1) and October 20^{th} -30^{th} (Period 2). An early (late) demise of the West African monsoon is associated with an anomalously strong (weak) NASH, which extends over the Mediterranean and Sahara, during both Period 1 and 2. Anticyclonic (cyclonic) flow anomalies corresponding to a stronger (weaker) NASH are shown as northerly/northeasterly (southerly/southwesterly) wind anomalies over the

Sahel. The southerly monsoon flow shows no difference between the early and late demise composites. Years with an early monsoon demise have less total rainfall than years with a late demise. The monsoon season total rainfall is significantly correlated with the demise date.

The atmospheric moisture budget is examined using values from the 6-hourly ERA-Interim reanalysis. The rainfall anomalies are mainly supported by anomalies in the vertically-integrated moisture flux convergence. Over the southern Sahel, the vertically-integrated moisture fluxes are divergent in the climatology for both Periods 1 and 2. In the early (late) demise composite, the northerly (southerly) moisture flux anomalies, which enhance (reduce) moisture divergence, are associated with northerly (southerly) wind anomalies in the lower troposphere due to an anomalously strong (weak) NASH. Analysis of the moisture convergence profiles in the southern Sahel (10.5°N) reveals that, corresponding to an early monsoon demise, a stronger NASH is associated with mid-level divergent and low-level convergent anomalies of the meridional moisture term (C_y); and negative anomalies of the meridional moisture advection (A_y) over the southern Sahel. The opposite applies for a late monsoon demise. These results connect the NASH variations with the rainfall anomalies over the Sahel. The early (late) demise of the West African monsoon is accompanied by cold (warm) SSTAs in the subtropical North Atlantic.

In Chapter 5, to advance the understanding of climate sensitivity in the tropics under the scenario of increasing greenhouse gases, a series of regional climate model simulations are conducted with idealized continents and oceans. This idealized approach simplifies the physical processes and feedbacks involved in the climate system and helps better identify the sensitivity of the climate system to greenhouse gas changes.

Two groups of simulations are conducted: the control simulation (CTL) with modern level of CO_2 concentration and future simulation ($2\times CO_2$) in which the CO_2 concentration is twice of the modern level. The boreal summer warm season (i.e., June to August, JJA) is analyzed. In both experiments, the model produces a higher temperature over the continents in the northern hemisphere, compared with adjacent oceans. The ocean mixed-layer currents are mainly poleward in both hemispheres. Strongest currents are shown near the equator, and the current speed decreases from low to high latitudes in general. No obvious difference is found for the SSTs and ocean mixed-layer currents between the $2\times CO_2$ simulation and the CTL, probably due to a relatively short period of spin-up. One prominent feature is that the northwestern part of the western continent is up to 6 K warmer in the $2\times CO_2$ simulation than in the CTL.

In the CTL simulation, the continental heat low is stronger in the western continent than in the eastern continent, with maxima located at 110°W and 15°N. The continental heat low in the eastern continent is much weaker and more confined. A profound subtropical high pressure system is simulated in the northern hemisphere, centered along 30°N over the oceans. The counterpart of this subtropical high in the southern hemisphere is much weaker and located mainly in the eastern section of the domain. In the $2\times CO_2$ simulation, the continental heat low is deeper, and the subtropical highs in both northern and southern hemispheres are stronger than in CTL.

Over the continents, the model produces rainfall maxima in the northern hemisphere land associated with the continental heat lows. The rainfall maxima over the western continent show a northeast-southwest orientation. The rainfall maxima over the eastern continent are more zonal, and limited within a small region. In the $2\times CO_2$ simulation, the large-scale rainfall pattern is similar to the CTL. However, over the western continent, the rainfall maxima shift southward, with a larger slope of northeast-

southwest orientation. In addition, over the eastern continent, the rainfall maxima remain zonal, with a decrease of rainfall over the center

6.2 FUTURE WORK

For the study of diurnal cycle of rainfall in Chapters 2 and 3, future work is needed on addressing the deficiencies of current generation of general circulation models and regional climate models in representing the diurnal cycle of rainfall. This study demonstrates that atmospheric models can realistically simulate the diurnal cycle of rainfall if run at convective-permitting resolutions. The next step is to narrow the gap between models with parameterized convection and convection-permitting models. A series of model experiments are needed to be designed to reflect the capability/inability of model physics in simulating the convective processes related to the diurnal cycle of rainfall.

For the study of West African monsoon demise in Chapter 4, future work is need on further understanding the mechanism that controls the NASH variability, including the role of global SSTs. In addition, there is potential to use these findings for seasonal prediction of the date of the monsoon demise in the Sahel and, therefore, seasonal rainfall totals. In practice, the weather and climate models usually performs well in predicting the circulation, for example the NASH, but it is difficult for the models to predict rainfall. It will be useful to test if there is any predictability by using the prediction of the NASH to infer the anomaly of demise date in seasonal to interannual climate prediction.

For the study of the sensitivity of tropical climate in Chapter 5, more experiments of the idealized simulation are needed. In addition, it will be useful to compare the

simulation with some of the current generation AOGCM or AGCM simulations, e.g. the NCAR CESM large ensemble simulations.

References

Agustí-Panareda, A., and Coauthors, 2010: The ECMWF re-analysis for the AMMA observational campaign. *Q. J. R. Meteorol. Soc.*, **136**, 1457–1472.

Arias, P., R. Fu, and K. C. Mo, 2012: Decadal variation of rainfall seasonality in the North American monsoon region and its potential causes. *J. Clim.*, **25**, 4258–4274, doi:10.1175/JCLI-D-11-00140.1.

Le Barbé, L., and T. Lebel, 1997: Rainfall climatology of the HAPEX-Sahel region during the years 1950–1990. *J. Hydrol.*, **188-189**, 43–73.

Bechtold, P., N. Semane, P. Lopez, J.-P. Chaboureau, A. Beljaars, and N. Bormann, 2014: Representing equilibrium and nonequilibrium convection in large-scale models. *J. Atmos. Sci.*, **71**, 734–753.

Biasutti, M., 2013: Forced Sahel rainfall trends in the CMIP5 archive. *J. Geophys. Res. Atmos.*, **118**, 1–11, doi:10.1002/jgrd.50206.

Biasutti, M., and A. H. Sobel, 2009: Delayed Sahel rainfall and global seasonal cycle in a warmer climate. *Geophys. Res. Lett.*, **36**, 1–5, doi:10.1029/2009GL041303.

Birch, C. E., D. J. Parker, J. H. Marsham, D. Copsey, and L. Garcia-Carreras, 2014: A seamless assessment of the role of convection in the water cycle of the West African Monsoon. *J. Geophys. Res. Atmos.*, **119**, 2890–2912.

Chen, F., and J. Dudhia, 2001: Coupling an advanced land surface–hydrology model with the Penn State – NCAR MM5 modeling system . Part I : model implementation and sensitivity. *Mon. Weather Rev.*, **129**, 569–585.

Chen, S.-H., and W.-Y. Sun, 2002: A One-dimensional time dependent cloud model. *J. Meteorol. Soc. Japan.*, **80**, 99–118.

Cook, K. H., 1999: Generation of the African easterly jet and its role in determining West African precipitation. *J. Clim.*, **12**, 1165–1184.

——, 2000: The South Indian convergence zone and interannual rainfall variability over southern Africa. *J. Clim.*, **13**, 3789–3804.

Cook, K. H., and A. Gnanadesikan, 1991: Effects of saturated and dry land surfaces on the tropical circulation and precipitation in a general circulation model. *J. Clim.*, **4**, 873–889.

Cook, K. H., and E. K. Vizy, 2006: Coupled model simulations of the West African monsoon system : Twentieth- and twenty-first-century simulations. *J. Clim.*, **19**, 3681–3704.

——, and ——, 2012: Impact of climate change on mid-twenty-first century growing seasons in Africa. *Clim. Dyn.*, **39**, 2937–2955.

——, and ——, 2015: Detection and analysis of an amplified warming of the Sahara desert. *J. Clim.*, **in review**.

——, J.-S. Hsieh, and S. M. Hagos, 2004: The Africa – South America intercontinental teleconnection. *J. Clim.*, **17**, 2851–2865.

Crétat, J., E. K. Vizy, and K. H. Cook, 2014: How well are daily intense rainfall events captured by current climate models over Africa? *Clim. Dyn.*, **42**, 2691–2711.

Dai, A., 2001: Global precipitation and thunderstorm frequencies. Part II: Diurnal variations. *J. Clim.*, **14**, 1112–1128.

——, 2006: Precipitation characteristics in eighteen coupled climate models. *J. Clim.*, **19**, 4605–4630.

Davis, R. E., B. P. Hayden, D. A. Gay, W. L. Philips, and G. V. Jones, 1997: The North Atlantic subtropical anticyclone. *J. Clim.*, **10**, 728–744.

Dee, D. P., and Coauthors, 2011: The ERA-Interim reanalysis: configuration and performance of the data assimilation system. *Q. J. R. Meteorol. Soc.*, **137**, 553–597.

Deser, C., A. S. Phillips, and M. A. Alexander, 2010: Twentieth century tropical sea surface temperature trends revisited. *Geophys. Res. Lett.*, **37**, L10701, doi:10.1029/2010GL043321.

Dirmeyer, P. a., and Coauthors, 2012: Simulating the diurnal cycle of rainfall in global climate models: resolution versus parameterization. *Clim. Dyn.*, **39**, 399–418.

Dudhia, J., 1989: Numerical study of convection observed during the winter monsoon experiment using a mesoscale two-dimensional model. *J. Atmos. Sci.*, **46**, 3077–3107.

Fasullo, J., and P. J. Webster, 2003: A hydrological definition of Indian monsoon onset and withdrawal. *J. Clim.*, **16**, 3200–3212.

Grist, J. P., and S. E. Nicholson, 2001: A Study of the dynamic factors influencing the rainfall variability in the West African Sahel. *J. Clim.*, **14**, 1337–1359.

Grosfeld, K., G. Lohmann, and N. Rimbu, 2008: The impact of Atlantic and Pacific Ocean sea surface temperature anomalies on the North Atlantic multidecadal variability. *Tellus A*, **60A**, 728–741.

Hagos, S. M., and K. H. Cook, 2007: Dynamics of the West African monsoon jump. *J. Clim.*, **20**, 5264–5284.

——, and ——, 2008: Ocean Warming and Late-Twentieth-Century Sahel Drought and Recovery. *J. Clim.*, **21**, 3797–3814.

——, and ——, 2009: Development of a coupled regional model and its application to the study of interactions between the West African monsoon and the eastern tropical Atlantic Ocean. *J. Clim.*, **22**, 2591–2604.

Hodges, K. I., and C. D. Thorncroft, 1997: Distribution and statistics of African mesoscale convective weather systems based on the ISCCP Meteosat imagery. *Mon. Weather Rev.*, **125**, 2821–2837.

Hong, S.-Y., Y. Noh, and J. Dudhia, 2006: A New vertical diffusion package with an explicit treatment of entrainment processes. *Mon. Weather Rev.*, **134**, 2318–2341.

Huffman, G. J., and Coauthors, 2007: The TRMM multisatellite precipitation analysis (TMPA): quasi-global, multiyear, combined-sensor precipitation estimates at fine scales. *J. Hydrometeorol.*, **8**, 38–55.

Janicot, S., V. Moron, and B. Fontaine, 1996: Sahel droughts and ENSO dynamics. *Geophys. Res. Lett.*, **23**, 515–518.

Janiga, M. A., and C. D. Thorncroft, 2014: Convection over tropical Africa and the East Atlantic during the West African monsoon: regional and diurnal variability. *J. Clim.*, **27**, 4159–4188.

Janjić, Z. I., 1994: The step-mountain Eta coordinate model: Further developments of the convection, viscous sublayer, and turbulence closure schemes. *Mon. Weather Rev.*, **122**, 927–945.

Kain, J. S., 2004: The Kain–Fritsch convective parameterization: An update. *J. Appl. Meteorol.*, **43**, 170–181.

Kanamitsu, M., W. Ebisuzaki, J. Woollen, S.-K. Yang, J. J. Hnilo, M. Fiorino, and G. L. Potter, 2002: NCEP–DOE AMIP-II Reanalysis (R-2). *Bull. Am. Meteorol. Soc.*, **83**, 1631–1643.

Kosaka, Y., and S.-P. Xie, 2013: Recent global-warming hiatus tied to equatorial Pacific surface cooling. *Nature*, **501**, 403–407.

Koster, R. D., and Coauthors, 2006: GLACE: The Global Land – Atmosphere Coupling Experiment . Part I: Overview. *J. Hydrometeorol.*, **7**, 590–611.

Laing, A. G., and J. M. Fritsch, 1993: Mesoscale convective complexes in Africa. *Mon. Weather Rev.*, **121**, 2254–2263.

——, R. Carbone, V. Levizzani, and J. Tuttle, 2008: The propagation and diurnal cycles of deep convection in northern tropical Africa. *Q. J. R. Meteorol. Soc.*, **134**, 93–109.

——, S. B. Trier, and C. A. Davis, 2012: Numerical simulation of episodes of organized convection in tropical northern Africa. *Mon. Weather Rev.*, **140**, 2874–2886.

Lebel, T., and Coauthors, 2010: The AMMA field campaigns: multiscale and multidisciplinary observations in the West African region. *Q. J. R. Meteorol. Soc.*, **136**, 8–33.

Lee, M.-I., and Coauthors, 2007: Sensitivity to horizontal resolution in the AGCM simulations of warm season diurnal cycle of precipitation over the United States and northern Mexico. *J. Clim.*, **20**, 1862–1881.

Liebmann, B., I. Bladé, G. N. Kiladis, L. M. V. Carvalho, G. B. Senay, D. Allured, S. Leroux, and C. Funk, 2012: Seasonality of African precipitation from 1996 to 2009. *J. Clim.*, **25**, 4304–4322.

Marteau, R., V. Moron, and N. Philippon, 2009: Spatial Coherence of Monsoon Onset over Western and Central Sahel (1950–2000). *J. Clim.*, **22**, 1313–1324.

Martin, E. R., and C. D. Thorncroft, 2013: The impact of the AMO on the West African monsoon annual cycle. *Q. J. R. Meteorol. Soc.*, doi:10.1002/qj.2107.

Mathon, V., and H. Laurent, 2001: Life cycle of Sahelian mesoscale convective cloud systems. *Q. J. R. Meteorol. Soc.*, **127**, 377–406.

——, ——, and T. Lebel, 2002: Mesoscale convective system rainfall in the Sahel. *J. Appl. Meteorol.*, **41**, 1081–1092.

Mlawer, E. J., S. J. Taubman, P. D. Brown, M. J. Iacono, and S. A. Clough, 1997: Radiative transfer for inhomogeneous atmospheres: RRTM, a validated correlated-k model for the longwave. *J. Geophys. Res. Atmos.*, **102**, 16663–16682.

Mohr, K. I., 2004: Interannual , monthly , and regional variability in the wet season diurnal cycle of precipitation in sub-Saharan Africa. *J. Clim.*, **17**, 2441–2453.

Nesbitt, S. W., and E. J. Zipser, 2003: The diurnal cycle of rainfall and convective intensity according to three years of TRMM measurements. *J. Clim.*, **16**, 1456–1475.

Nicholson, S. E., and J. P. Grist, 2003: The seasonal evolution of the atmospheric circulation over West Africa and Equatorial Africa. *J. Clim.*, **16**, 1013–1030.

Noda, A. T., K. Oouchi, M. Satoh, and H. Tomita, 2012: Quantitative assessment of diurnal variation of tropical convection simulated by a global nonhydrostatic model without cumulus parameterization. *J. Clim.*, **25**, 5119–5134.

Pearson, K. J., G. M. S. Lister, C. E. Birch, R. P. Allan, R. J. Hogan, and S. J. Woolnough, 2013: Modelling the diurnal cycle of tropical convection across the "grey zone." *Q. J. R. Meteorol. Soc.*, **140**, 491–499.

Ploshay, J. J., and N.-C. Lau, 2010: Simulation of the diurnal cycle in tropical rainfall and circulation during boreal summer with a high-resolution GCM. *Mon. Weather Rev.*, **138**, 3434–3453.

Raia, A., and I. F. de A. Cavalcanti, 2008: The life cycle of the South American monsoon system. *J. Clim.*, **21**, 6227–6246.

Ramel, R., H. Gallée, and C. Messager, 2006: On the northward shift of the West African monsoon. *Clim. Dyn.*, **26**, 429–440.

Rienecker, M. M., and Coauthors, 2011: MERRA - NASA's Modern-Era Retrospective Analysis for Research and Applications. *J. Clim.*, **24**, 3624–3648.

Rio, C., F. Hourdin, J.-Y. Grandpeix, and J.-P. Lafore, 2009: Shifting the diurnal cycle of parameterized deep convection over land. *Geophys. Res. Lett.*, **36**, doi:10.1029/2008GL036779.

Rio, C., and Coauthors, 2013: Control of deep convection by sub-cloud lifting processes: the ALP closure in the LMDZ5B general circulation model. *Clim. Dyn.*, **40**, 2271–2292.

Rodwell, M. J., and B. J. Hoskins, 2001: Subtropical Anticyclones and Summer Monsoons. *J. Clim.*, **14**, 3192–3211.

Rowell, D. P., 2001: Teleconnections between the tropical Pacific and the Sahel. *Q. J. R. Meteorol. Soc.*, **127**, 1683–1706.

Saha, S., and Coauthors, 2010: The NCEP Climate Forecast System Reanalysis. *Bull. Am. Meteorol. Soc.*, **91**, 1015–1057.

Sato, T., H. Miura, M. Satoh, Y. N. Takayabu, and Y. Wang, 2009: Diurnal cycle of precipitation in the tropics simulated in a global cloud-resolving model. *J. Clim.*, **22**, 4809–4826.

Seager, R., R. Murtugudde, N. Naik, A. Clement, N. Gordon, and J. Miller, 2003: Air – Sea Interaction and the Seasonal Cycle of the Subtropical Anticyclones. *J. Clim.*, **16**, 1948–1966.

Shi, X., and D. R. Durran, 2014: The Response of Orographic Precipitation over Idealized Midlatitude Mountains Due to Global Increases in CO 2. *J. Clim.*, **27**, 3938–3956.

——, and ——, 2015: Estimating the response of extreme precipitation over mid-latitide mountains to global warming. *J. Clim.*, **in review**.

Shinoda, M., T. Okatani, and M. Saloum, 1999: Diurnal variations of rainfall over Niger in the West African Sahel: a comparison between wet and drought years. *Int. J. Climatol.*, **19**, 81–94.

Skamarock, W. C., and Coauthors, 2008: *A description of the advanced research WRF version 3. NCAR/TN-475+STR*. [Available from NCAR Information Services, P.O. Box 3000, Boulder, CO 80307.], 1-113 pp.

Sorooshian, S., K.-L. Hsu, X. Gao, H. V Gupta, B. Imam, and D. Braithwaite, 2000: Evaluation of PERSIANN system satellite–based estimates of tropical rainfall. *Bull. Am. Meteorol. Soc.*, **81**, 2035–2046.

Sultan, B., and S. Janicot, 2003: The West African monsoon dynamics . part II : The "preonset" and "onset" of the summer monsoon. *J. Clim.*, **16**, 3407–3428.

Sutton, R. T., B. Dong, and J. M. Gregory, 2007: Land/sea warming ratio in response to climate change: IPCC AR4 model results and comparison with observations. *Geophys. Res. Lett.*, **34**, L02701, doi:10.1029/2006GL028164. http://doi.wiley.com/10.1029/2006GL028164 (Accessed January 24, 2015).

Syroka, J., and R. Toumi, 2004: On the withdrawal of the Indian summer monsoon. *Q. J. R. Meteorol. Soc.*, **130**, 989–1008.

Thompson, G., R. M. Rasmussen, and K. Manning, 2004: Explicit forecasts of winter precipitation using an improved bulk microphysics scheme. Part I: description and sensitivity analysis. *Mon. Weather Rev.*, **132**, 519–542.

Thorncroft, C. D., H. Nguyen, C. Zhang, and P. Peyrillé, 2011: Annual cycle of the West African monsoon: regional circulations and associated water vapour transport. *Q. J. R. Meteorol. Soc.*, **137**, 129–147.

Tokinaga, H., S.-P. Xie, C. Deser, Y. Kosaka, and Y. M. Okumura, 2012: Slowdown of the Walker circulation driven by tropical Indo-Pacific warming. *Nature*, **491**, 439–443.

Trenberth, K. E., and D. J. Shea, 2006: Atlantic hurricanes and natural variability in 2005. *Geophys. Res. Lett.*, **33**, L12704, doi:10.1029/2006GL026894.

Vizy, E. K., and K. H. Cook, 2009: A mechanism for African monsoon breaks: Mediterranean cold air surges. *J. Geophys. Res.*, **114**, 1–19.

——, and ——, 2013: Impact of cold air surges on rainfall variability in the Sahel and wet African tropics: A multi-scale analysis. *Clim. Dyn.*, doi:10.1007/s00382-013-1953-z.

——, and ——, 2014: Capturing the Atlantic cold tongue and coastal upwelling in an intermediate-level ocean model coupled to a regional climate model. *Clim. Dyn.*, **42**, 345–366.

——, ——, J. Crétat, and N. Neupane, 2013: Projections of a wetter Sahel in the 21st century from global and regional models. *J. Clim.*, **26**, 4664–4687.

Wang, B., and LinHo, 2002: Rainy season of the Asian–Pacific summer monsoon. *J. Clim.*, **15**, 386–398.

Washington, R., and Coauthors, 2009: Dust as a tipping element : The Bodélé Depression, Chad. *Proc. Natl. Acad. Sci. U. S. A.*, **106**, 20564–20571.

Wu, L., and Coauthors, 2012: Enhanced warming over the global subtropical western boundary currents. *Nat. Clim. Chang.*, **2**, 161–166.

Xie, P., J. E. Janowiak, P. A. Arkin, R. F. Adler, A. Gruber, R. Ferraro, G. J. Huffman, and S. Curtis, 2003: GPCP pentad precipitation analyses: an experimental dataset based on gauge observations and satellite estimates. *J. Clim.*, **16**, 2197–2214.

Xue, Y., and Coauthors, 2010: Intercomparison and analyses of the climatology of the West African Monsoon in the West African Monsoon Modeling and Evaluation project (WAMME) first model intercomparison experiment. *Clim. Dyn.*, **35**, 3–27.

Yang, G.-Y., and J. Slingo, 2001: The diurnal cycle in the tropics. *Mon. Weather Rev.*, **129**, 784–801.

Zhang, C., P. Woodworth, and G. Gu, 2006: The seasonal cycle in the lower troposphere over West Africa from sounding observations. *Q. J. R. Meteorol. Soc.*, **132**, 2559–2582.

Zhang, G., and K. H. Cook, 2014: West African monsoon demise: Climatology, interannual variations, and relationship to seasonal rainfall. *J. Geophys. Res. Atmos.*, **119**, 10175–10193.

——, ——, and E. K. Vizy, 2015a: The diurnal cycle of warm season rainfall over West Africa. Part II: Convection-permitting simulations. *J. Clim.*, **submitted**.

——, ——, and ——, 2015b: The diurnal cycle of warm season rainfall over West Africa. Part I: Observational Analysis. *J. Clim.*, **submitted**.

Zhou, J., and K.-M. Lau, 1998: Does a monsoon climate exist over South America? *J. Clim.*, **11**, 1020–1040.